

UNIVERSIDAD DE VALENCIA - CSIC
DEPARTAMENTO DE FÍSICA ATÓMICA, MOLECULAR Y NUCLEAR
INSTITUTO DE FÍSICA CORPUSCULAR



UNIVERSITAT DE VALÈNCIA

Beta decay studies in the $N \approx Z$ and the rare-earth regions using Total Absorption Spectroscopy techniques

ENRIQUE NÁCHER GONZÁLEZ

TESIS DOCTORAL

SEPTIEMBRE DE 2004

UNIVERSIDAD DE VALENCIA - CSIC
INSTITUTO DE FÍSICA CORPUSCULAR

DEPARTAMENTO DE FÍSICA ATÒMICA,
MOLECULAR I NUCLEAR

**Beta decay studies in the $N \approx Z$ and the
rare-earth regions using Total Absorption
Spectroscopy techniques**

ENRIQUE NÁCHER GONZÁLEZ
TESIS DOCTORAL
SEPTIEMBRE DE 2004

Berta Rubio Barroso, Colaborador Científico del Consejo Superior de Investigaciones Científicas (CSIC), y **Alejandro Algora**, Senior Research Associate at the Institute of Nuclear Research of the Hungarian Academy of Sciences, Debrecen (Hungary)

CERTIFICAN: Que la presente memoria “**Beta decay studies in the $N \approx Z$ and the rare-earth regions using Total Absorption Spectroscopy techniques**” ha sido realizada bajo su dirección en el Instituto de Física Corpuscular (Centro Mixto Universidad de Valencia - CSIC) por **Enrique Nácher González** y constituye su Trabajo de Investigación dentro del programa de doctorado del Departamento de Física Atómica, Molecular y Nuclear.

Y para que así conste, en cumplimiento con la legislación vigente, presenta ante el Departamento de Física Atómica, Molecular y Nuclear la referida memoria, firmando el presente certificado en Burjassot (Valencia) a 20 de Septiembre de 2004.

Contents

I	General introduction	1
1	The β-decay process	3
1.1	Introduction. Energetics in β -decay	3
1.2	The Fermi theory of β -decay	4
1.3	Charge-Exchange reactions: The Gamow-Teller resonance	6
1.3.1	The Gamow-Teller sum-rule	6
1.4	Charge-exchange reactions and β -decay	9
2	Experimental techniques: High-resolution vs Total Absorption Spectroscopy	13
2.1	The GT strength distribution from β^+ -decay	13
2.2	How to measure the $I_\beta(E)$ distribution	14
2.2.1	The HRS technique and the “ <i>pandemonium effect</i> ”	14
2.2.2	The Total Absorption Spectroscopy technique	17
3	The data analysis method	21
3.1	The Expectation maximisation (EM) algorithm	21
3.2	The problem of the subtractions	24
II	The N=Z nucleus ^{76}Sr	29
4	The nuclei with $A \approx 70-80$ in the vicinity of the N=Z line	31
4.1	Deformed nuclei	31
4.1.1	Quadrupole moments	31
4.1.2	Deformation parameters	31
4.2	General features of the region	33
4.3	Self-consistent Hartree-Fock + BCS + QRPA formalism in deformed nuclei	34
4.4	The N=Z nucleus ^{76}Sr	36

5	The experiment	39
5.1	The ISOLDE mass separator at the PS-Booster	39
5.2	Lucrecia, the TAS at ISOLDE	41
5.3	The measurement	43
6	Data analysis of the ^{76}Sr β-decay	45
6.1	Sorting the data	45
6.2	Determination of the contaminants	47
6.3	The EM algorithm applied to the data	49
7	Results and discussion	53
7.1	The B(GT) distribution in the β -decay of ^{76}Sr	53
7.2	Conclusion: The shape of the N=Z nucleus ^{76}Sr from its β -decay . . .	55

III The Gamow-Teller resonance in the Rare-Earth region 59

8	The Rare-earth nuclei above ^{146}Gd	61
8.1	The quasi-doubly magic ^{146}Gd	61
8.2	The nuclei around ^{146}Gd . The fast GT decay $\pi h_{11/2} \rightarrow \nu h_{9/2}$	62
9	The experiment	65
9.1	The GSI accelerator facilities	65
9.2	ISOL, the On-Line Mass Separator	66
9.3	The TAS at GSI	68
9.4	The measurement of ^{152}Tm β -decay	70
10	Data analysis of the ^{152}Tm β-decay	75
10.1	^{152}Tm low-spin ($J^\pi=2^-$): The sorting and preparation of the data	75
10.2	^{152}Tm low-spin ($J^\pi=2^-$): Analysis using the EM algorithm	79
10.3	^{152}Tm high-spin ($J^\pi=9^+$): The sorting and analysis of the data	81
10.4	Results and discussion: The GT strength distribution in the decay of ^{152}Tm	84
11	Summary of the other decays in the region pertinent to the present discussion: ^{148}Dy, ^{148}Tb and ^{156}Tm	89
11.1	Beta decay of ^{148}Dy	89
11.2	Beta decay of ^{148}Tb	91
11.3	Beta decay of ^{156}Tm	95

12 Systematics of the GT resonance in the rare-earth region.	
Theoretical shell model calculations	99
12.1 Systematics of the GT resonance in the region	99
12.2 Shell model calculations	107
12.3 Summary and conclusion	112
IV Resumen en español	115

List of Figures

1.1	Neutron time-of-flight spectra at $\theta = 0^\circ$ for the (p,n) reaction on various nuclear targets.	7
1.2	Fraction of GT sum-rule strength observed in (p,n) reactions.	8
1.3	Allowed β^+ -decay in the nuclear chart: The $N \approx Z$ nuclei up to $A \approx 70$ -80, the nuclei around the doubly magic ^{100}Sn , and the rare-earth nuclei around mass 150.	12
2.1	Comparison between the <i>apparent</i> $B(GT)$ obtained with Ge detectors with the real one. In the graph the vertical axes is the excitation energy in the daughter nucleus.	16
2.2	Ideal TAS: a very big NaI(Tl) detector covering a 4π solid angle around the radioactive source (left). From the direct spectrum one can obtain directly the $I_\beta(E)$ distribution.	17
2.3	Real TAS: as soon as we place some dead material near the source the photo-peak efficiency of the detector decreases and escape peaks and a continuum appear in the measured spectrum.	18
3.1	Details of the GSI TAS geometrical description in GEANT4. a) Longitudinal cut along the spectrometer showing the main crystal and the plug detector. b) Plug detector with ancillary detectors and absorber. c) Upper part: Ge detector cryostat and cold finger; lower part: Ge crystal and capsule. d) Mounting of the Si detectors and transport tape rollers together with the polyethylene absorber	22
3.2	Comparison between the analysis made subtracting pile-up and undesired activity (left), and the analysis taking into account these unwanted contributions in the analysis program, without any subtraction (right).	27
4.1	Oblate (left) and prolate (right) spheroids.	32
4.2	Bottom: Experimental $E(2^+)$ for the even-even, $N=Z$ nuclei from Ge to Mo. Top: Quadrupole deformation ε_2 derived from Grodzin's formula (dashed line) and other theoretical estimation (solid line). . .	33
4.3	Hartree-Fock energy as a function of deformation (quadrupole moment) for the light Sr isotopes.	35

4.4	Calculated Gamow-teller strength distributions in $g_A^2/4\pi$ units as a function of the excitation energy of the daughter nucleus. The calculations have been performed assuming different shapes for the parent nucleus.	36
5.1	Time structure of the PS-Booster. Each pulse contains $\approx 3 \times 10^{13}$ protons.	39
5.2	The PS-Booster accelerator at CERN.	40
5.3	Detector setup for the ^{76}Sr measurement. In the upper-left part we have a 3D plot of the cylindrical NaI(Tl) detector “Lucrecia”, and in the lower part we see a transverse cut through the main crystal and the ancillary detectors, as well as the tape where the separated ^{76}Sr beam is implanted.	41
5.4	Lucrecia, the biggest NaI(Tl) crystal ever made. At the left side of the picture there is the telescopic beam pipe.	42
5.5	Lucrecia’s total and photo-peak efficiency.	42
5.6	Direct spectra registered in Lucrecia and the ancillary detectors during the measurement of the ^{76}Sr β^+ -decay.	44
6.1	Energy spectra measured with the ancillary detectors.	45
6.2	Energy spectrum measured in Lucrecia without conditions (upper panel), requiring coincidence with the beta detector (middle panel) and requiring coincidence with the Rb K_α peak in the X-ray detector (lower panel).	46
6.3	^{76}Rb decay spectrum and its contaminants (see text).	48
6.4	^{76}Sr decay spectrum and its contaminants (see text).	49
6.5	Simulation of the β -decay of ^{24}Na (red) overlaid to the measured ^{24}Na source (black).	50
6.6	Top: Experimental spectrum for the ^{76}Sr decay (grey shade). Overlaid there is the recalculated spectrum using the result after the analysis (dashed line). Bottom: Resulting $I_\beta(E)$ after the data deconvolution.	52
7.1	B(GT) distribution in the β^+ -decay of ^{76}Sr as a function of the excitation energy in the daughter nucleus ^{76}Rb	53
7.2	Comparison between the results of this work (solid line) and those obtained using a high resolution setup (red dots).	55
7.3	B(GT) distribution resulting from this work compared with the theoretical calculations for prolate and oblate shapes of ^{76}Sr	56
7.4	Accumulated B(GT) from this work compare with the theoretical calculations for prolate and oblate shapes of ^{76}Sr	57

8.1	Extreme single-particle representation of the configuration of the two isomers in the odd-N=83 isotopes above ^{146}Gd . The low-spin isomer is on the left side and the high-spin isomer on the right one.	63
8.2	Qualitative description of our expectation for the decay of the low-spin isomer (left) and the high-spin isomer (right).	64
9.1	A view of the <i>UNILAC</i> and the layout of the GSI accelerator facilities.	66
9.2	The on-line mass separator.	67
9.3	The Total Absorption Spectrometer at the on-line mass separator. . .	69
9.4	GSI TAS' total and photo-peak efficiency.	69
9.5	Selective production of the two isomers of ^{152}Tm	71
9.6	Direct spectra registered in the TAS and the ancillary detectors during the measurement of the ^{152}Tm 2^- decay.	73
9.7	Direct spectra registered in the TAS and the ancillary detectors during the measurement of the ^{152}Tm 9^+ decay.	74
10.1	X-ray spectrum during the measurement of the decay of ^{152}Tm 2^- . The shade regions represent the gates set for the coincidences.	76
10.2	Top: EC component of the decay of the low-spin isomer of ^{152}Tm (black) and its contaminants (red). Bottom: Resulting spectrum after the subtraction.	77
10.3	Top: EC spectrum of the decay of the low-spin isomer of ^{152}Tm (black) clean from isobaric contaminants. Overlaid in red colour: Clean EC spectrum of the decay of the high-spin isomer of ^{152}Tm . Bottom: Resulting spectrum after the subtraction.	78
10.4	Low amplification germanium spectrum. We see transitions that can only come from the decay of the high-spin isomer.	79
10.5	Simulation of the β -decay of ^{24}Na (red) overlaid to the measured ^{24}Na source (black).	80
10.6	Top: Experimental spectrum for the ^{152}Tm 2^- decay (grey shade). Overlaid there is the recalculated spectrum using the result after the analysis (dashed line). Bottom: Resulting $I_\beta(E)$ after the data deconvolution.	81
10.7	Top: The black curve is the ^{152}Tm 9^+ decay clean of any isobaric contamination. The red spectrum is the ^{152}Tm 2^- decay plus the pile-up. It has been normalised to the peak at 808.2 keV. Bottom: Result of the subtraction of the two spectra of the upper panel.	82
10.8	Top: Experimental spectrum for the ^{152}Tm 9^+ decay (grey shade). Overlaid is the recalculated spectrum using the result after the analysis (dashed line). Bottom: Resulting $I_\beta(E)$ after the data deconvolution.	83
10.9	Left: End point of the EC spectrum measured in the TAS for the decay of the 2^- isomer. Right: End point of the positron spectrum measured in the Ge detector for the same decay.	84

10.10	B(GT) distribution in the β^+ -decay of ^{152}Tm . Upper panel: high-spin isomer (9^+) decay. Lower panel: low-spin isomer (2^-) decay.	85
10.11	Comparison between the results of this work (solid line) and those obtained using a high resolution setup (red dots).	87
11.1	Extreme single-particle representation of the β -decay of ^{148}Dy	89
11.2	Left: Experimental EC spectrum of the ^{148}Dy decay (grey shade) and recalculated spectrum after the analysis (dashed line). Right: Gamow-Teller strength in the β -decay of ^{148}Dy	90
11.3	Same as in Fig. 11.2 for the decay of $^{148}\text{Tb } 2^-$	92
11.4	Same as in Fig. 11.2 for the decay of $^{148}\text{Tb } 9^+$	95
11.5	Same as in Fig. 11.2 for the decay of ^{156}Tm	97
12.1	Gamow-Teller strength distribution in the β -decay of the odd-N=83 nuclei above ^{146}Gd pertinent to the present discussion (see text).	100
12.2	Gamow-Teller strength distribution in the decay of ^{156}Tm (top) compared to the same distribution in the decay of $^{152}\text{Tm } 2^-$ (bottom).	105
12.3	Evolution of the total B(GT) as a function of the occupancy number of the proton orbital $h_{11/2}$	107
12.4	Gamow-Teller strength distribution for the low-spin isomer of the odd-N=83 nuclei above ^{146}Gd . The results from the TAS measurement (black/grey) are compared with a shell-model calculation (red).	109
12.5	Same as Fig. 12.4 but for the high-spin isomers.	110
12.6	Espectro de tiempo de vuelo de los neutrones a $\theta = 0^0$ para la reacción (p,n) sobre distintos blancos nucleares	118
12.7	TAS en el caso ideal: Los dos rayos γ que aparecen tras la desintegración β son totalmente absorbidos por el detector. Del espectro se puede obtener directamente la intensidad beta I_β	119
12.8	Distribución B(GT) en unidades de $g_A^2/4\pi$ como función de la energía de excitación del núcleo hijo. El cálculo se ha realizado asumiendo diferentes deformaciones en el estado fundamental.	120
12.9	Espectros directos registrados en Lucrecia y en los detectores auxiliares durante la medida de la desintegración del ^{76}Sr	121
12.10	Distribución B(GT) en la desintegración β del ^{76}Sr como función de la energía de excitación del núcleo hijo ^{76}Rb	122
12.11	En el panel superior se representa la distribución de B(GT) en intervalos de energía de 800 keV. En el panel inferior se muestra para cada canal la B(GT) integrada hasta ese canal. En ambos casos los cuadrados negros son el resultado experimental de este trabajo, la línea solida roja en cálculo teórico para forma prolada, y la azul para forma oblada.	124
12.12	Distribución B(GT) en la desintegración de los dos isómeros de los núcleos impar-N=83 estudiados en este trabajo.	127

12.13	Distribución B(GT) en la desintegración del ^{148}Dy (izda.) y del ^{156}Tm (dcha).	128
12.14	Evolución de la B(GT) total con el número de protones en el orbital $h_{11/2}$.	130
12.15	Distribución B(GT) en el isómero de bajo espín de los núcleos impar-N=83 por encima del ^{146}Gd . Los resultados experimentales (gris) se comparan con cálculos teóricos shell-model (rojo).	131
12.16	Como en la Fig. 12.4 pero para los isómeros de alto espín.	131

List of Tables

9.1	Main characteristics of the on-line mass separator at GSI	67
12.1	Ratio between B(GT) values: comparison between the expected value from a shell model calculation and the experimental results of this work. Only the experimental errors are taken into account.	102
12.2	Same as Tab. 12.1	103
12.3	Same as Tab. 12.1	103
12.4	Reacciones de fusión-evaporación utilizadas en este estudio sistemático	126

Part I

General introduction

Chapter 1

The β -decay process

1.1 Introduction. Energetics in β -decay

When the ratio between the number of protons (Z) and neutrons (N) in the atomic nucleus is such that the nuclear strong interaction can no longer keep it bound, it becomes unstable. At this point Nature provides different disintegration mechanisms that the nuclei can use to become more stable. Normally, these mechanisms imply a change in both Z and N . The most common way for unstable nuclei to approach the equilibrated ratio between Z and N , thus getting closer to stability, is the so-called beta decay process (β -decay).

Beta decay is the process of conversion of a proton into a neutron or a neutron into a proton in the atomic nucleus. The former case is called β^+ -decay whereas the latter is the β^- -decay. H. Becquerel discovered the phenomenon of radioactivity in 1896. Some years later the experiments of E. Rutherford and of P. and M. Curie showed that radioactivity contained components with different powers to penetrate matter. They were called α , β and γ rays. It took thirty-eight years more to discover the β^+ -decay. The Joliot-Curies observed it in 1934, just two years after the discovery of the positron in the cosmic rays.

Let us now turn to the β -decay process in more detail. There are three different processes that we regard as β -decay. The first, β^- -decay, is the emission of an electron from the nucleus in such a way that a neutron is converted into a proton and the nuclear charge Z increases by one unit. This process takes place in neutron-rich nuclei, following the path to approach the valley of stability by converting neutrons into protons. The second process, β^+ -decay, happens when a positron is emitted from the nucleus. In this case a proton is converted into a neutron and consequently the nuclear charge Z decreases by one unit. In competition with the β^+ -decay there is also the *Electron Capture* process (EC), which occurs when an atomic electron, usually from the K-shell, is captured by a nuclear proton, creating a neutron as a result. Again Z decreases by one unit. The second and third processes are typical

of proton-rich nuclei, following the path to the valley of stability by converting protons into neutrons. In this description one would assume that β -decay is a process which ends with a two-body final state, which is completely wrong. In that hypothetical case, the electron or positron released in the decay should have always the same energy. The measured spectra showed during many years that this was not the case, the charged particle was released with an energy covering a wide continuum. This strange feature of β -decay led Pauli to postulate in 1931 that there was another particle released in the process: the neutrino. The discovery of such particle by Reines and Cowan in 1959 confirmed the three-body final state of β -decay. Now we can write the three different processes at the level of nucleons as follows:

$$\begin{aligned}\beta^- &: n \rightarrow p + e^- + \bar{\nu}_e \\ \beta^+ &: p \rightarrow n + e^+ + \nu_e \\ EC &: p + e^- \rightarrow n + \nu_e\end{aligned}$$

The decay of the free proton is energetically forbidden. Protons can only decay inside a nucleus, taking the energy needed from the nucleus. We are not concerned about the decay of single nucleons but of unstable nuclei. The three corresponding decay processes in nuclei can be expressed as follows:

$$\begin{aligned}\beta^- &: {}^A_Z X_N \rightarrow {}^A_{Z+1} X_{N-1} + e^- + \bar{\nu}_e & Q_{\beta^-} &= [M({}^A_Z X_N) - M({}^A_{Z+1} X_{N-1})]c^2 \\ \beta^+ &: {}^A_Z X_N \rightarrow {}^A_{Z-1} X_{N+1} + e^+ + \nu_e & Q_{\beta^+} &= [M({}^A_Z X_N) - M({}^A_{Z-1} X_{N+1})]c^2 - 2m_e c^2 \\ EC &: {}^A_Z X_N + e^- \rightarrow {}^A_{Z-1} X_{N+1} + \nu_e + X_{\text{ray}} & Q_{EC} &= [M({}^A_Z X_N) - M({}^A_{Z-1} X_{N+1})]c^2 - B_e\end{aligned}$$

On the right hand side of each process is shown the Q value, the kinetic energy released in the process, which is equal to the difference of the masses in the initial and final states. In the case of the EC process there appears a negative term B_e which is the binding energy of the atomic shell from which the electron was captured. In the $N \approx Z$, $A \approx 70-80$ nuclei this energy is around 11-13 keV in the case of the K-shell, whereas in the rare-earth region it can reach up to 43-50 keV. Neglecting this term, the difference in Q value between the β^+ and the EC process is twice the mass of the electron: 1022 keV. In other words, the energy window available for the decay is 1022 keV bigger for the EC process than for the β^+ process.

1.2 The Fermi theory of β -decay

In this section we will introduce the theory underlying these processes, which are governed by weak interaction. In this way we hope to establish the motivation for this work and introduce the quantities that will play an

important role in our study. The Fermi theory of the β -decay dates back to 1934. According to it, the process of β -decay can happen by two different modes: The Fermi (F) and the Gamow-Teller (GT) modes. In the former the operator that drives the interaction is just the isospin raising (β^+ -decay) or lowering (β^- -decay) operator¹: $O_F = \tau^\pm$. This operator is independent of the nuclear spin and hence it does not involve any change in angular momentum, thus it is a vector operator. In the Gamow-Teller mode there is also the Pauli spin operator: $O_{GT} = \sigma\tau^\pm$. This is an axial operator because it involves a change in angular momentum. In other words, the GT decay mode can change the spin of the nucleus whereas this is not possible in the case of Fermi decay. The selection rules for these processes are: for Fermi transitions $\Delta J = 0$ and $\Delta\pi = 0$, and for GT transitions $\Delta J = 0, \pm 1$ ($J_i = J_f = 0$ excluded) and $\Delta\pi = 0$. Therefore, we see that we can extract information about the spin-isospin properties of nuclei by studying the Gamow-Teller β -decay.

According to Fermi's Golden Rule, the transition rates for both Fermi and Gamow-Teller processes must be proportional to the square of the matrix element between the initial and final state:

$$\begin{aligned}
 B(F) &= | \langle \psi_f | \sum_{k=1}^A \tau_k^\pm | \psi_i \rangle |^2 \equiv \langle \tau \rangle^2 \\
 B(GT) &= | \langle \psi_f | \sum_{k=1}^A \vec{\sigma}_k \tau_k^\pm | \psi_i \rangle |^2 \equiv \langle \sigma\tau \rangle^2
 \end{aligned}
 \tag{1.1}$$

normally regarded as reduced transition probabilities, or the Fermi and Gamow-Teller strength respectively. The word ‘‘reduced’’ stresses the fact that the $B(F)$ and $B(GT)$ do not depend on the phase space available in the final state as the real probability does. Due to the isospin selection rule the Fermi decay is suppressed over most of the nuclear chart, and in particular in our cases of study. Therefore, in what follows only Gamow-Teller transitions will be considered. From the definition (1.1) we see that, if we can measure the $B(GT)$ properly in β -decay, we will have an idea of the importance of spin-isospin excitations in nuclei. But this is not the only way to study the excitations which involve the $\sigma\tau$ operator. The charge-exchange reactions, (p,n) and (n,p), are also driven by the $\sigma\tau$ operator². To be sure that there is no angular momentum transfer in the reaction ($L=0$) the angular distribution of the final neutron or proton must be peaked at zero degrees. Therefore, measurements of (p,n) or (n,p) cross-sections at zero degrees are directly related to the GT strength defined above (1.1), and are closely related to the β -decay process. For many years, (p,n) experiments have been the most popular way to study the GT strength and the spin-isospin properties of nuclei [2][3].

¹Here we follow the convention $T_z=-1/2$ for the proton, and $T_z=+1/2$ for the neutron. This is the usual convention in Nuclear Physics but not in Particle Physics [1].

²This includes (p,n) type reactions such as ($^3\text{He},T$) or (n,p) type reactions such as ($d,^2\text{He}$).

1.3 Charge-Exchange reactions: The Gamow-Teller resonance

When we mention giant resonances in nuclear physics we are talking about elementary modes of nuclear excitation which involve the coherent motion of many nucleons in the nucleus or, in other words, a superposition of single particle excitations. Both pictures represent the same excitation, either from the macroscopic or the microscopic point of view respectively. For instance the isoscalar modes are nuclear vibrations with protons and neutrons moving in phase, whereas isovector modes are those where protons and neutrons move in opposite phase.

According to [2], in $N > Z$ nuclei, the Gamow-Teller resonance is a collective spin-isospin oscillation mode in which the excess neutrons coherently change the direction of their spins and isospins without changing the orbital motion. This does not mean that all of them change spin and isospin, it is just one in average, but acting all of them as a whole, without distinction between the different particles, and herein lies the collectivity of the resonance. Following [4], for a quantum system like a nucleus this visual scheme is not clear and we should come to a microscopic viewpoint assuming that the GT resonance is described as a coherent superposition of one-particle-one-hole (1p-1h) excitations resulting from the action of the $\sigma\tau$ operator. The existence of these GT states was predicted in 1962 by Ikeda, Fujii and Fujita [5]. In 1975 the GT resonance was observed for the first time at Michigan [6], and during the 80s it was extensively studied by means of charge-exchange reactions. Many (p,n) reaction experiments were performed during those years at the Indiana University Cyclotron Facility (IUCF) [7][2]. In Fig. 1.1, taken from Ref. [7], we see some of the (p,n) zero-degree spectra measured in that laboratory. These spectra reveal a prominent resonance structure that corresponds to the excitation of this spin-isospin mode that we are referring to as the GT resonance. As we see, the peak is located at an excitation energy of $\approx 15-20$ MeV in the final nucleus ($\approx 180-185$ MeV for the neutron). Consequently, this energy will rarely be reached in the β -decay process. However there are a few exceptions where the resonance becomes accessible in β -decay because it lies inside the Q_{EC} window. We will talk about these cases later in this chapter.

1.3.1 The Gamow-Teller sum-rule

Let us consider the GT strength (1.1) summed over all final states. If it comes from a (p,n) reaction it will be driven by the τ^- operator, and in the case of the (n,p) reaction it will be the τ^+ operator.

$$S_+ = \frac{1}{2} \sum_f B_+(GT) \quad S_- = \frac{1}{2} \sum_f B_-(GT) \quad (1.2)$$

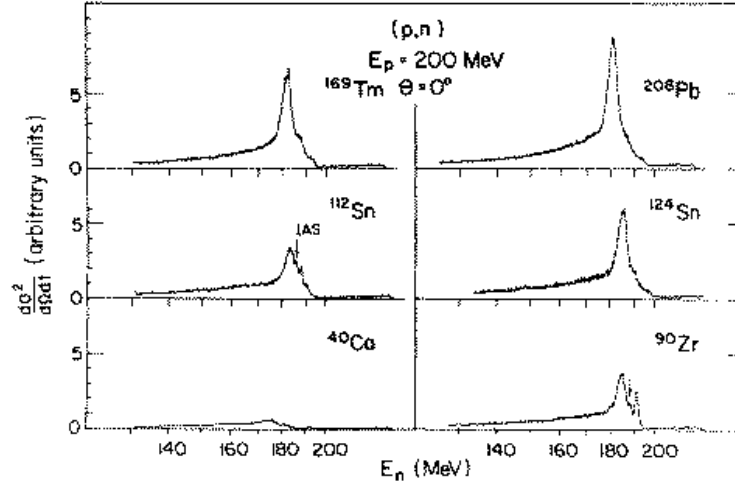


Figure 1.1: Neutron time-of-flight spectra at $\theta = 0^\circ$ for the (p,n) reaction on various nuclear targets. Taken from Ref. [7].

If now we take these two definitions and subtract one from the other we arrive at the GT sum-rule which was derived by K. Ikeda in Ref. [8]:

$$S_{GT} = S_- - S_+ = 3(N - Z) \quad (1.3)$$

This derivation assumes that the nucleons are point-like particles which interact via an effective two-nucleon interaction resulting from meson exchange, and explicit mesonic degrees of freedom are not taken into account. The most important characteristic of the GT sum-rule is that in the second term we have just $3(N - Z)$, three times the neutron excess. This means that the result is model-independent, it does not depend on details of the nuclear wave functions, only on the neutron excess.

By measuring zero-degree spectra for both (p,n) and (n,p) reactions at the same incident energy, one can subtract the (n,p) from the (p,n) data and, according to the GT sum-rule (1.3) the remaining cross section should be proportional to $3(N - Z)$. In the case of heavy nuclei with a large neutron excess the amplitude for converting protons into neutrons is strongly suppressed by the Pauli principle. Then the quantity S_+ of Eq.(1.3) can be neglected and we can assume that the relation:

$$S_{GT} \approx S_- = 3(N - Z) \quad (1.4)$$

applies directly to the summed GT strength seen in the (p,n) reaction. The experiments have been performed for many different nuclei and the result is surprising: only 60% of the expected total strength is observed in the zone of the peak [9]. Fig. 1.2 is a graphical view of such results. The error band comes from the uncertainty in the determination of the background to the spectra. The 40% of B(GT)

that does not show up in the (p,n) experiments, the so-called *missing strength*, has been the subject of many articles since 1975.

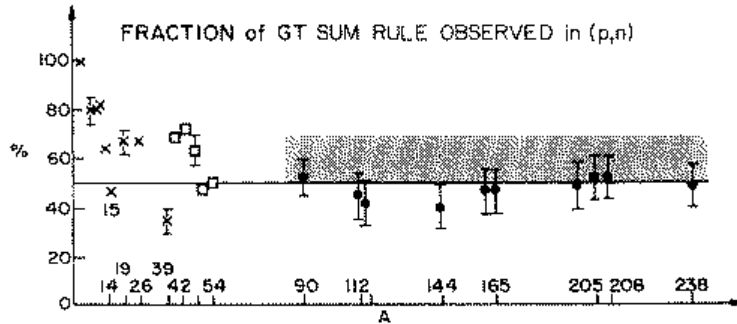


Figure 1.2: Fraction of GT sum-rule strength observed in (p,n) reactions.

This problem of the missing $B(GT)$ was found not only in (p,n) reactions but in β -decay measurements as well. In fact, in 1973, before the discovery of the GT resonance, D.H. Wilkinson [10] pointed out that β -decay between some mirror nuclei up to $A=21$ were hindered so that the effective axial coupling constant in nuclear matter should be smaller than the same constant for the free nucleons. However the β -decay data available at that moment were very limited and, in the case of medium mass and heavy nuclei, not properly measured as will be explained in Sec. 2.2.1. At this point it is already obvious that a proper measurement of the $B(GT)$ in the decay of medium and heavy nuclei is absolutely necessary to quantify the missing strength in this heavier region of the nuclear chart by means of the β -decay process to complement results from (p,n) reactions. We will come back to this point later in Sec. 1.4.

Following the literature one finds two different approaches to explain why there is a certain amount of $B(GT)$ missing in the charge-exchange reactions:

1. One possible theoretical explanation: $\Delta(1232)$ -hole excitations couple into the Nucleon-hole excitation and remove part of the strength at low energy. Theoreticians following this approach treat the problem in terms of a renormalisation of the axial coupling constant [11][12][13]. According to this explanation the missing strength should lie in the $\Delta(1232)$ region which would be at ≈ 300 MeV of excitation energy in the final nucleus.
2. The other possible explanation for the missing strength is based on the classical configuration mixing. Excitations at higher energy of 2Nucleon-1hole [14] and 2Nucleon-2holes [15][16] are mixed with the main 1Nucleon-1hole state and shift part of the strength mainly to the region beyond the resonance. According

to this hypothesis, the missing strength is in the background around the main resonant peak and spread in the continuum up to 50-60 MeV. To take this into account in the experiments, one should evaluate the $B(\text{GT})$ estimating the background accurately.

It took some years to clarify the question, but it turned out finally in 1997, that the role of the $\Delta(1232)$ -hole excitations was not necessary to explain the quenching of the Gamow-Teller resonance, with second explanation explaining this phenomenon better [17][18]. From the experimental side it was again a (p,n) reaction what gave rise to new results thanks to a better evaluation of the background. The experiment was carried out at the RCNP (Osaka) using a polarised proton beam at 195 MeV over a ^{90}Zr target [18]. This result demands confirmation from β -decay experiments in this mass region.

1.4 Charge-exchange reactions and β -decay

It was pointed out at the end of Sec. 1.2 that charge-exchange reactions and β -decay are two different manifestations of the same quantum process: the conversion of a proton into a neutron (or vice-versa) in the atomic nucleus. Under certain conditions both processes are driven by the same operator, namely the $\sigma\tau$ operator. Therefore, in principle, one should be able to study the same phenomena either via a charge-exchange reaction or β -decay. Furthermore, both processes have different advantages and drawbacks, and sometimes one process complements the other as will be explained later in this section. At this point we arrive at the main motivation for this work. So far (p,n) reactions have been the most widely applicable way to study the spin-isospin degrees of freedom of nucleons in the atomic nucleus. The aim of this work is to study the same thing but using a different tool: the β -decay process. This is important not only to confirm those results coming from (p,n) reactions, but also to complement these results in those cases where β -decay can be better measured or even the cases where it is the only possible tool to investigate the spin-isospin properties of the atomic nucleus (e.g. nuclei far from stability). To better understand the advantages and drawbacks of using one process or the other for this kind of study, let us summarise the main differences between (p,n) reactions and β -decay measurements:

1. The main drawback of charge-exchange reactions is the huge and unavoidable experimental background, always very difficult to estimate. This is a tremendous problem, especially when we know that the main part of the missing $B(\text{GT})$ probably lies in the background. In contrast, β -decay experiments are far cleaner and lack of such a huge experimental background. Even in the worst cases, when there is some undesired activity present during the experiment, this is easily identified and removed.

2. Obviously, β -decay is a process that can occur only for unstable nuclei, whereas (p,n) reactions have been studied so far just for stable nuclei. This may now change: radioactive beam facilities are starting to be operative ³. However, for the moment only a very few post-accelerated radioactive beams can be produced with enough intensity to perform and study nuclear reactions. Therefore charge-exchange reactions are limited for the moment to stable nuclei whereas β -decay is a process that can only happen to unstable nuclei. In this sense the two processes complement each other.
3. Finally, the last big difference and main drawback of β -decay is the energy window available for the process. Charge-exchange reactions are limited by the energy of the beam (this is not a problem nowadays) and by the determination of the energy of the light particle after the reaction. However, β -decay can only happen in a small energy window where the process releases energy. Therefore, we have to focus our measurements on the cases where the GT resonance, or at least a big part of it, lies inside this window. Unfortunately this only happens in a very few cases in the whole nuclear chart. When we compare our results with theoretical calculations we must take into account the accuracy of these calculations inside the energy window.

Following the first point, one must try to measure the GT resonance populated in β -decay to get rid of the problem of the background. Furthermore, most of the theoretical works cited earlier are based on experimental results obtained through charge-exchange reactions and one should measure the $B(\text{GT})$ properly through β -decay of medium mass and heavy nuclei to quantify the problem of the missing strength, thus allowing for further theoretical calculations based on the cleaner β -decay data. From the second point one sees that both processes are complementary in the sense that they cover two complementary areas of the nuclear chart: the stable nuclei and the nuclei far from stability. However, one hopes that, thanks to the forthcoming development of radioactive beams, at some moment it will become possible to compare the strength measured in (p,n) reactions with that obtained in β -decay, and this is another very good reason to measure β -decay, focusing on the determination of the $B(\text{GT})$ distribution.

Regarding the third point, we must now establish the regions of the nuclear chart where it makes sense to measure the $B(\text{GT})$ distribution in β -decay. It must be noticed that we are dealing with a forbidden process in general. In most of the existing nuclei the number of neutrons is bigger than the number of protons ($N > Z$). In this case the decay can not proceed through a Fermi process because it would not obey the isospin selection rule. On the other hand, allowed Gamow-Teller decay can only

³The first radioactive beams at SPIRAL (GANIL) and REX-ISOLDE (CERN) became available by the end of year 2001.

happen either if the spin-orbit partner of the initial proton⁴, or the same orbital of the initial proton are free on the neutron side. Furthermore, the final states which can be reached in the decay must lie inside the energy window available to the decay. These conditions are rarely found in $N > Z$ nuclei. However there are three regions of the nuclide chart where pure Gamow-Teller β^+ -decay is allowed: the $N \approx Z$ nuclei up to $A \approx 70-80$, the nuclei around the doubly magic nucleus ^{100}Sn , and the rare-earth nuclei around mass 150 (above the quasi-doubly magic ^{146}Gd). In Fig. 1.3 we see the possible *GT+Fermi* decays in some of the $N < Z$ cases, and the *pure GT* decay of the intruder orbitals $g_{9/2}$ and $h_{11/2}$.

The subject of our study is, on the one hand, the Gamow-Teller β^+ -decay of the $N=Z$ nucleus ^{76}Sr , in which the valence protons have free neutron orbitals with the same quantum numbers thus allowing the decay, and on the other hand the fast Gamow-Teller transition $h_{11/2} \rightarrow h_{9/2}$ in the nuclei around ^{146}Gd . In the ^{76}Sr case a big part of the GT resonance is expected to lie inside the Q_{EC} window. Theoretical calculations will allow us to determine the prolate or oblate character of its ground state based on the determination of the $B(\text{GT})$ distribution of its β^+ -decay. Everything regarding this decay is explained in the second part of this work. Around the quasi-doubly magic ^{146}Gd the main peak of the GT resonance will lie inside the Q_{EC} window thus allowing a good determination of the missing $B(\text{GT})$ in β^+ -decay. We will also report a systematic study of the $h_{11/2} \rightarrow h_{9/2}$ transition as a function of the number of protons in the $h_{11/2}$ orbital. The third part of this work is fully dedicated to this subject.

⁴Spin-orbit partner of an orbital on the proton side is the orbital on the neutron side with the same ℓ but one unit less in j

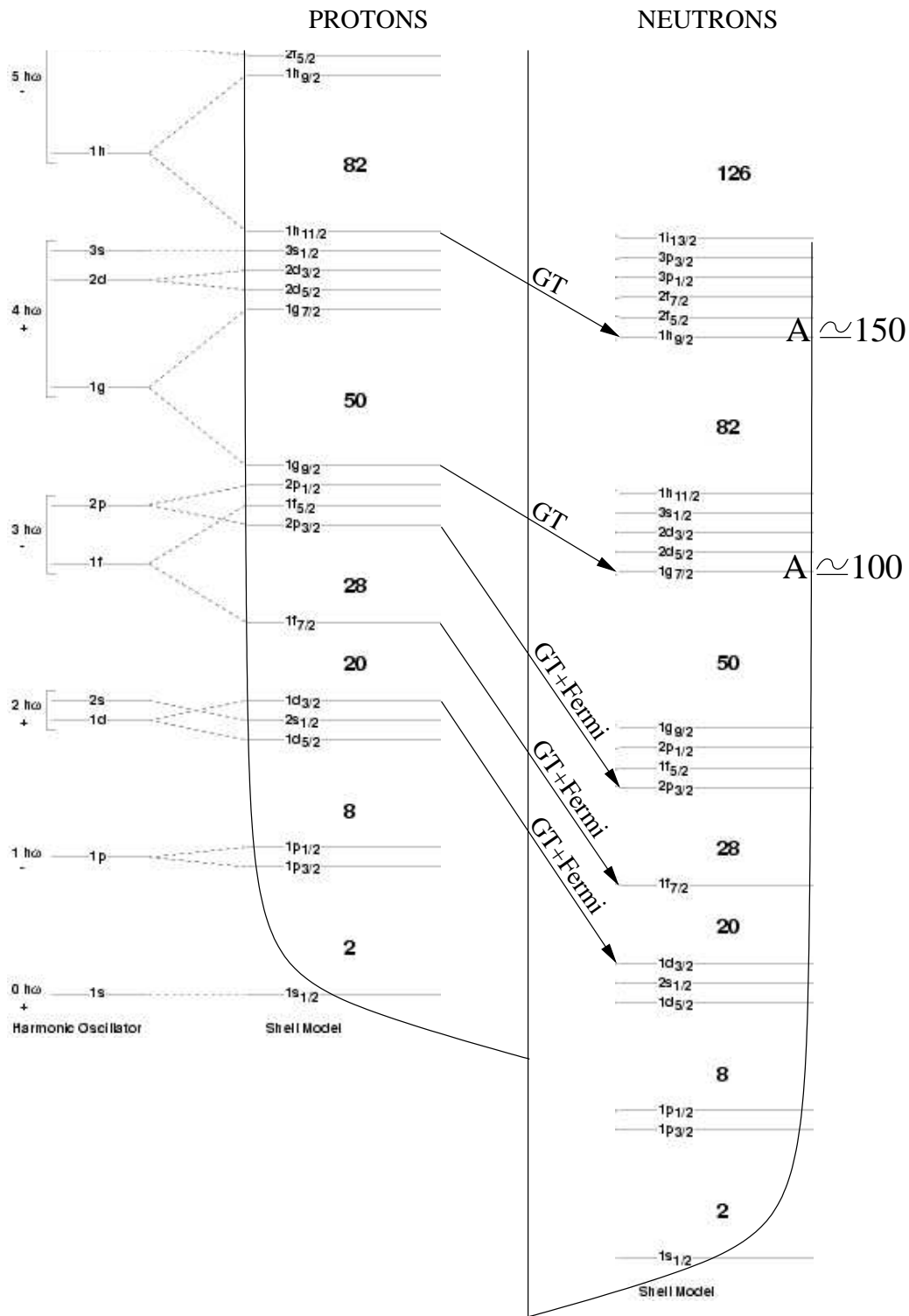


Figure 1.3: Allowed β^+ -decay in the nuclear chart: The $N \approx Z$ nuclei up to $A \approx 70-80$, the nuclei around the doubly magic ^{100}Sn , and the rare-earth nuclei around mass 150.

Chapter 2

Experimental techniques: High-resolution vs Total Absorption Spectroscopy

2.1 The GT strength distribution from β^+ -decay

In the previous chapter, the main aim of this work was presented: measuring the B(GT) distribution in the β^+ -decay of the N=Z nucleus ^{76}Sr and in the β^+ -decay of some nuclei in the rare-earth region above the ^{146}Gd core. However we have not yet presented the proper experimental method to do this. The first step forward in our understanding on how to obtain the B(GT) from our measurement is to express the GT strength in terms of other quantities that can be directly measured. For that reason we will define the β -strength function $S_\beta(E)$, which will be a function of the excitation energy in the daughter nucleus E . This quantity depends on the β -intensity $I_\beta(E)$ or feeding probability:

$$S_\beta(E) = \frac{I_\beta(E)}{f(Q_\beta - E) T_{1/2}} \quad (2.1)$$

Let us describe what we have in Eq. (12.5). The β -intensity $I_\beta(E)$ is just the probability (normalised to 1) of populating the level at energy E in the daughter nucleus when the β^+ -decay process happens. The function $f(Q_\beta - E)$ is the statistical rate Fermi integral, the so called phase space factor that depends on the energy available to the decay $Q_\beta - E$. Obviously $T_{1/2}$ is the half-life of the nucleus which is decaying, and therefore if we take the ratio $I_\beta(E)$ over $T_{1/2}$ what we have is the decay rate distribution in s^{-1} units. Now, if we divide this decay rate by the phase space factor, according to Fermi's Golden Rule, we are close to having the square of the matrix element of the operator responsible for the decay. To be precise, the quantity we have just introduced is an average quantity proportional to the mean value of the B(GT) for all the transitions populating the daughter nucleus at an excitation energy inside a certain energy bin ΔE which is defined by our experiment (or our

analysis). In other words: the B(GT) defined in Eq. (1.1) is a theoretical magnitude, the square of the GT matrix element between the initial and final states, whereas S_β is an experimental average quantity related to the former as follows:

$$S_\beta(E) = \frac{1}{6147 \pm 7} \left(\frac{g_A}{g_V} \right)^2 \sum_{E_f \in \Delta E} \frac{1}{\Delta E} \text{B(GT)}_{i \rightarrow f} \quad (2.2)$$

Eq. (2.2) gives us the recipe to exchange between the two different terminologies: the B(GT) and the S_β , the theoretical and experimental definitions of the strength.

2.2 How to measure the $I_\beta(E)$ distribution

From Eq. (12.5) it is clear that, in order to obtain the strength, one needs to measure the β -intensity, in other words, the probability that the decay populates a certain level of energy E in the daughter nucleus. We can distinguish between two different methods of carrying out such measurements: high-resolution spectroscopy (HRS) and total absorption spectroscopy (TAS). The former is based on the use of high-purity germanium detectors, with a very good energy resolution but a quite poor photo-peak efficiency. The latter implies the use of a big scintillator crystal (either NaI(Tl) or BaF₂) which has a very high efficiency but whose energy resolution is much worse than in the previous case. In both techniques the main objective is to measure the delayed γ -ray cascade which follows the β -decay.

2.2.1 The HRS technique and the “*pandemonium effect*”

In the HRS technique, due to the poor detection efficiency mentioned above, only a few γ -rays of the cascade will be detected, and very seldom the complete cascade. However, if all the γ -rays were observed, the energy of the levels in the daughter nucleus could be determined with a very high accuracy, and also the branching ratios from each level to the others. This is normally possible in the lower part of the level scheme. Once we know the energy of the levels and the relative intensity of each γ -ray observed in the decay, we can extract the $I_\beta(E)$ distribution just by imposing a γ -intensity balance criterion: the β -intensity to a certain level E_x is assumed to be the difference between the γ -intensity which de-excites the level E_x , and the γ -intensity which populates the level E_x from the de-excitation of the other levels above. Explicitly: $I_\beta(E_x) = I_\gamma^{\text{OUT}}(E_x) - I_\gamma^{\text{IN}}(E_x)$.

However, the efficiency of the germanium detectors is often not good enough to detect the entire gamma cascades and therefore in these cases it is impossible to have an accurate measure of the I_γ . This is especially known to happen for high energy γ -rays (e.g. 2-4 MeV) de-exciting the levels which lie in the upper part of

the level scheme of the daughter nucleus. In reality, it is the combination of three different effects that make this a difficult problem:

1. Due to the very low photo-peak efficiency, part of the γ -ray cascade following the decay remains undetected or lost in the Compton background of the spectrum, especially for high energy γ -rays ($E_\gamma \approx 2\text{-}4$ MeV).
2. In medium mass and heavy nuclei, the higher part of the level scheme has a very high level density, we can even talk about a quasi-continuum of energy levels. Therefore, in these cases the B(GT) can be very fragmented in the daughter nucleus and consequently the I_β will be very fragmented as well.
3. The subsequent γ -ray cascade after the β -decay can follow many different paths until the daughter nucleus arrives at its ground state. In other words, not only the I_β but also the de-excitation pattern can be highly fragmented.

In principle, as long as the photo-peak efficiency of the Ge detector is not zero and there are peaks in the spectrum for all the different gamma transitions, one should be able to correct for the first effect once the photo-peak efficiency is well known, but this is not possible if the other two effects are also present. The combination of the three effects results in a global shift of the I_β to lower energies and consequently a shift in the B(GT) as well as its global reduction. This limitation of the HRS measurements was first addressed by J.C. Hardy and collaborators in Ref. [19]. When talking about β -decay experiments performed with high resolution detectors the authors of Ref. [19] say: “...the derived β -decay branching ratios, for all but the strongest transitions, could be wrong by orders of magnitude.”, and afterwards state that this conclusion “...surely indicates the need to reevaluate the usefulness of a whole class of experiments.”. Taking into account that the authors reach this conclusions after the Monte Carlo simulation of a fictitious nucleus called Pandemonium, we will call this problem the *pandemonium effect*.

Fig. 2.1 shows a simplified recreation of this effect. Although it may look like a very naive oversimplification of reality, it is indeed very similar to the β -decay of the rare-earth nuclei around ^{146}Gd that are presented in this work. As we see in the figure, the β -decay of a certain nucleus populates its daughter at an excitation energy about 4.5 MeV, where the GT resonance has its maximum. Then, the most likely thing to happen is that a high energy γ -ray starts the de-excitation cascade, in this particular case γ_1 with $E \approx 3.5$ MeV. Due to the low photo-peak efficiency of Ge detectors for such a high energy, γ_1 will probably suffer a Compton scattering before escaping from the crystal. The second γ -ray of the cascade, γ_2 , has a lower energy, approximately 1 MeV, and therefore it has a good chance to be fully absorbed in the other Ge detector. When we detect such an event we tend to think that the original β -decay populated the daughter nucleus not at the position of the resonance but

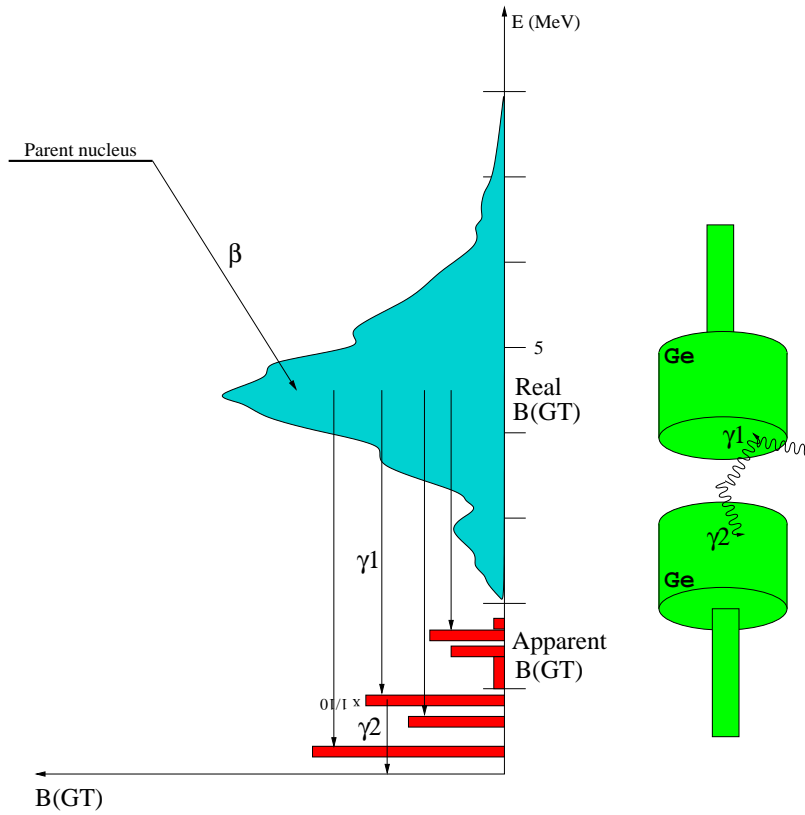


Figure 2.1: Comparison between the *apparent* $B(GT)$ obtained with Ge detectors with the real one. In the graph the vertical axes is the excitation energy in the daughter nucleus.

at the level at $E \approx 1$ MeV. Furthermore, the effect is exacerbated by the fact that, due to the high fragmentation of the $B(GT)$ in the region above 3 MeV (high level density), the first γ -ray will not always have the same energy, whereas the second de-excites a very well established level at low energy (low level density) and therefore will always have a well defined energy (e.g. 1 MeV in the case of the figure). This means that, after the detection of many events, γ_2 will produce a peak in the energy spectrum whereas γ_1 will not. Therefore we can make an efficiency correction for the peak at $E \approx 1$ MeV (and many other peaks at low energies), but we can not correct any peak at $E \approx 3.5$ MeV because it simply does not exist. In conclusion, with this kind of measurement, assuming the γ -intensity balance explained before, one ends up with an $I_\beta(E)$ distribution which is shifted to lower energies. Consequently it must be regarded as the *apparent* $I_\beta(E)$ or *apparent feeding*, stressing the fact that it is different from the real one. This systematic error is amplified as it propagates to the $B(GT)$ distribution because the Fermi integral becomes smaller as the energy increases, following a logarithmic dependence. Obviously one can not take very seriously the *apparent* $B(GT)$ distribution obtained from HRS experiments unless

they have been performed with a very efficient setup, and even in this case one must know the amount of B(GT) which remains unmeasured. For instance in Ref. [20] we have a β -decay experiment performed with six Ge cluster detectors in a very close geometry. The authors could identify 295 levels and 1064 γ -rays in the β -decay of ^{150}Ho , however they lost about 55% of the total B(GT) which was observed using the TAS technique as explained in next section. A similar effect was observed earlier in the β^+ -decay of ^{98}Ag (in the ^{100}Sn region) [21].

2.2.2 The Total Absorption Spectroscopy technique

To get rid of the *pandemonium effect* the Total Absorption Spectroscopy (TAS) technique has proved to be a very powerful tool [22]. In this case the main detector is designed to absorb the entire γ -cascades de-exciting the daughter nucleus after the β -decay rather than the individual γ -rays. In other words, the TAS detector acts as a calorimeter, absorbing the full energy released in the β -decay process. The main requirement for such a detector is a very large crystal which covers a solid angle of $\approx 4\pi$ around the radioactive source and made of an appropriate material with a high intrinsic efficiency for γ detection. These requirements can be very well fulfilled by a big NaI(Tl) or BaF₂ crystal with the appropriate shape. There are some technical problems to make a NaI(Tl) crystal grow to the right size, and it is even more difficult to cut the final crystal to give it the right shape, but it can be done. In ideal conditions a TAS detector can be represented schematically by Fig. 2.2. If the crystal covers the source completely and no extra material is placed inside, the cascade represented in the level scheme should be fully absorbed by the NaI(Tl) crystal, and from the directly measured spectrum we would be able to ex-

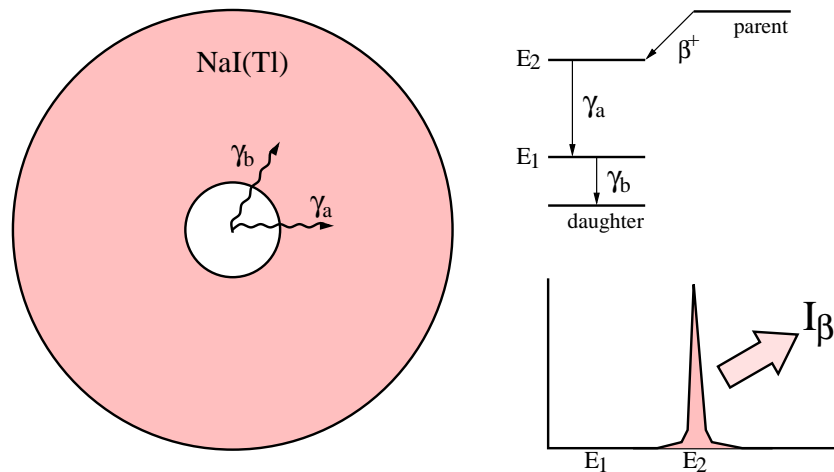


Figure 2.2: Ideal TAS: a very big NaI(Tl) detector covering a 4π solid angle around the radioactive source (left). From the direct spectrum one can obtain directly the $I_\beta(E)$ distribution.

tract the feeding distribution $I_\beta(E)$ just by deconvoluting the energy resolution of the crystal.

Reality is never so simple. We have to take into account that we are interested in measuring β^+ -decay and this competes always with the electron capture process. We may want to disentangle the spectra associated with the two processes, and therefore ancillary detectors must be placed around the radioactive source, typically a Ge planar detector for X-rays (this tags the EC processes) and a Si detector or a plastic scintillator for charged particles (this tags the β^+ processes). Furthermore, if we want to avoid the penetration of positrons in the NaI(Tl) crystal, so that it only detects the γ -cascade, then we have to add a piece of absorber such as polyethylene or Be. Unfortunately, all these modifications increase the amount of dead material very close to the radioactive source and lead to a decrease in the photo-peak efficiency of our TAS detector. In Fig 2.3 a realistic TAS with all this extra material is shown. A typical β^+ disintegration would again produce the same two γ -rays as before, but in this case we see that γ_b interacts with the Ge volume losing some energy before being absorbed in the NaI(Tl) crystal. Moreover, the positron annihilates with an atomic electron either in the absorber ring or in the Si detector producing two photons of 511 keV moving back-to-back. At the right side of the figure we have a very simple representation of the typical spectra that would be measured with the TAS main crystal in coincidence with the Ge detector (EC component) and with the Si detector (β^+ component). Due to the sum with the two 511 keV photons, in the β^+ spectrum, the main peaks are shifted 1022 keV with respect to the same peaks in the EC spectrum.

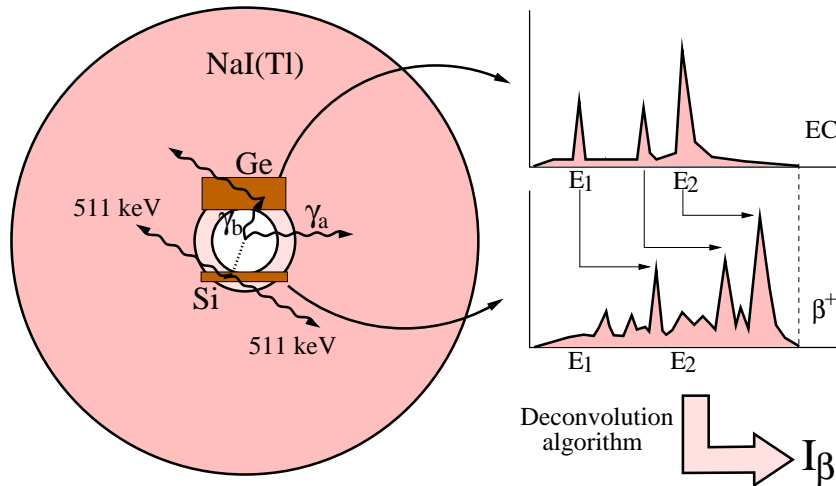


Figure 2.3: Real TAS: as soon as we place some dead material near the source the photo-peak efficiency of the detector decreases and escape peaks and a continuum appear in the measured spectrum.

Apart from the sum peaks, in both EC and β^+ spectra we observe the escape peaks and the Compton continuum which did not appear in the ideal TAS of Fig. 2.3. Although the photo-peak efficiency of the real TAS is not 100% anymore, its total efficiency is almost 100%. This means that for almost every decay the TAS detector registers one count in its spectrum. This count will lie in the sum peak in the best case, in a single escape peak in some other cases, in a double escape peak, or in the Compton continuum. There are several different methods to deconvolute the measured spectrum to obtain the I_β distribution. However it must be clear at this stage that it is thanks to the fact that the total efficiency of the TAS is close to 100% that we can unfold the experimental data, putting the counts that are not in the total absorption peak back in their proper channel. In the next chapter we explain one of those methods of deconvolution.

Chapter 3

The data analysis method

3.1 The Expectation maximisation (EM) algorithm

In the previous chapter it was mentioned that, if our TAS detector had 100% peak efficiency, we would measure directly the β -intensity or feeding distribution $I_{\beta(E)}$ affected only by the energy resolution of the crystal. Unfortunately, the dead material placed around the radioactive source near the centre of the crystal lowers the peak efficiency and then we can not measure $I_{\beta(E)}$ directly anymore. The procedure to extract $I_{\beta(E)}$ from our measured spectrum is usually called deconvolution or unfolding. We would like to have all our counts in the sum peaks corresponding to the levels which are fed by the β -decay, however many of these counts are placed in the escape peaks or the Compton continuum. By unfolding the data we can put all these counts back in their right position, the sum peak, and then obtain $I_{\beta(E)}$ by correcting for energy resolution.

In the following discussion we regard the β -intensity distribution as *feeding* and it is represented by f in the equations. We can expose the problem in the following way: the number of counts that we have in the channel i of our spectrum is equal to the number of events that fed the level j in the daughter nucleus after the decay, multiplied by the probability that feeding to the level j gives a count in the channel i :

$$d_i = \sum_{j=1}^{j_{max}} R_{ij} f_j \quad (i = 1 \dots i_{max}) \quad (3.1)$$

The probability we have mentioned is, by definition, the response function of the detector for feeding to the level j , and this is the reason why we called it R_{ij} . This response function is unique to each detector and each decay scheme. It is possible to calculate R_{ij} from the responses to individual gamma-rays [23]. Due to the lack of mono-energetic gamma sources, the only way to obtain such individual responses

is by means of Monte Carlo simulation. For the detectors we used in our experiments either at GSI or at CERN, the simulations were performed using the code *GEANT4* [24]. In order to give an idea of how detailed the simulations are, Fig. 3.1 taken from Ref. [23] shows part of the geometry implemented for the GSI-TAS detector.

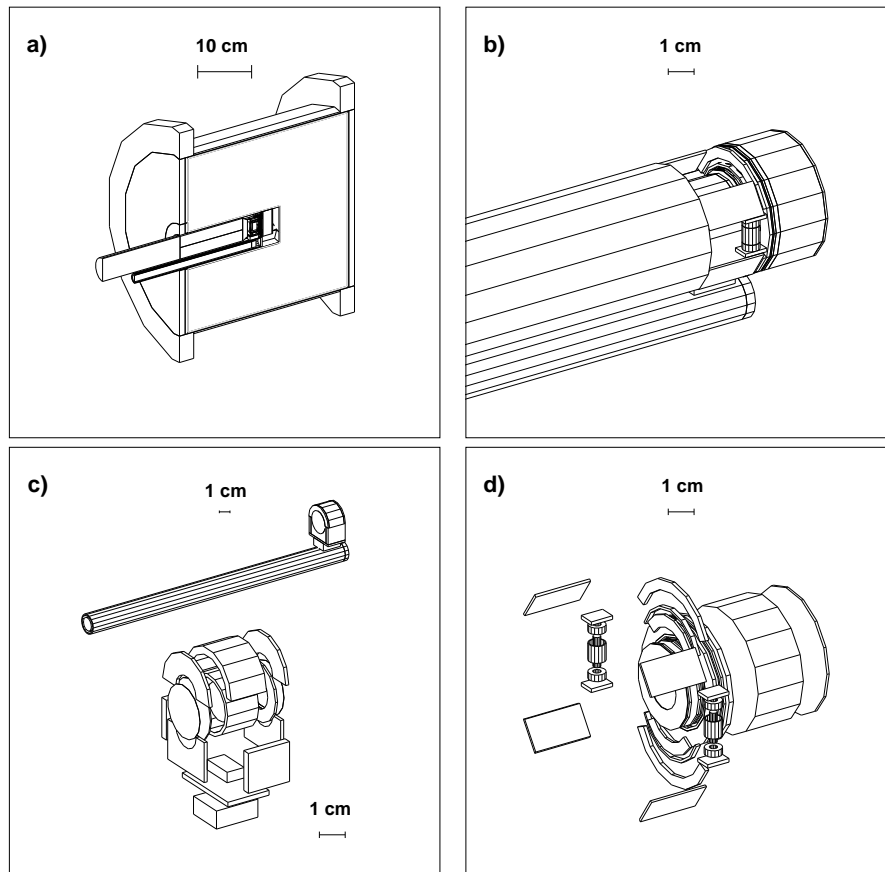


Figure 3.1: Details of the GSI TAS geometrical description in GEANT4. a) Longitudinal cut along the spectrometer showing the main crystal and the plug detector. b) Plug detector with ancillary detectors and absorber. c) Upper part: Ge detector cryostat and cold finger; lower part: Ge crystal and capsule. d) Mounting of the Si detectors and transport tape rollers together with the polyethylene absorber

At this point we have to face the following problem: even though we can measure the data and calculate the response function of the decay by means of Monte Carlo simulations, we still need to extract the feeding distribution solving the inverse problem defined by Eq. (3.1). The first and most direct approach to solve the problem would be simply to invert the response matrix R_{ij} , but this is not that easy. The main problem is the following: the response matrix R_{ij} is nearly singular,

in other words, it has nearly-degenerate columns due to the fact that the detector has a very similar response to the feeding to contiguous energy bins. This problem causes many calculational difficulties such as computer round-off errors, overflows, etc.

If we can not invert the response matrix, what we have to do is to use the appropriate method to solve the inverse problem given in Eq. (3.1). A large set of algorithms have been devised with this aim. In Ref. [25] an exhaustive study of three of these different algorithms is performed specifically for the TAS data. One of them is the Expectation-Maximisation (EM) method [26]. There are some other methods such as the Linear Regularisation or the Maximum Entropy methods, but we will use the first one because quoting the conclusions of Ref. [25]: “...it is easy to implement and the solutions found are always positive because the method intrinsically deals with probabilities. They do not depend on the arbitrary election of a parameter and the convergence of the method is very fast.”. For these reasons we decided to use this method.

The algorithm can be obtained by substituting the fundamental theorem of conditional probability, namely the Bayes theorem (3.2) in the definition of the inverse problem written in terms of probabilities (3.3). This was not the original way to arrive at the EM algorithm but it is very intuitive as shown by D’Agostini in Ref. [27]. In terms of causes and effects the Bayes theorem can be enunciated as follows: if we observe a single event (effect), the probability that it has been due to a certain cause is proportional to the probability of the cause times the probability that the cause produces the effect. If we identify the feeding as cause and the count as effect we can then say: the probability of having one count in the channel i due to feeding to the energy bin j is equal to the probability of having feeding to the energy bin j times the probability that feeding to the bin j gives counts in the channel i :

$$P(f_j|d_i) = \frac{P(d_i|f_j)P(f_j)}{\sum_{j=1}^m P(d_i|f_j)P(f_j)}, \quad (3.2)$$

where the denominator appears to ensure that the probability is normalised to 1. The inverse problem defined in (3.1) can be written as:

$$f_j = \frac{1}{\epsilon_j} \sum_{i=1}^n P(f_j|d_i)d_i, \quad j = 1, \dots, m, \quad (3.3)$$

where ϵ_j is the efficiency of the detector for feeding to a certain bin j (again it appears just for normalisation reasons), and in the second factor we have the inverse of the response matrix but written as the probability that we measure one count in channel i due to feeding to the channel j . Now we can substitute (3.2) in (3.3) and obtain the expression:

$$f_j = \frac{1}{\epsilon_j} \sum_{i=1}^n \frac{P(d_i|f_j)P(f_j)}{\sum_{j=1}^m P(d_i|f_j)P(f_j)} d_i, \quad j = 1, \dots, m, \quad (3.4)$$

which is already the EM algorithm, but we can rewrite it identifying the probability that feeding to bin j gives counts in channel i with the response matrix, and the efficiency for feeding to j with the response matrix for feeding to bin j summed for all the possible channels i . Then we get:

$$f_j = \frac{1}{\sum_{i=1}^n R_{ij}} \sum_{i=1}^n \frac{R_{ij} \hat{f}_j}{\sum_{k=1}^m R_{ik} \hat{f}_k} d_i, \quad j = 1, \dots, m \quad (3.5)$$

We can start for example with a flat probability distribution of feeding \hat{f}_j . Then we substitute it in (3.5) and obtain a first estimate of the feeding distribution f_j using the *a priori* information given by the data d_i . After normalisation we have the new probability distribution of feeding \hat{f}_j to substitute again in (3.5) and this allows us to calculate a new estimate for the feeding distribution f_j . In Eq. (3.5) the \hat{f}_j on the right side has a hat because it is normalised to 1, whereas the f_j on the left side has no hat because it is not normalised, in fact, thanks to the denominators which normalise the probabilities, the solution f_j has the same number of counts as the measured spectrum d_i . We can then re-write Eq. (3.5) for each iteration s to stress that it represents an iterative process:

$$f_j^{(s)} = \frac{1}{\sum_{i=1}^n R_{ij}} \sum_{i=1}^n \frac{R_{ij} \hat{f}_j^{(s-1)}}{\sum_{k=1}^m R_{ik} \hat{f}_k^{(s-1)}} d_i, \quad j = 1, \dots, m \quad (3.6)$$

To check the convergence of the iterative algorithm one must multiply the response function R_{ij} by the solution f_j and, according to Eq.(3.1), this product should be very similar to the original spectrum d_i . In our cases ≈ 200 iterations are enough to have a solution which do not improve, in terms of χ^2 , anymore.

3.2 The problem of the subtractions

So far we have explained how to analyse a spectrum where we have counts only coming from the decay of interest. Obviously it is impossible to measure just such a decay and not some undesired activity coming from the parent or daughter of the decay of interest, the room background, and the unavoidable electronic pile-up. Thus, in order to apply the EM algorithm to our data we have to make sure that we take into account these unwanted components properly.

Measuring the parent or daughter activity is not a problem in general, we just have to change the cycle of the tape transport system, or simply put a gate in the appropriate X-rays if we are analysing the EC process. Calculating the pile-up spectrum is somewhat more complicated. We have used a numerical method that

uses the real signal that we are accepting in our ADCs. The method is explained in Ref. [28]. In this article the authors assume that there is only first-order pile-up, that means, any contribution due to the summing of three signals is neglected. It is also assumed that the time of pulse arrival at the ADC follows the Poisson probability distribution, and the ADC will process the first maximum of the composite pulse. With these assumptions, completely fulfilled in the case of our TAS measurements, the pile-up calculation is made by convoluting the real pulse shape with itself for the different channels of our spectrum, that means, different pulse heights. In the case of coincidence spectra the convolution of the pulse shape is made between the channels of the coincidence spectrum and the total TAS spectrum measured without any condition (in singles).

Once we have the spectra corresponding to the undesired activities and the pile-up, we have to determine the normalisation factors to make the subtractions. If we are not dealing with coincidence spectra, then the first factor to determine is that corresponding to the background. For this we can use the upper part of the spectrum far from the end point (Q_{EC}) of all the decays involved in the measurement and also the end point of the pile-up. Then we have to calculate the factor to subtract the background giving zero counts in this upper region. Afterwards we should proceed in a similar way with the pile-up. In this case we select a region beyond the biggest Q_{EC} value of our spectrum (already free of background). For the unwanted activities it depends on the case. If $Q_{EC}^{undesired} > Q_{EC}^{decay}$ then it is clear that, once we have subtracted pile-up, we can use the region beyond the Q_{EC}^{decay} to normalise. If this is not the case, the situation is more critical. One possibility is to identify a peak in the TAS spectrum belonging to the unwanted activity and subtract this contribution normalising to the number of counts of the peak. Sometimes we can use the ancillary Ge detectors to determine the amount of contamination by comparing the intensities of some particular γ transitions. Another alternative is to estimate from the cycle time how much parent or daughter activity is present in our samples, but this is difficult in general.

In principle, one should now be able to make a clean subtraction using the normalisation factors and afterwards analyse the data. However there is still a problem to solve. As we have subtracted spectra with statistical fluctuations, in the regions of low statistics we can have channels with zero or even negative counts. This is a big problem because on the one hand the EM algorithm can only deal with positive counts in the spectrum, and on the other hand, having fluctuations is especially critical in the region of very low statistics near the Q_{EC} value, not only because we have very few counts and large oscillations, but also because, due to the Fermi integral, in this region the strength calculation is very sensitive to any count. This means that a small fluctuation in the data due to the subtraction can give some non-real counts or remove some real counts in the feeding spectrum, which implies a huge amount of non-real strength when we divide by the phase space factor (Fermi

integral).

How can we solve this problem? One possible solution is to avoid making any subtraction. If we do not want to subtract anything, we need to take into account the undesired activity and the pile-up at the level of the analysis algorithm. To better understand this we have to look at Eq. (3.5). What we have in the denominator of the second term of the equation is just the definition of the probability of having data in the channel i . We will denote this as \hat{d}_i to distinguish it from the real measured data d_i :

$$\hat{d}_i = \sum_{k=1}^m R_{ik} \hat{f}_k \quad (3.7)$$

In our algorithm we can now substitute this by a new definition of probability of data which takes into account the background, undesired activity and electronic pile-up as if they were just a constant:

$$\hat{d}_i = Fact1 \times \sum_{k=1}^m R_{ik} \hat{f}_k + Fact2 \times (Und.Activity)_i + Fact3 \times (Pile-up)_i \quad (3.8)$$

If we assume such a definition for the probability of data, then when we apply the algorithm (3.5) we must use for d_i the spectrum that contains the pile-up and the undesired activity. In this case we will not have the problem of the fluctuations due to the subtractions. However it is important to note that we still have to calculate the normalisation factors. We do not make the real subtraction but the normalisation factor must be calculated anyway to take it into account in the analysis algorithm.

The effect of avoiding subtractions is illustrated in Fig. 3.2. What we see is a comparison between the same analysis making subtractions (left side) and taking into account the undesired components of the spectrum in the analysis program (right side). The upper part of the figure shows the measured spectrum once we have subtracted the pile-up and the undesired activity (grey shade), and the recalculated spectrum (dashed line) overlaid on the former. This recalculated spectrum results from the product of the response matrix and the feeding distribution obtained from the analysis, and it should reproduce the measured one. In the lower part we present the feeding distributions obtained with the two methods. Obviously the analysis without subtractions leads to something smoother and without fluctuations whereas the analysis with subtraction gives something unphysical at the end of the spectrum due to statistical fluctuations. For this check we used the analysis of the decay of $^{148}\text{Tb}(9^+)$ that will be described in Sec. 3.4.2.

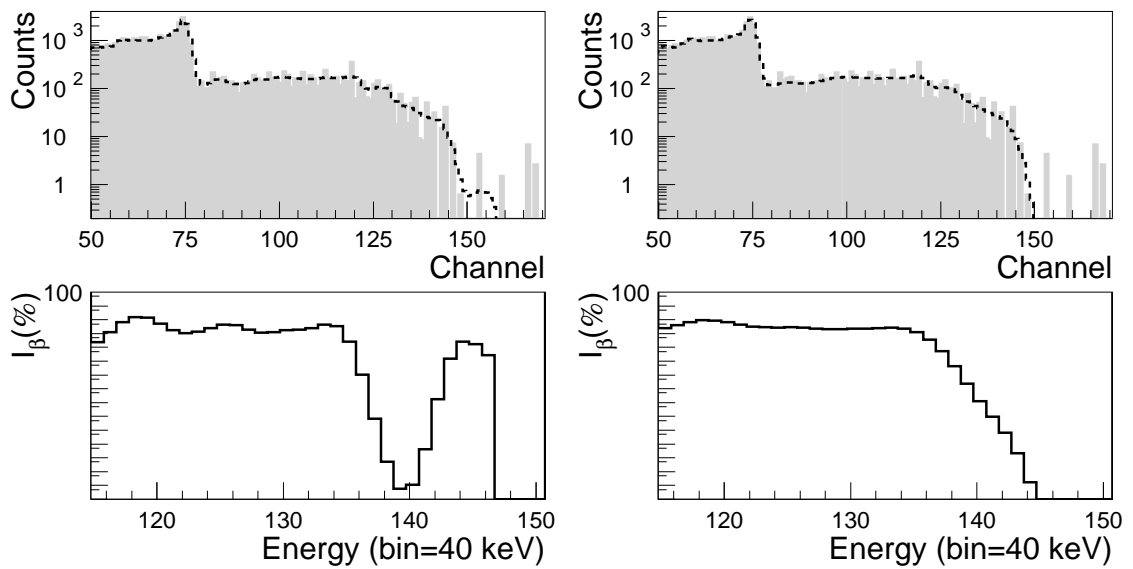


Figure 3.2: Comparison between the analysis made subtracting pile-up and undesired activity (left), and the analysis taking into account these unwanted contributions in the analysis program, without any subtraction (right).

Part II

The N=Z nucleus ^{76}Sr

Chapter 4

The nuclei with $A \approx 70-80$ in the vicinity of the $N=Z$ line

4.1 Deformed nuclei

4.1.1 Quadrupole moments

The first probe one can use to determine the shape properties of a charge distribution is the value of its electric quadrupole moment. For a single proton in an orbital defined by the wave function ψ , we can calculate the electric quadrupole moment as:

$$eQ = e \int \psi^*(3z^2 - r^2)\psi dv \quad (4.1)$$

If $|\psi|^2$ has spherical symmetry, then $Q = 0$ because $\langle x^2 \rangle = \langle y^2 \rangle = \langle z^2 \rangle = \frac{1}{3}\langle r^2 \rangle$ and the integral in 4.1 obviously vanishes. For the particular case of a nucleus with even N and odd Z , if we assume that the paired nucleons move in spherically symmetric orbitals (they do not contribute to the value of Q) and that the odd proton lies near the surface of the nucleus, then we can estimate $|Q| \lesssim \langle r^2 \rangle = R_0^2 A^{2/3}$, which ranges from 0.06 barn in light nuclei to 0.5 barn in heavy nuclei. The measurements of Q for the stable nuclei give results inside this range for many nuclei, but there are several exceptions such as the stable nuclei in the rare-earth region (e.g. $Q \approx 3.5$ barn for the stable ^{165}Ho , ^{167}Er and ^{175}Lu). This means that we can not assume a spherical core of paired nucleons for these cases and therefore we must consider deformation of the nuclear surface.

4.1.2 Deformation parameters

In order to characterise the surface of the nucleus and its possible deformation, we will start by expanding the length of the vector pointing from the origin to the nuclear surface, $R(\theta, \phi)$, in the base of the spherical harmonics $Y_{\lambda\mu}(\theta, \phi)$:

$$R(\theta, \phi) = R_0 \left(1 + \alpha_{00} + \sum_{\lambda=1}^{\infty} \sum_{\mu=-\lambda}^{\lambda} \alpha_{\lambda\mu} Y_{\lambda\mu}(\theta, \phi) \right) \quad (4.2)$$

If we require that the volume of the nucleus is kept fixed, the term α_{00} must be constant and thus incorporated into the average radius R_0 . The term $\lambda = 1$ describes a translation of the whole system, i.e. a net displacement of the centre-of-mass. This does not affect the shape of the nucleus and we can then remove this term from (4.2). Therefore, the expansion (4.2) starts with $\lambda = 2$: the quadrupole deformation. For higher orders in λ we will have octupole deformation ($\lambda = 3$), hexadecupole deformation ($\lambda = 4$), etc.

For transitional nuclei which are not deformed very strongly it may be necessary to consider axially asymmetric (triaxial) shapes, but for well deformed nuclei it is a good approximation to consider only axially symmetric nuclear shapes. Thus, in the following we will restrict ourselves to axially symmetric deformations¹. In this case, choosing the z -axis as the symmetry axis, the deformation parameters $\alpha_{\lambda\mu}$ vanish except for $\mu=0$, and it is common to use the notation $\alpha_{\lambda 0} = \beta_{\lambda}$. For the case of quadrupole deformations we will talk about β_2 , considering the higher orders of deformation to be negligible. After all these considerations one can re-write (4.2) as:

$$R(\theta, \phi) = R_0 (1 + \beta_2 Y_{20}(\theta, \phi)) \quad (4.3)$$

The relationship between the electric quadrupole moment and the deformation parameter β_2 is:

$$Q = \frac{3}{\sqrt{5\pi}} R_{av}^2 Z \beta_2 (1 + 0.16\beta_2), \quad \text{with } R_{av} = 1.2A^{1/3}(\text{fm}) \quad (4.4)$$

The nuclei with $\beta_2 > 0$ have a prolate shape (right part of Fig. 4.1) and positive electric quadrupole moment, whereas the nuclei with $\beta_2 < 0$ have an oblate shape (left part of Fig. 4.1) and negative electric quadrupole moment.

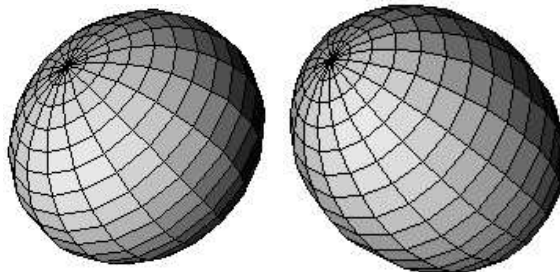


Figure 4.1: Oblate (left) and prolate (right) spheroids.

¹For a deeper treatment of triaxial shapes one can follow Ref. [29]

4.2 General features of the region

The neutron-deficient nuclei with $A \approx 70-80$ are the heaviest nuclei one can study in which protons and neutrons occupy the same orbitals ($N \approx Z$). This region of the nuclear chart is characterised by different shape effects such as strong deformation in the ground-state, shape transitions and shape coexistence. These three effects are exhibited by the light Sr isotopes, which evolve from sphericity at $N=50$ to large deformation (presumably prolate) at $N=40$. In the lower part of Fig. 4.2 (taken from Ref. [30]) we see the experimental energy of the first 2^+ state, $E(2^+)$, for all the even-even, $N=Z$ nuclei from Ge to Mo. This $E(2^+)$ is connected to the quadrupole deformation of the nucleus β_2 by Grodzin's empirical formula:

$$|\beta_2| \approx \left(\frac{1225}{A^{7/3} E(2^+)} \right)^{1/2} \quad (4.5)$$

Therefore, from the experimental $E(2^+)$ values that we have in Fig. 4.2 one can estimate the deformation parameter β_2 using Eq. 4.5, and this is shown in the upper part of the figure (dashed line). In reality the deformation parameter shown in the figure is ε_2 , but this is proportional to the β_2 that we have in Eq. 4.5: $\varepsilon_2 \approx 0.95\beta_2$. We can see that the maximum deformation in the region belongs to ^{76}Sr . The experimental $E(2^+)$ for the ^{76}Sr case is taken from Ref. [31]. The value $E(2^+)=261$ keV indicates, according to Eq. 4.5, that ^{76}Sr is strongly deformed with $|\beta_2| > 0.4$. However, Eq. 4.5 does not give any information on the sign of β_2 .

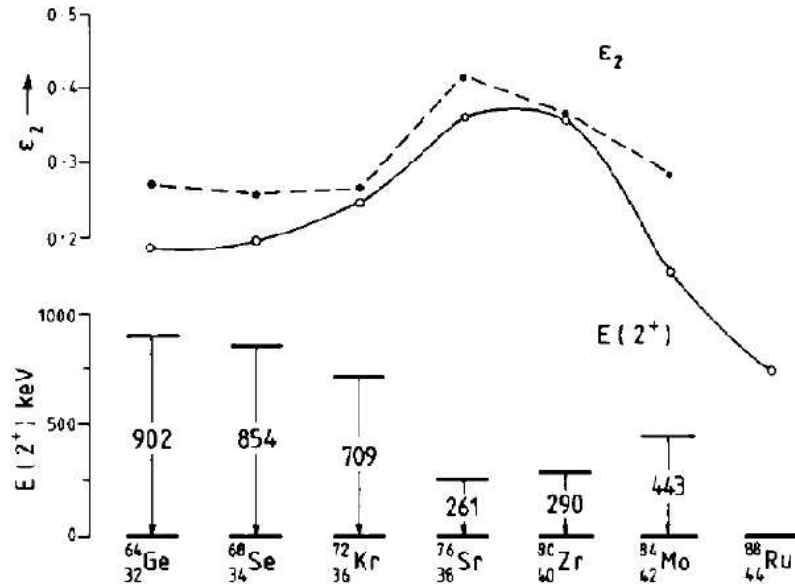


Figure 4.2: Bottom: Experimental $E(2^+)$ for the even-even, $N=Z$ nuclei from Ge to Mo. Top: Quadrupole deformation ε_2 derived from Grodzin's formula (dashed line) and other theoretical estimation (solid line).

According to Hamamoto *et al.* [32] and Sarriguren *et al.* [33], one can study the deformation (including the sign) of the ground-state of a particular nucleus by measuring the B(GT) distribution for its β -decay. In these references the authors calculate the B(GT) distribution for various nuclei in the region assuming different deformations for the ground-state. In some cases, the results differ markedly with the shape of the ground-state of the parent, especially for the light Kr and Sr isotopes. The first attempt to extract some information about the shape of the ground-state of ^{76}Sr from its β -decay is that described in Ref. [34]. Unfortunately, due to the lack of efficiency of HPGe detectors and its consequent effects described in Sec. 2.2.1, the authors could only give an indication of the prolate character of ^{76}Sr but not a conclusive proof.

The aim of the present work is to measure the β -decay of ^{76}Sr with a total absorption spectrometer, and to extract the B(GT) distribution with enough accuracy to compare with the theoretical calculations of Ref. [35, 36]. In this way the shape of the ground-state of ^{76}Sr will be determined without ambiguity. In the next section the calculation method of Ref. [33, 35, 36] is summarised, and in Chap. 7 the calculations will be used to compare with our experimental results.

4.3 Self-consistent Hartree-Fock + BCS + QRPA formalism in deformed nuclei

In this section a short summary of the theoretical approach used in Refs. [33, 35, 36] is given. The starting point of the calculation is the construction of the quasi-particle basis using the Hartree-Fock (HF) approach with the inclusion of pairing correlations in the BCS approximation. The two-body interaction used in the HF calculation is a density-dependent Skyrme force. In particular two different interactions have been used: the Sk3 which is the most extensively used Skyrme force, and the SG2 which is known to give a good description of Gamow-Teller excitations in spherical nuclei. In this work the experimental results are compared with the theoretical calculation performed with the Sk3 force. In order to construct the basis, the HF equations are solved iteratively using the McMaster code based on Ref. [37]. At the end of each HF iteration the BCS equations are solved to determine the Fermi levels and occupation probabilities.

The result of the HF + BCS calculation is the Slater determinant of lowest energy. If one wants to include the possibility of shape coexistence the approach must be extended to a constrained HF theory with a quadratic quadrupole constraint [38], where the minimisation of the HF energy is performed under the constraint of holding the nuclear deformation fixed. With this approach one gets a solution for each value of the quadrupole deformation. Fig. 4.3, taken from [35], shows the total HF energy as a function of the mass quadrupole moment for the even-even $^{76-82}\text{Sr}$

isotopes. In the cases where we observe more than one local minimum, shape co-existence is expected. The N=Z nucleus ^{76}Sr presents two minima: one oblate with $\beta_2 \approx 0.1$ and the other prolate with $\beta_2 \approx 0.4$. The separation in energy of these two minima is 4 keV when the mean field is derived from the SG2 interaction and 2.2 MeV when the Sk3 interaction is used. Thus, the SG2 interaction would allow shape mixing in the ground-state, whereas the Sk3 interaction results in a pure prolate ground-state. According to other microscopic calculations [39, 40] the ground-state of ^{76}Sr is expected to be pure prolate.

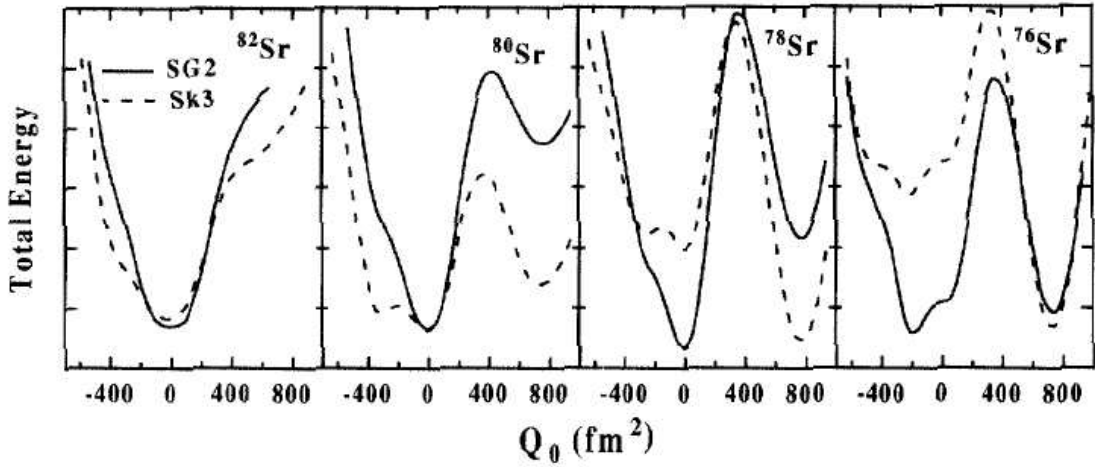


Figure 4.3: Hartree-Fock energy as a function of deformation (quadrupole moment) for the light Sr isotopes.

Once the basis is established, one has to derive the residual interaction and solve the QRPA equations. To describe Gamow-Teller transitions a spin-isospin residual interaction must be added to the mean field. This interaction contains two parts: particle-hole (ph) and particle-particle (pp). The ph part, which is derived self-consistently from the same Skyrme interaction used in the HF calculation, determines the position and structure of the GT resonance. The pp part is a neutron-proton pairing force in the $J^\pi=1^+$ coupling channel. Using this residual interaction the GT transitions are calculated in the QRPA approach for the nuclear shapes that minimise the HF energy. The method is self-consistent in the sense that both the mean field for the HF calculation, and the particle-hole residual interaction which generates the QRPA modes are derived from the same two-body interaction. The GT strength distributions calculated for the even-even $^{76-82}\text{Sr}$ isotopes are presented in Fig. 4.4 which has been taken from Ref. [36]. In order to compare with experimental results and to take into account other spreading mechanisms such as configuration mixing, the results have been folded with a Gaussian function (width=1 MeV).

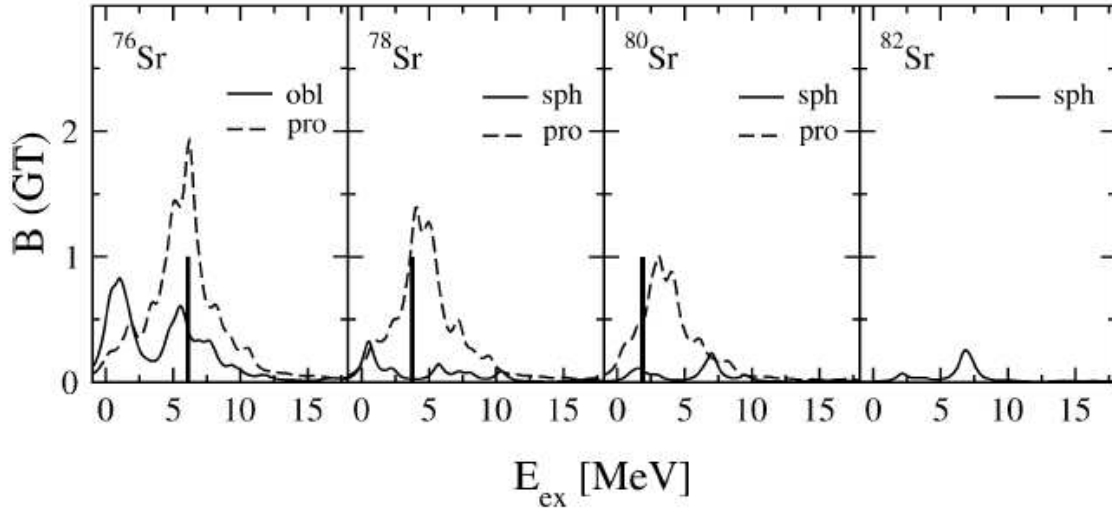


Figure 4.4: Calculated Gamow-teller strength distributions in $g_A^2/4\pi$ units as a function of the excitation energy of the daughter nucleus [36]. The calculations have been performed assuming different shapes for the parent nucleus (the shapes that minimise the HF energy). The results from the QRPA calculation have been folded with a Gaussian curve of width=1 MeV.

4.4 The N=Z nucleus ^{76}Sr

Among all the nuclei with $A=70-80$ in the vicinity of the $N=Z$ line we have measured the β -decay of the light Kr and Sr isotopes. The main reason is that for these two series of isotopes the calculations of Ref. [32, 41] and Ref. [33, 35, 36] conclude that the $B(\text{GT})$ distribution is markedly different for different shapes of the parent nucleus. Among all the cases studied in those references, the $N=Z$ nucleus ^{76}Sr is of particular interest for the following reasons:

1. Either in [32, 41] or in [35, 36] the decay of ^{76}Sr presents the biggest difference between prolate and oblate shapes in terms of the $B(\text{GT})$ distribution.
2. Although shape coexistence is predicted in this nucleus [39, 40, 35], microscopic calculations [39, 40] predict a pure, prolate ground-state. In contrast, other nuclei in the region (e.g. ^{72}Kr and ^{74}Kr) are expected to present shape mixing in the ground-state [42]. Therefore ^{76}Sr is a clean case, free of shape admixtures and other shape effects [43], which means that it is the best case to test the method of deducing the sign of the deformation from the $B(\text{GT})$ distribution.
3. It was already predicted in Ref. [44] that $N=Z$ nuclei above ^{56}Ni might decay to a GT resonant state inside the Q_{EC} window. Such a decay is called a “super-allowed” Gamow-Teller in [44].

4. Previous experimental work has shown that ^{76}Sr is the most deformed nucleus in the region with $|\beta_2| \approx 0.4$ [31]. However the sign of this strong deformation could not be deduced in that work.
5. Together with ^{72}Kr , ^{76}Sr is one of the N=Z waiting points for the astrophysical rp-process above Z=32. The only possible significant delays in the time structure of the rp-process above Kr are the β -decays of ^{76}Sr , ^{80}Zr and ^{81}Zr [45]. The B(GT) distribution in the decay of those nuclei are thus important for network calculations [45].

Chapter 5

The experiment

5.1 The ISOLDE mass separator at the PS-Booster

ISOLDE is the Isotope Separator On-Line DEvice installed at CERN. The main purpose of such a device is to produce radioactive isotopes in spallation, fission or fragmentation reactions and separate them according to their mass. Since 1992 this facility is sited at the PS accelerator complex at CERN and receives protons accelerated up to 1.4 GeV by the PS-Booster.

The PS-Booster (PSB) is in reality a stack of four small synchrotrons. These receive the protons delivered by a Linac at 50 MeV and accelerate them up to 1.0 or 1.4 GeV. The accelerated protons are then transferred either to the PS ring or to the ISOLDE target areas. The PSB gives one pulse of $\approx 3 \times 10^{13}$ protons every 1.2 seconds. Each of these proton pulses lasts for $2.4 \mu\text{s}$. In the time structure of the PSB the proton pulses are grouped in super-cycles containing 14 pulses which last 16.8 s. These 14 proton pulses of each super-cycle may be shared between the ISOLDE target area and the PS accelerator. The time structure of the PSB is shown in Fig. 5.1, whereas Fig. 5.2 shows the PSB layout together with a picture of one section of the accelerator ring.

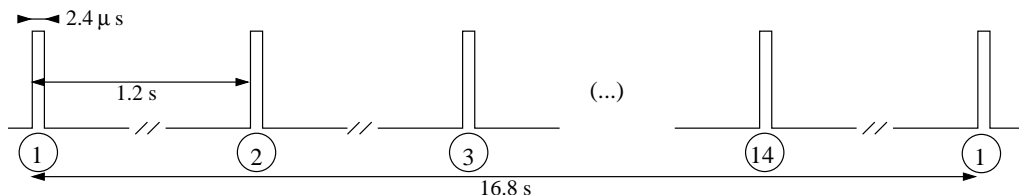


Figure 5.1: Time structure of the PS-Booster. Each pulse contains $\approx 3 \times 10^{13}$ protons.

After acceleration, the proton pulses leave the PSB through a transfer line to be injected in the PS synchrotron or to bombard one of the ISOLDE targets. Nowadays

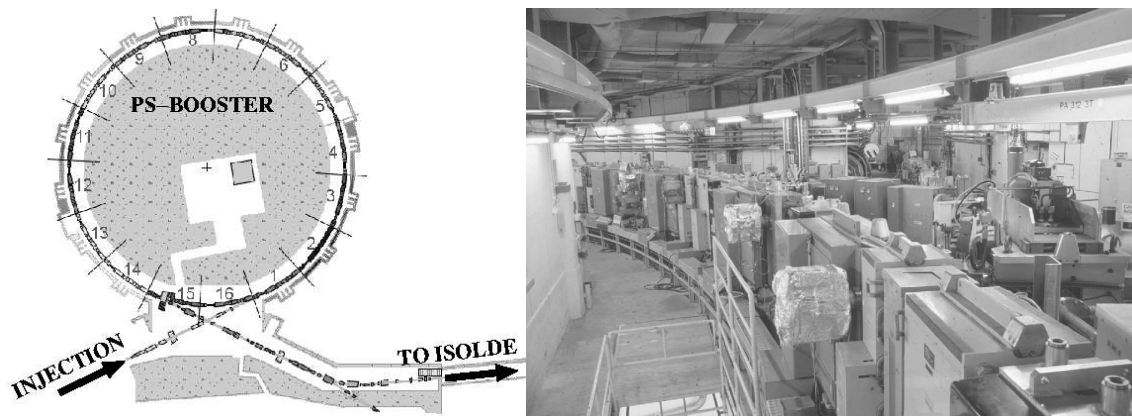


Figure 5.2: The PS-Booster accelerator at CERN.

the ISOLDE target area holds two different target stations each of them coupled to one of the two separators available at ISOLDE, namely the GPS and the HRS separators which will be described later. The production of the isotope of interest takes place by spallation, fission or fragmentation reactions induced by the collision of the 1 or 1.4 GeV protons in the target. For the production of ^{76}Sr we used a 52 g/cm^2 Nb target bombarded by 1.4 GeV protons. In order to ionise the products to allow their extraction one has to couple the target to an ion source. There are three different types of ion source which can be mounted in the ISOLDE target stations: surface ion source, plasma ion source and laser ion source. For our measurement the surface ion source was the most appropriate. It consisted of a metal tube, the line, made of tungsten, which has a higher work function than the atom or molecule that should be ionised. The line was heated up to $2100 \text{ }^\circ\text{C}$ to produce thermo-ionisation of the reaction products. To suppress the release of isobaric contaminants out of the ion source (mainly ^{76}Rb), a fluorination technique was used [46, 47, 48]: a certain amount of CF_4 gas was introduced into the cavity and SrF molecules were produced and thermo-ionised on the hot surface. However, RbF can not be produced for chemical reasons, and here lies the power of this fluorination technique to suppress the contaminants by a factor of 10^{-5} or lower. The SrF^+ molecular ions (and any other ion in the hot cavity) were then extracted from the ion source with a 60 kV potential, entering then in the first bending magnet of the High Resolution Separator (HRS).

The High Resolution Separator (HRS) is one of the two magnetic spectrometers installed at ISOLDE. It consists of two bending magnets with angles 90° and 60° which allow the selection of one single mass with a resolution of about $M/\Delta M=5000$. By setting the appropriate magnetic field in the two magnets a clean $^{76}\text{Sr}^{19}\text{F}^+$ ion beam could be separated and steered to our measuring station, which is described in next section.

5.2 Lucrecia, the TAS at ISOLDE

With the aim of measuring the β -decay of nuclei far away from the stability line with the Total Absorption technique, a spectrometer called “Lucrecia” has been installed at the ISOLDE mass separator at CERN. It consists of a large NaI(Tl) crystal of cylindrical shape ($L=\varnothing=38$ cm) with a cylindrical hole ($\varnothing=7.5$ cm) at right angles to the symmetry axis. The purpose of the hole is twofold: on the one hand it allows the beam pipe (coming from the separator) to enter up to the centre of the crystal, thus allowing on-line activity of very short half-life (>5 ms) to be deposited at the centre and measured. On the other hand it allows us to place ancillary detectors inside for the detection of the positrons (β^+ -decay), electrons (β^- -decay) or X-rays (EC process) produced in the decay. In our case we use a plastic scintillator to detect the positrons and a Germanium telescope (planar+coaxial) to detect X-rays and γ -rays. Surrounding the whole setup there is a shielding box 19 cm thick made of four layers: polyethylene-lead-copper-aluminium. This shield stops a large part of the room background (mainly neutrons and γ -rays), thus reducing the counting rate in the main crystal by a factor of 6 when the proton beam is bombarding the target. In Fig. 5.3 a schematic view of the detector setup placed inside the shielding box is shown, and Fig. 5.4 is a photograph of the real set up where we see, not only the NaI(Tl) cylinder and some of the PM tubes, but also the telescopic beam pipe which can enter up to the centre of the crystal.

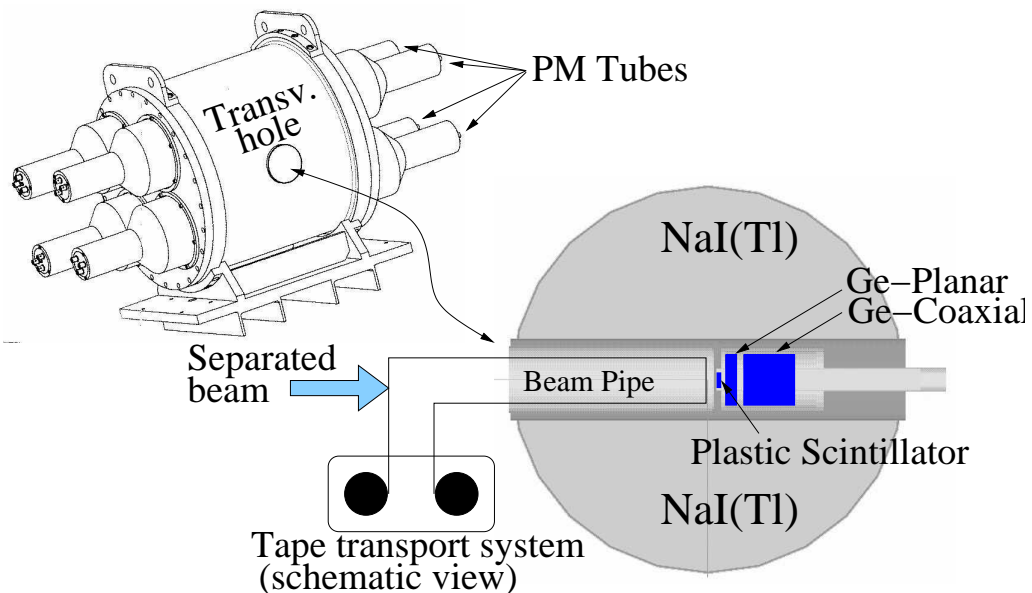


Figure 5.3: Detector setup for the ^{76}Sr measurement. In the upper-left part we have a 3D plot of the cylindrical NaI(Tl) detector “Lucrecia”, and in the lower part we see a transverse cut through the main crystal and the ancillary detectors, as well as the tape where the separated ^{76}Sr beam is implanted.

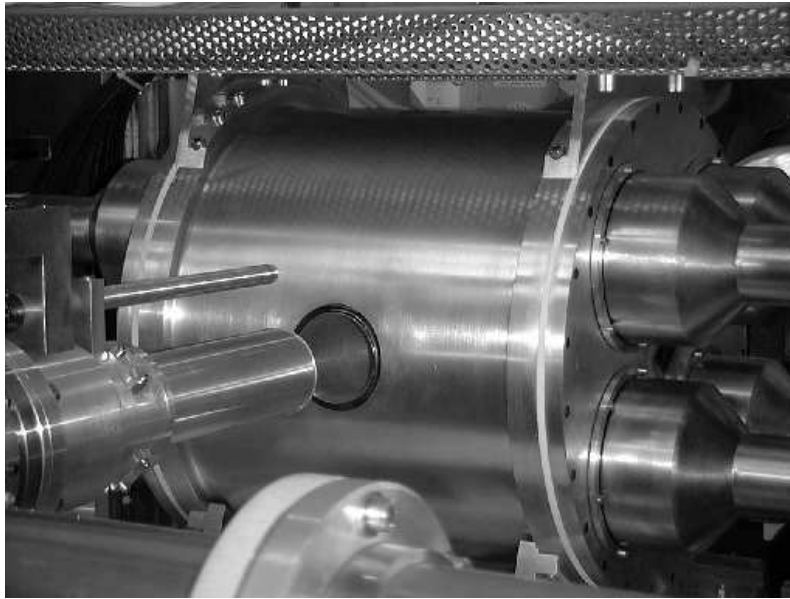


Figure 5.4: Lucrecia, the biggest NaI(Tl) crystal ever made. At the left side of the picture there is the telescopic beam pipe.

The energy resolution of the crystal is $\approx 7\%$ at 662 keV, and the total and peak efficiencies calculated with the *GEANT4* code [24] are shown in Fig. 5.5. The important thing about this graph is that the total efficiency is $\gtrsim 90\%$ in the range 300-3000 keV so that for every cascade of two or more γ -rays in this range, the probability of detecting something is always $\gtrsim 99\%$.

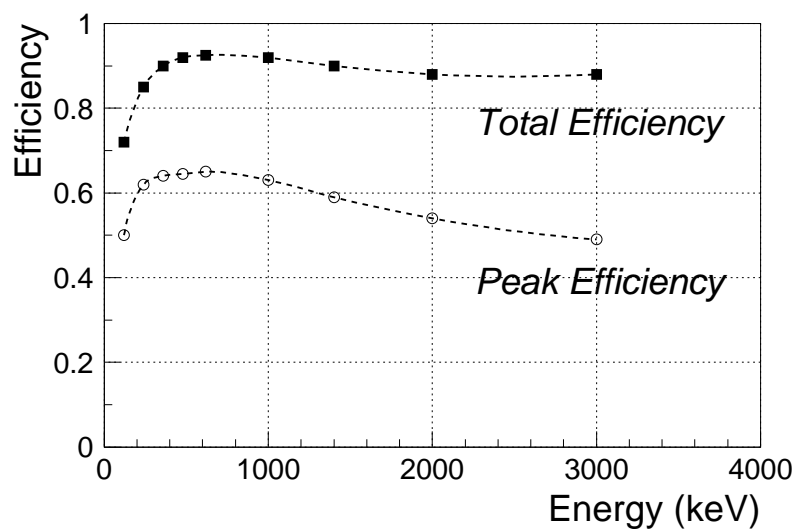


Figure 5.5: Lucrecia's total and photo-peak efficiency.

5.3 The measurement

The experiment on the β -decay of ^{76}Sr took place in the summer of 2001. The 28th of August a 52 g/cm^2 Nb target with W hot surface ion source was already mounted at the HRS separator and, after some technical problems¹, on the 31st at around 18:00 h the first $^{76}\text{Sr}^{19}\text{F}^+$ radioactive beam was separated and steered up to the detection set-up. The CF_4 gas flow rate to achieve the fluorination of Sr and therefore its selective separation was 2×10^{-5} mbar·l/s. The beam transmission from the HRS separator front-end to the Lucrecia spectrometer was $\approx 78\%$. The measurement started with 6 proton pulses per PSB super-cycle (see Fig. 5.1) but it was soon changed to 9 protons per super-cycle. The beam gate was open for 15 seconds during which the reaction products were extracted continuously, separated, and implanted on an aluminised Mylar tape. The tape moved in a symmetric cycle of 15 s of implantation and 15 s of measurement. Under these conditions (beam intensity, beam gate and tape cycle) the NaI(Tl) crystal registered ≈ 4500 counts per second of which ≈ 1500 were background.

The singles spectra (without any condition) from this measurement are shown in Fig. 5.6. The upper panel shows the spectrum measured with Lucrecia. It has a very complex structure which includes peaks coming from the decay of ^{76}Sr and the decay of its daughter ^{76}Rb , the background contribution, and a wide continuum toward the end made of background plus pile-up. The beta spectrum represents the energy lost by the positrons in the plastic scintillator. It has a very simple structure: a noise peak well separated from the continuous beta spectrum. Finally, the X-ray spectrum is shown in the lower part of the figure. We see clearly the Rb X-rays corresponding, in principle, to Electron Capture in ^{76}Sr . The K_α line is at 13.4 keV and the K_β at 15 keV. Surprisingly, we do not see the Kr X-rays which should follow the EC in ^{76}Rb . This will be explained later in Sec. 6.1.

The measurement of the decay of ^{76}Sr under the conditions listed above lasted for roughly two days. During these two days 13 hours of ^{76}Sr activity were properly measured, the rest of the time was devoted to background and calibration measurements with standard sources. Normally these measurements took place when there were problems (accelerator, separator, tape transport system, vacuum...), which did not allow us to measure the decay of interest. After these two days the conditions were changed to optimise the measurement of the daughter activity (^{76}Rb decay). The HRS magnet was set to separate mass 76 instead of 19+76. As ^{76}Rb is produced in the reaction some orders-of-magnitude more than ^{76}Sr , separating mass 76, and therefore ignoring the fluorination, we measure mainly the decay of ^{76}Rb , with the contribution from ^{76}Sr being perfectly negligible. On the other hand the

¹On the 29th of August in the evening, lightning struck on building 250 which holds part of the power supply for the accelerators and experimental areas at CERN: A 18 KV cell exploded and power was completely lost at ISOLDE and at the PS-Booster!!

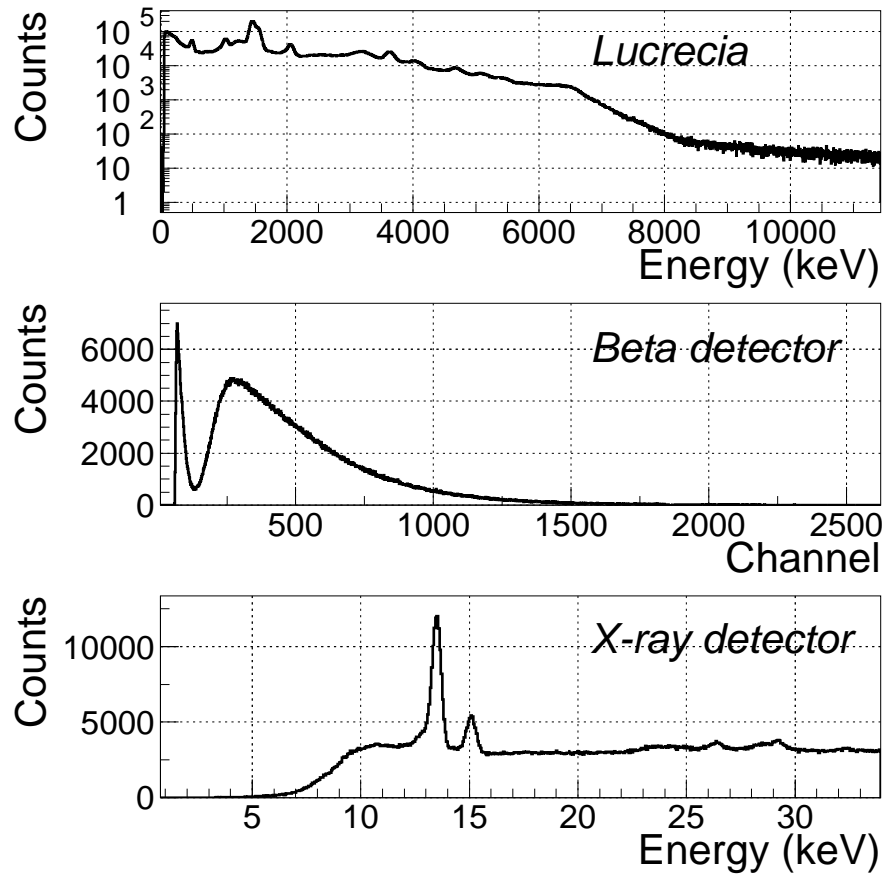


Figure 5.6: Direct spectra registered in Lucrecia and the ancillary detectors during the measurement of the ^{76}Sr β^+ -decay.

beam gate was changed to only 6 ms and the number of proton pulses per super-cycle reduced to 2. Even with these conditions the counting rate at the beginning of the 15 s symmetric cycle was too high and a 3 s delay was set between the transportation of the source to the centre of the crystal and the start of the acquisition system. Therefore the cycle was not symmetric anymore as we had 15 seconds of implantation, transport of the source, 3 s of delay and 12 s of measurement. In these conditions the daughter activity was properly measured allowing us to subtract it from the decay of interest as we will see in the next chapter.

Chapter 6

Data analysis of the ^{76}Sr β -decay

6.1 Sorting the data

The first stage during the analysis process is the sorting of the data. This means that we have to pass through all the data, event by event, making projections of the parameters of interest. In other words, we construct the spectra that we need for our analysis. These spectra can be with or without conditions imposed in the ancillary detectors. For example, in Fig. 6.1 we have the energy spectra registered in the beta detector (plastic scintillator) and in the X-ray detector (Ge planar) during the

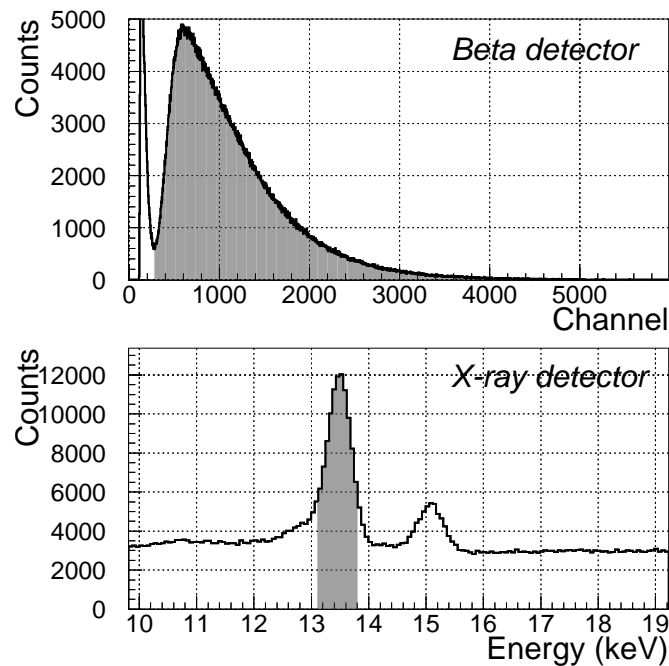


Figure 6.1: Energy spectra measured with the ancillary detectors.

measurement of the ^{76}Sr decay. The grey shades indicate the gates which define the conditions imposed in the ancillary detectors to accumulate some particular spectra in the NaI(Tl) crystal Lucrecia. To make this clear we look at Fig. 6.2. There we have different energy spectra registered in Lucrecia. The upper spectrum is the energy deposited in Lucrecia when there is no condition imposed on the ancillary detectors. The middle spectrum of Fig. 6.2 is again the energy deposited in Lucrecia but this time requiring that the beta detector registers something within the gate represented by the grey region in the upper part of Fig 6.1. Finally, the lower panel of Fig. 6.2 shows the energy in Lucrecia when the X-ray detector measures something within the gate represented by the shaded region of the lower spectrum of Fig 6.1.

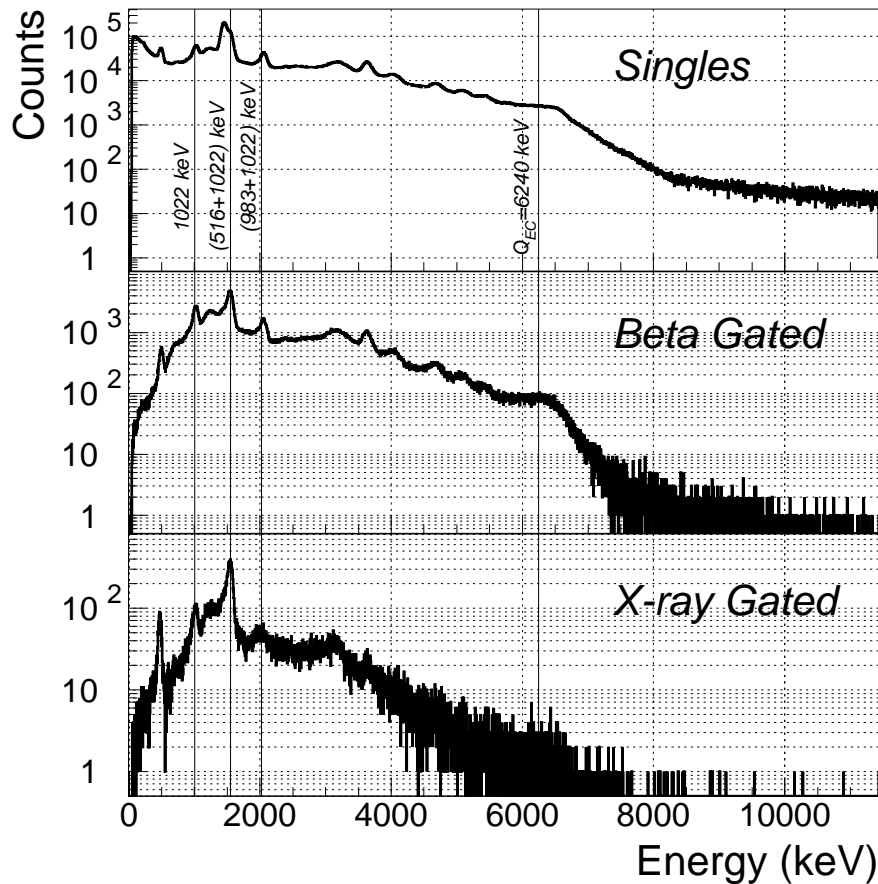


Figure 6.2: Energy spectrum measured in Lucrecia without conditions (upper panel), requiring coincidence with the beta detector (middle panel) and requiring coincidence with the Rb K_{α} peak in the X-ray detector (lower panel).

In principle, the two gated spectra of Fig. 6.2 should correspond to the β^+ and the EC components of the decay. The peaks in the β -gated spectrum should be shifted by 1022 keV with respect to the same peaks in the X-ray gated spectrum. However we observe something different. In Fig. 6.2 we have marked the most prominent peaks of the decay of ^{76}Sr and they appear in the same position for the three spectra. The reason is that even though we have set a gate on the appropriate X-ray peak to determine the EC component of the decay, this peak does not always correspond to the electron capture in ^{76}Sr . Most of the counts in this peak come from the internal conversion of the 39 keV gamma ray after the β^+ -decay of ^{76}Sr . In other words: we can not have a clean EC spectrum for this decay. Therefore we must analyse either the β^+ component of the decay (we lose 1022 keV of energy window) or the total decay $\beta^+ + EC$ using the direct spectrum without conditions. We decided to analyse the total decay because the last MeV of the spectrum can be crucial in terms of distinguishing between the oblate and prolate shape for ^{76}Sr . The main drawback to analysing the total decay is that we need to take into account the background and the daughter activity accurately. The next section explains how this was done.

6.2 Determination of the contaminants

There are three different contaminants which distort the spectrum we want to analyse: the pile-up, the room background and the daughter activity (^{76}Rb β -decay). The pile-up can be calculated following Ref. [28] as was explained in Sec. 3.2. However, the room background and the daughter activity must be measured under the same experimental conditions as the decay of interest.

The room background during the experiment gave a counting rate of ≈ 1.5 kHz in Lucrecia. In these conditions it does not produce any pile-up. Therefore, a direct measurement of the background is appropriate for use in the subtractions. However, a direct measurement of the daughter, namely the β -decay of ^{76}Rb , is not clean because it contains background and furthermore it produces first order pile-up (counting rate ≈ 5 kHz). In Fig. 6.3 we see how the ^{76}Rb decay spectrum was cleaned to be used afterwards as a contaminant in the main decay of interest. In the upper panel the black solid line is the direct spectrum corresponding to the β -decay of ^{76}Rb . The green dashed line is the room background and the blue dashed line is the calculated pile-up. Finally, the red line is the sum of the two dashed spectra, in other words the total contaminating spectrum. The lower panel shows the result of the subtraction, the direct spectrum minus the total of the contaminants. The normalisation factor for the background has been calculated using the energy region 12-13.7 MeV, which lies beyond the end point of the pile-up but below the peak of the light pulser. After removing the background, the normalisation factor for the pile-up can be calculated using the region 9.7-11.6 MeV, beyond the Q_{EC} value.

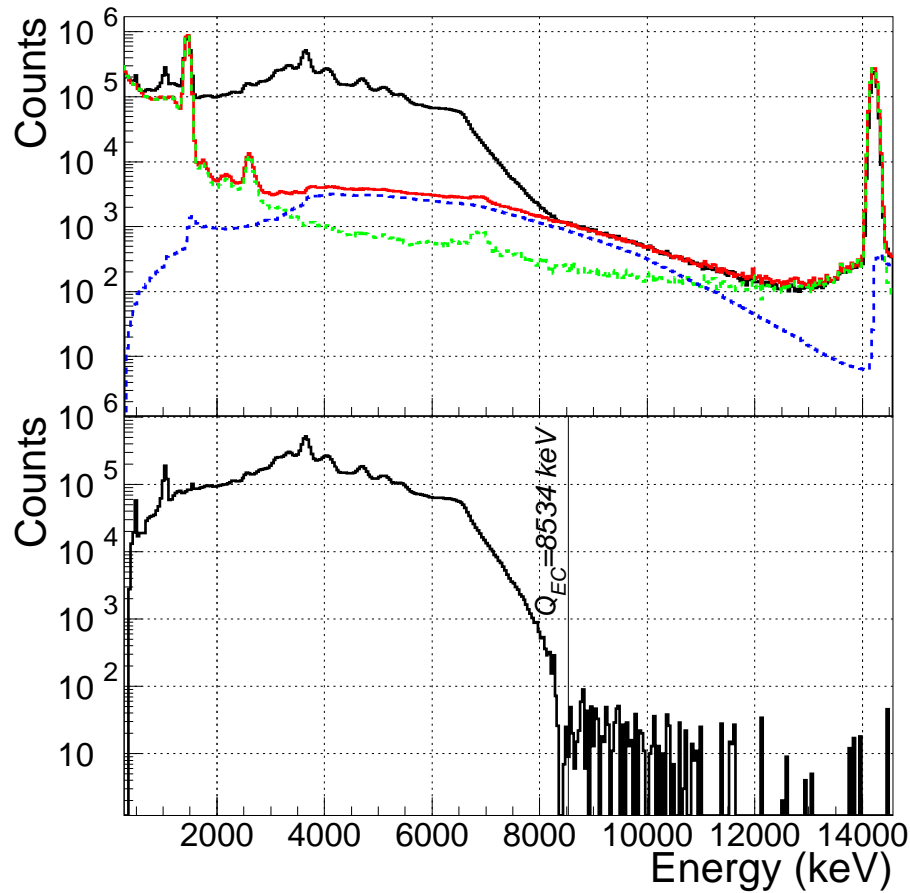


Figure 6.3: ^{76}Rb decay spectrum and its contaminants (see text).

Once we have a clean ^{76}Rb decay spectrum we can proceed to clean the ^{76}Sr decay spectrum which is the one we want to analyse. In this sense talking about subtractions is not completely correct. In Sec. 3.2 a method to avoid subtractions was presented and it will be used for the present analysis. Therefore, in what follows we calculate the normalisation constants for the contaminants in order to clean the spectrum of interest, but we do not subtract any spectrum for the analysis (we perform the subtraction explicitly only to show it in the figure). The upper panel of Fig. 6.4 shows in black solid line the direct spectrum corresponding to the β -decay of ^{76}Sr . The dashed lines are the contaminants: background (green), pile-up (blue) and daughter activity cleaned before (pink). The red solid line is the sum of the three contaminants. In the lower panel of Fig. 6.4 we have the clean ^{76}Sr decay spectrum. In this case the regions chosen to calculate the normalisation factors are: 12-13.7 MeV for the background, 8.9-10.4 MeV for the pile-up and 6.9-8.1 MeV for the ^{76}Rb activity. Again it is important to keep in mind that the spectrum to be analysed is in reality the direct spectrum with all of its contaminants, without performing any

subtraction. Knowing the different contaminants and their normalisation factors the analysis algorithm described in Sec. 3.2 will take them into account.

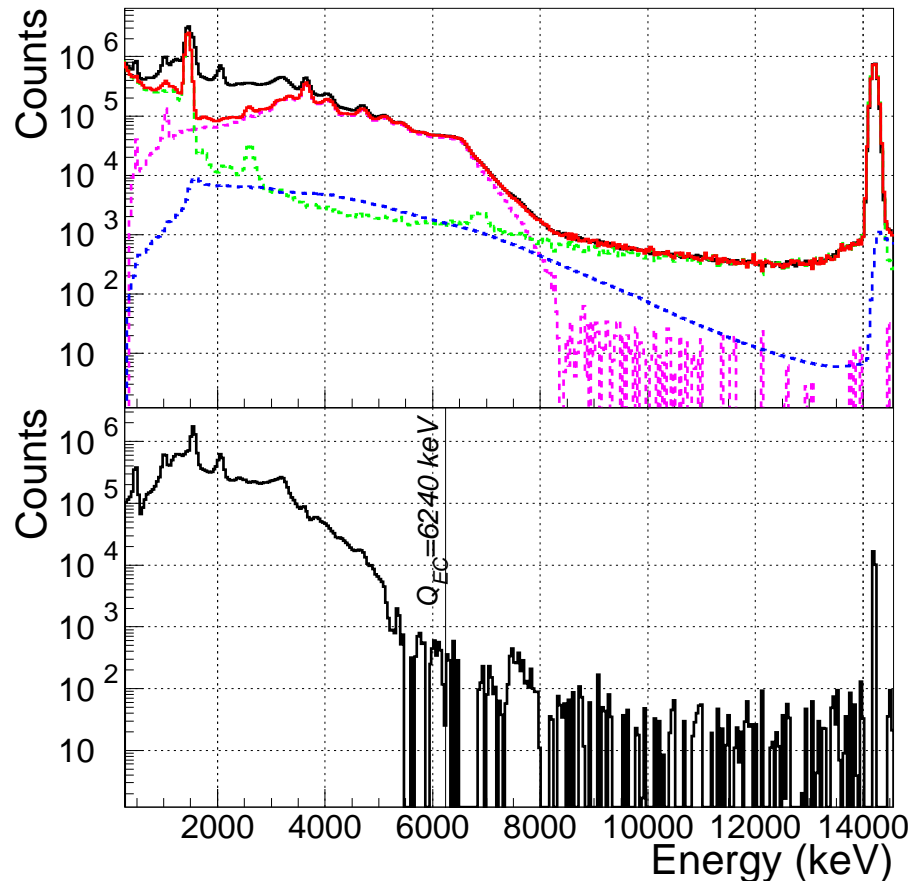


Figure 6.4: ^{76}Sr decay spectrum and its contaminants (see text).

6.3 The EM algorithm applied to the data

Now that we have measured properly the decay of interest and identified the contaminants, there is only one more thing that we need for the analysis: we need to calculate the response function of the detector to our decay. This is done in two steps: First we use Monte Carlo simulations to calculate the response function of our detector to individual mono-energetic gamma rays and to positrons with energy following a Fermi distribution for different end points. In a second step we use the known level scheme of the daughter nucleus to construct the response function to our particular decay by convoluting the responses to individual gamma rays and to

positrons calculated previously [23].

All the Monte Carlo simulations were performed using the *GEANT4* code [24]. To make sure that the description of the geometry of the detector, the materials and the physical processes are properly implemented in the simulation, one must compare the results from the simulation with a well known radioactive source. We chose the β -decay of ^{24}Na because it has a relatively large Q_β window and the disintegration scheme is mainly a two gamma cascade. The ^{24}Na was implanted on the tape in the same position as the ^{76}Sr samples during the experiment. The result of the simulation can be seen overlaid to the real measured source in Fig. 6.5. Once we get such a good agreement we can trust our calculated response function and we can use it for the particular decay that we want to analyse.

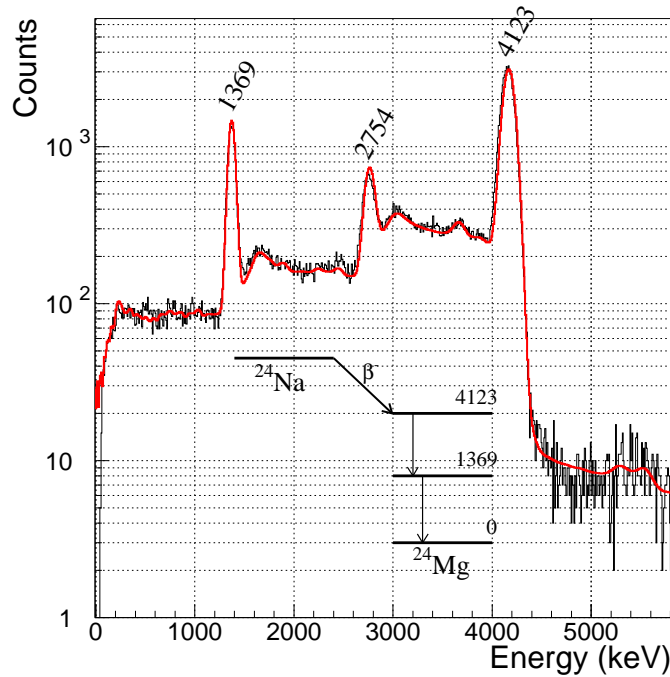


Figure 6.5: Simulation of the β -decay of ^{24}Na (red) overlaid to the measured ^{24}Na source (black).

As mentioned earlier, we can use the simulated response functions for individual γ -rays and the daughter level scheme to calculate the response function of our detector to our decay of interest [23]. The problem is that the level scheme of the daughter is not very well known. Up to ≈ 2 MeV we can use Ref. [49], but our Q_{EC} window allows the decay up to ≈ 6 MeV in the daughter. Therefore, the upper part of the level scheme of ^{76}Rb must be estimated using a statistical model. The level density from 2 MeV on has been calculated using the back-shifted Fermi gas model [50] with

a level density parameter $a = 11 \text{ MeV}^{-1}$ taken from [51], and a fictitious ground-state $\Delta = -1.324 \text{ MeV}$ calculated following [50]. For the branching ratios we follow the Axel-Brink hypothesis: the electromagnetic strength can be derived from the parametrisation which best fits the experimental data (photo-absorption) on giant resonances. We have taken into account E1, M1 and E2 transitions, using the parametrisation of Ref. [52][53][54, 55] respectively.

At this stage we can run the Expectation Maximisation algorithm modified to take into account the contaminants (Sec. 3.2). The input spectra we must use are: the direct spectrum measured for the decay of ^{76}Sr (Fig. 6.4 upper panel, solid black line), and the individual contaminants (Fig. 6.4 upper panel, dashed lines). After the deconvolution process we will obtain as output the β -intensity distribution $I_\beta(E)$ in the decay of ^{76}Sr , and the reconstructed spectrum which is simply the product of the response matrix times the β -intensity distribution plus the contaminants, and this should reproduce the measured spectrum.

For our analysis an energy bin of 40 keV was set, and after 300 iterations we obtained a β -intensity distribution which reproduces quite accurately the experimental data. Fig. 6.6 shows these results. At the top of the figure the shaded region (without line) represents the measured spectrum used for the analysis. At the bottom we have the $I_\beta(E)$ distribution obtained from the analysis. This graph has been split in two different ranges in order to see the structure of the $I_\beta(E)$ near the Q_{EC} value. Finally, if we multiply the response function of the detector by this $I_\beta(E)$ distribution and then we add the contaminants we have the recalculated spectrum represented by the dashed line in the upper panel. We can see that it reproduces very well the experimental spectrum. The fact that we reproduce the experimental data (Fig. 6.6 top) plus the fact that our simulations are good (Fig 6.5) implies that we can trust the result we have obtained for the $I_\beta(E)$ distribution (Fig. 6.6 bottom).

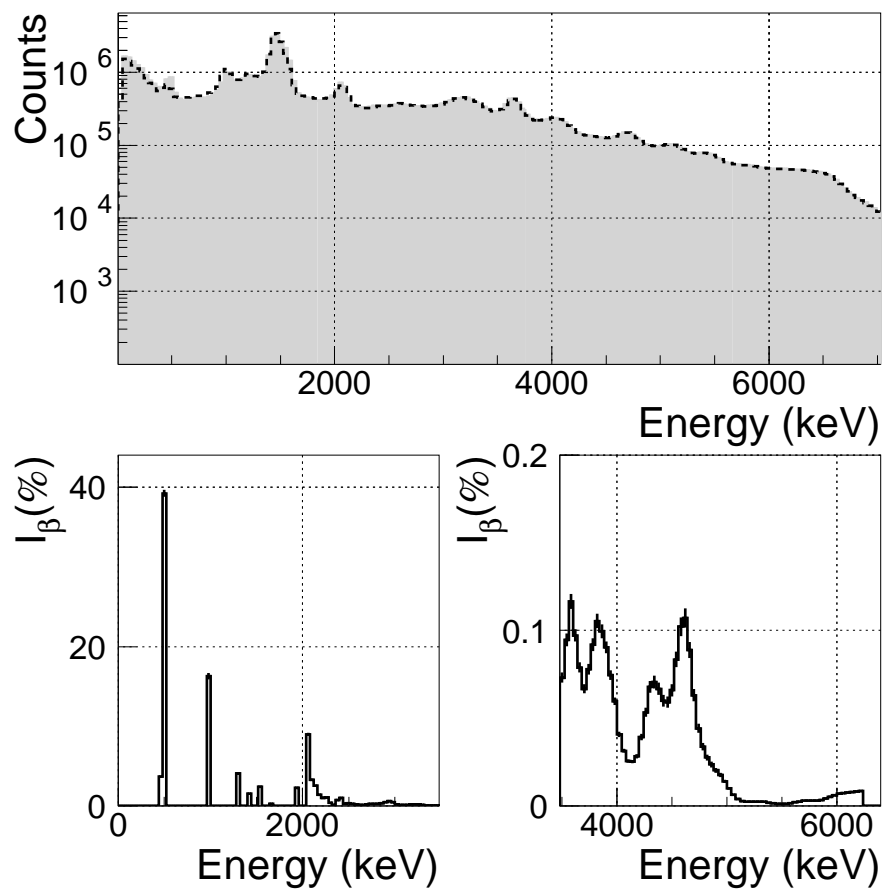


Figure 6.6: Top: Experimental spectrum for the ^{76}Sr decay (grey shade). Overlaid there is the recalculated spectrum using the result after the analysis (dashed line). Bottom: Resulting $I_\beta(E)$ after the data deconvolution.

Chapter 7

Results and discussion

7.1 The B(GT) distribution in the β -decay of ^{76}Sr

With the results obtained in the previous chapter it is easy to obtain the strength distribution B(GT) of our decay of interest. To do so, one needs to know the half-life of the parent nucleus, and the statistical rate Fermi integral. The former is known to be $T_{1/2}=8.9(7)$ s [49], and the latter is calculated using numerical methods and can be found tabulated in Ref. [56]. The Fermi integral depends on the energy available for the decay, therefore, the other important quantity we need is the $Q_{EC}=6240(40)$ keV taken from Ref. [57]. Fig. 7.1 shows the resulting B(GT) distribution. The shaded area represents the uncertainty, which grows rapidly as we approach the Q_{EC} value. Since we used a 40 keV energy bin for the analysis described in the previous chapter, now the resulting B(GT) is shown again with such an energy bin, but in order to have the B(GT) in the natural units $g_A^2/4\pi$, as if it was calculated

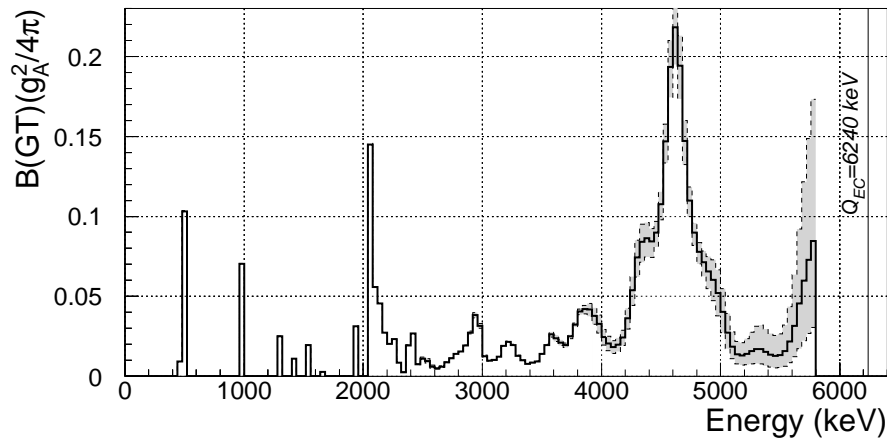


Figure 7.1: B(GT) distribution in the β^+ -decay of ^{76}Sr as a function of the excitation energy in the daughter nucleus ^{76}Rb .

for a continuum of energies, the original result in $\frac{g_A^2}{4\pi \times 40 \text{ keV}}$ has been multiplied by 40 keV. In this way if we want to integrate the $B(GT)$ between two energy limits we only need to sum up the contents of all the channels within this particular energy range.

The total $B(GT)$ summed up to 5.6 MeV gives an amount of:

$$\boxed{\sum^{5.6 \text{ MeV}} B(GT) = 3.8(6) \frac{g_A^2}{4\pi}}$$

of which almost 60% is located in the resonance between 4 and 5 MeV. The uncertainty value of $0.6 \frac{g_A^2}{4\pi}$, as well as the uncertainty region in Fig. 7.1, have been estimated following two different approaches: First we used a pure statistical approach and propagated the statistical uncertainties from the original spectra to the final $B(GT)$ distribution using the covariance matrices. Unfortunately, due to the high correlation between the $I_\beta(E)$ of different channels, the propagated error is very small and therefore not realistic. Then we decided to study the variations of the $B(GT)$ as a function of different parameters which play an important role in our analysis such as the Q_{EC} value, $T_{1/2}$, normalisation factors of the contaminants, parameters of the back-shifted Fermi gas model, number of iterations... After all these different checks we concluded that the $B(GT)$ distribution as well as the integrated $B(GT)$ are particularly sensitive to the normalisation factor that multiplies the daughter activity as the main contaminant. Choosing two extreme values for this factor we could estimate the uncertainty that we show in Fig. 7.1 and in the result for the integrated $B(GT)$.

Now that we have a final result for the I_β and $B(GT)$ distributions we can compare them with the results obtained with a high resolution set-up in Ref. [49]. Such a comparison is presented in Fig. 7.2. Looking at the upper graph we conclude that, in terms of β -intensity the difference between both results is not very significant. We see roughly the same levels populated and the main β -feeding accumulated at 516 keV, 983 keV, 1289 keV, and the region around 2 MeV. However, when we look at the lower panel of Fig. 7.2 the differences between the two results are more obvious. The *pandemonium effect* presented in Sec. 2.2.1 shifts the strength to lower energies in the high resolution experiment, but, on top of that, due to the fragmentation of the $B(GT)$ in the high level density region beyond 3 MeV, and the low efficiency of the Ge detectors for high energy γ -rays, there is no information from the high resolution experiment [49] above 2.8 MeV. On the contrary, the TAS results of this work show that most of the strength is located beyond 3 MeV. If we sum up the $B(GT)$ to all the levels populated in [49] we arrive to a total $B(GT)$ of $0.52 \frac{g_A^2}{4\pi}$ to be compared with our result of $3.8(6) \frac{g_A^2}{4\pi}$ reported before. This situation reminds us very much of the one shown in Fig. 2.1 when talking about the *apparent $B(GT)$* that one measures with Ge detectors. Obviously, if one wants to arrive at final conclusions about the shape of the nucleus by comparing the experimental $B(GT)$

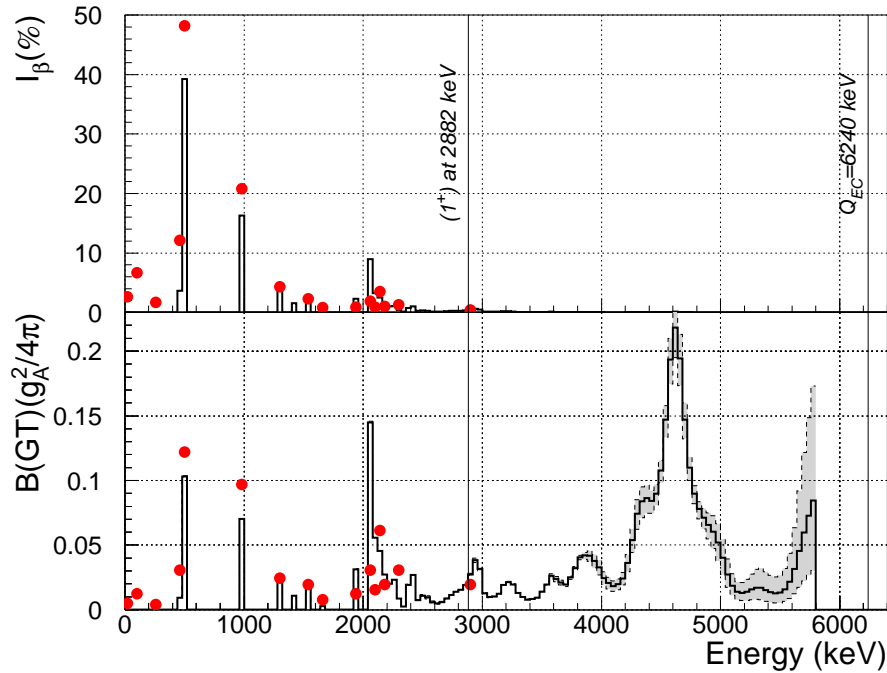


Figure 7.2: Comparison between the results of this work (solid line) and those from Ref. [49] using a high resolution setup (red dots). The first vertical line indicates the position of the last level seen in [49].

with the theoretical calculations, the TAS technique must be used to measure the β -decay of interest.

7.2 Conclusion: The shape of the N=Z nucleus ^{76}Sr from its β -decay

At this stage we have an experimental B(GT) distribution which can be trusted up to 5.6 Mev (beyond this point the error bars are too large), the following step is to compare this result with the theoretical calculations presented before in Sec. 4.3 and see whether we can extract any conclusion about the shape of the N=Z nucleus ^{76}Sr in its ground-state.

Taking into account that the position of the levels in the theoretical calculations very seldom agree exactly with the experimental levels, one can never compare the B(GT) level by level. There are two possible methods to compare our results with theory. The first method is to compare the B(GT) distribution accumulated in wide energy bins. In Fig. 7.3 we have represented the B(GT) distribution accumulated in 800 keV bins. The B(GT) value has been divided by 800 to have units of keV^{-1} in such a way that the area of the graph is the integral of the B(GT). Our results fit

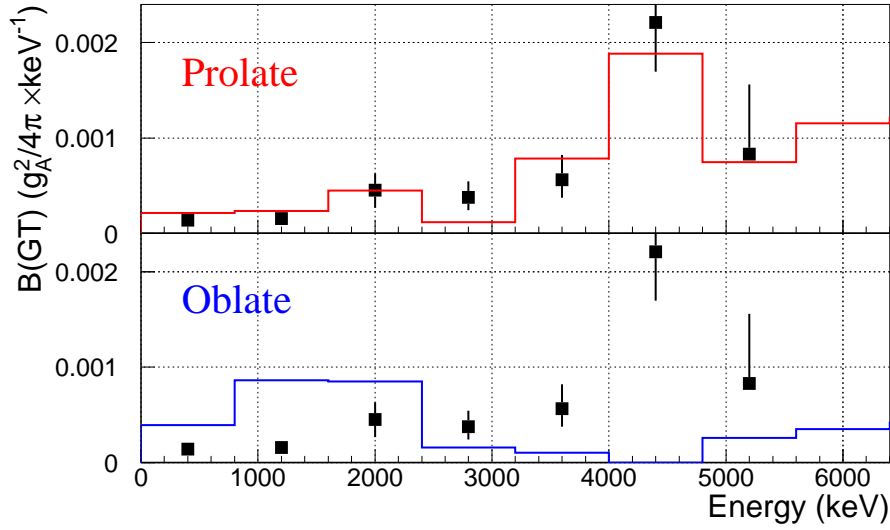


Figure 7.3: $B(\text{GT})$ distribution resulting from this work (squares) compared with the theoretical calculations [35, 36] for prolate (top, red) and oblate (bottom, blue) shapes of ^{76}Sr .

quite well the theoretical calculations of Ref. [35, 36] only in the upper panel, which is the prolate case. The resonance between 4 and 5 MeV that we have found in our experiment is only compatible with the QRPA calculations for a prolate ground-state for ^{76}Sr . In the region between 0 and 4 MeV the agreement between experiment and theory is also markedly better for the prolate shape case.

The second method to compare our result with theory is representing not the $B(\text{GT})$ but the integrated $B(\text{GT})$, i.e., for each energy we plot the accumulated $B(\text{GT})$ from the ground-state of the daughter nucleus up to that particular energy. This is shown in Fig. 7.4. From the comparison presented in this figure there is no possible doubt that our result fits very well the calculations of Ref. [35, 36] for a prolate ground-state shape for ^{76}Sr , and is absolutely incompatible with the oblate case.

Summarising, from our work we conclude the following:

1. We have measured the β -decay of ^{76}Sr using the Total Absorption Spectroscopy technique. From the analysis of the data we have obtained three important results: The β -intensity distribution $I_\beta(E)$ of Fig. 6.6, the Gamow-Teller strength distribution $B(\text{GT})$ of Fig. 7.1, and a value for the total $B(\text{GT})$ up to 5.6 MeV of $3.8(6) g^2/4\pi$. These results are very important in themselves as nuclear structure data and for use in network calculations fundamental for the understanding of the astrophysical rp-process.
2. From the comparison of our results with the theoretical calculations of

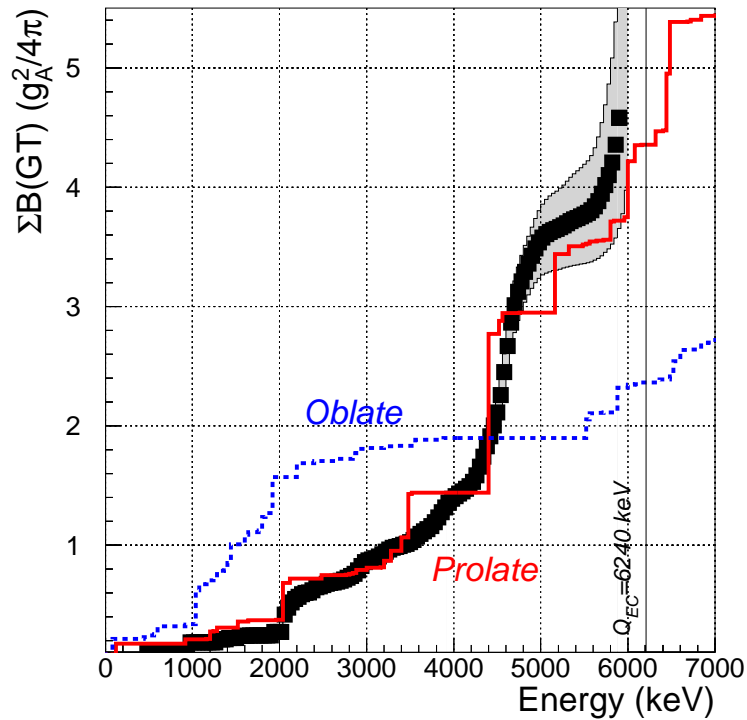


Figure 7.4: Accumulated B(GT) from this work (squares) compared with the theoretical calculations [35, 36] for prolate (red) and oblate (blue) shapes of ^{76}Sr .

Ref. [35, 36] we conclude for the first time that the ground-state of ^{76}Sr is strongly prolate ($\beta_2 \approx 0.4$), in agreement with theoretical predictions [39, 40] and with previous experimental indications [31]. There was earlier experimental evidence for the strong deformation of this nucleus [31] but not of its prolate character.

3. An important consequence of the present work is the validation of the method of deducing the deformation of ground-states or β -decay isomers, including the sign of the quadrupole moment, from the comparison of the β -decay TAS results and the calculated B(GT) since the ^{76}Sr ground-state is a very clean case, free of shape admixtures. This opens new opportunities in the study of nuclei far from the stability line where very often the first information comes from β -decay (half-life, $J^\pi \dots$).
4. Once the method is validated, one can trust other results involving more complex systems such as nuclei where the ground-state is a mixture of two different shapes. This shape mixing effect occurs for instance in ^{74}Kr [58]. We have measured the β -decay of this nucleus with Lucrecia at ISOLDE and our results support the mixing of prolate and oblate shapes in the ground-state [59].

This work has been published in *Physical Review Letters* [60].

Part III

The Gamow-Teller resonance in the Rare-Earth region

Chapter 8

The Rare-earth nuclei above ^{146}Gd

8.1 The quasi-doubly magic ^{146}Gd

As already explained at the end of Sec. 1.4 β -decay is a forbidden process in general. The reason is that the final states which can be reached in the decay without violation of the selection rules lie, in general, beyond the Q_{EC} value, and therefore they are not accessible to the β -decay process. There are, however, some exceptions. One of them, the $N \approx Z$ region around mass 70-80, was already studied in the second part of this work. The other exceptions are the nuclei around ^{100}Sn , in which protons from the intruder orbital $g_{9/2}$ can decay to the $g_{7/2}$ which is free on the neutron side, and the rare-earth nuclei above ^{146}Gd , in which the intruder $h_{11/2}$ is being filled with protons that can decay to the empty $h_{9/2}$ neutron orbital. This latter case is the object of study in this third part of the work.

^{146}Gd has a very special feature only shared by the doubly magic ^{208}Pb : it is an even-even nucleus but its first excited state has spin-parity $J^\pi=3^-$ instead of 2^+ like most of the other even-even nuclei [61, 62]. On the other hand, the transition probability ($B(E3)$) from this state to the ground-state is very large (a factor of ≈ 37) compared with the single-particle estimate [62]. The same effect occurs in ^{208}Pb , and it is a clear indication of the high collectivity of the 3^- state. These similarities between both nuclei made people think about the possibility of ^{146}Gd as another doubly magic nucleus. Recent experiments have been performed in search of a second octupole in this nucleus [63].

According to the shell model, there are 5 orbitals between the magic numbers 50 and 82: $1g_{7/2}$, $2d_{5/2}$, $2d_{3/2}$, $3s_{1/2}$ and $1h_{11/2}$ (see Fig. 1.3). ^{146}Gd has 64 protons and 82 neutrons. Obviously, it is magic in neutrons, but on the proton side the orbitals $1g_{7/2}$ and $2d_{5/2}$ are full whereas the others are empty, and this does not close a shell. However, subtracting the separation energy for protons in ^{146}Gd and ^{147}Tb , and correcting for pairing correlations, one obtains an energy gap of ≈ 2.4 MeV between the last full orbital, $2d_{5/2}$, and the group of three free orbitals $2d_{3/2}$, $3s_{1/2}$ and $1h_{11/2}$

(which lie within ≈ 260 keV) [64]. This gap is not as big as the one obtained for the magic number 82, but still large enough to confer ^{146}Gd the properties of a quasi-doubly magic nucleus. This allows us to interpret all the nuclei in this region and their excited states as simple excitations of valence particles (quasi-particles on the proton side) above the ^{146}Gd core.

8.2 The nuclei around ^{146}Gd . The fast GT decay $\pi h_{11/2} \rightarrow \nu h_{9/2}$

If we can treat all nuclei in this region as excitations above the core defined by ^{146}Gd , we can imagine that, as soon as we add protons to the core (^{147}Tb , $^{148}\text{Dy}\dots$) we will fill the upper orbitals $d_{3/2}$, $s_{1/2}$ and $h_{11/2}$, thus opening the possibility to observe the fast Gamow-Teller decay $\pi h_{11/2} \rightarrow \nu h_{9/2}$ ¹. In this third part of the work we will study the allowed transition $\pi h_{11/2} \rightarrow \nu h_{9/2}$ in the rare-earth nuclei and its behaviour with the number of protons in the $h_{11/2}$ orbital.

In principle one might think that the best cases to study this decay are the $N=82$ isotones. However, the odd- $N=82$ nuclei present two isomers that can not be separated experimentally in most of the cases, and with the even- $N=82$ we can only study the cases with an even number of protons in the $h_{11/2}$ orbital. One of the cases studied here is the decay of ^{148}Dy with 2 protons in the $h_{11/2}$ (see Sec. 11.1). With the $N=83$ cases there is no experimental problem because, even though the odd- $N=83$ isotopes have two isomers, one with spin-parity $J^\pi=2^-$ and the other $J^\pi=9^+$, they can be produced selectively by means of the fusion-evaporation reaction. We will see later that the low-spin isomer corresponds to a configuration with an even number of protons in the $h_{11/2}$ whereas the high-spin isomer will have one more proton in this orbital. In other words, measuring the odd- $N=83$ isotopes above ^{146}Gd (^{148}Tb , ^{150}Ho , ^{152}Tm) we can cover the systematics of the $\pi h_{11/2} \rightarrow \nu h_{9/2}$ decay in the region as we fill the $h_{11/2}$ orbital with 0 to 5 protons. In this work we will describe the measurement and analysis of the even- $N=82$ ^{148}Dy , and the odd- $N=83$ ^{148}Tb and ^{152}Tm . The other odd- $N=83$ nucleus which is part of the systematics is ^{150}Ho already measured by D. Cano *et al.* [25]. Apart from the systematics of the number of protons in the $h_{11/2}$ orbital, we will also present the decay of ^{156}Tm which has 5 protons and 4 neutrons above the ^{146}Gd core. This presents again the fast Gamow-Teller transition $\pi h_{11/2} \rightarrow \nu h_{9/2}$ but in this case we approach the deformed region.

In the three odd- $N=83$ cases the low-spin isomer (2^-) can be well described by the configuration $[\pi d_{3/2} \nu f_{7/2}]_2^- [\pi^{2n}]_{0^+}$, and the high-spin isomer as the configuration $[\pi h_{11/2} \nu f_{7/2}]_{9^+} [\pi^{2n}]_{0^+}$. In both cases, the second part coupled to 0^+ represents

¹Due to pairing correlations, as soon as we have two or more protons in these upper orbitals the proton pairs will be filling all the three orbitals at the same time.

n pairs of protons which, due to pairing correlations, partially occupy the three proton orbitals $d_{3/2}$, $s_{1/2}$ and $h_{11/2}$. Although this picture is only an approximation to reality, it can not be too wrong since in the framework of the proposed orbitals there is no other combination of one proton and one neutron producing either the 2^- or the 9^+ isomer. Therefore, the decay of the low-spin isomer can only happen by breaking a proton pair $[h_{11/2}^2]_{0^+}$, whereas the high-spin isomeric decay (9^+) will have two possible decays: one corresponding to the breakup of the proton pairs $[h_{11/2}^2]_{0^+}$ as in the former case, and the decay of the valence proton in the $h_{11/2}$ necessary to make the 9^+ . This extreme single-particle point of view is represented in Fig. 8.1. The proton pair of the figure represents in reality an undefined number of proton pairs which will be close to zero in the case of ^{148}Tb , one for ^{150}Ho and two in the case of ^{152}Tm . Due to pairing correlations there is always the possibility of pair scattering on the proton side, which means that proton pairs can be promoted from the ^{146}Gd core, thus crossing the 2.4 MeV gap. This is the only way to have non-zero occupation in the $h_{11/2}$ orbital in the case of $^{148}\text{Tb } 2^-$.

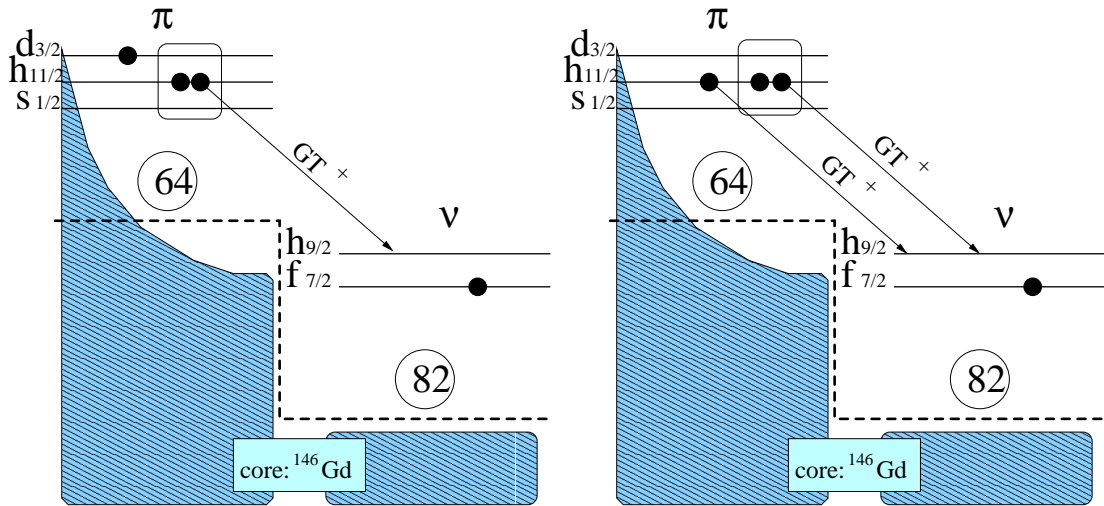


Figure 8.1: Extreme single-particle representation of the configuration of the two isomers in the odd- $N=83$ isotopes above ^{146}Gd . The low-spin isomer is on the left side and the high-spin isomer on the right one.

On the other hand, Fig. 8.2 shows schematically what we expect to see in the $B(\text{GT})$ distribution when we study the decay of the two isomers, stressing the component responsible for the decay. As we see in the figure, the decay of the odd proton in the high-spin case populates a very well defined state in the daughter nucleus, whereas the breakup of the proton pair in both the low- and high-spin cases populates a broad distribution which lies higher in energy. This is because the odd proton, in the 9^+ parent nucleus configuration, always decays populating an 8^+ two-particle state in the daughter at about 2-2.5 MeV. Here, two-particle ($2p$) or

four-particle (4p) states always refers to the number of valence particles, neglecting the proton pairs coupled to 0^+ . In the case of the decay of one proton of the pair coupled to 0^+ , there are many 4p states that can be populated in the daughter at higher energies: the energy of the 2p state, $\approx 2-2.5$ MeV, plus the extra energy necessary to break a proton pair $\approx 2-2.5$ MeV. This gives a bump of many 4p states centred at $\approx 4-5$ MeV, the main peak of the resonance. Without knowing the energy of the 8^+ 2p state one can estimate the energy of the 4p states as the energy needed to break a proton pair, plus the energy needed to break a neutron pair, plus the $\nu h_{9/2}$ single-particle energy in the daughter nucleus. This is again $\approx 4-5$ MeV. In the case of ^{148}Tb this bump should be shifted upward due to the energy needed to promote a proton pair from the ^{146}Gd core.

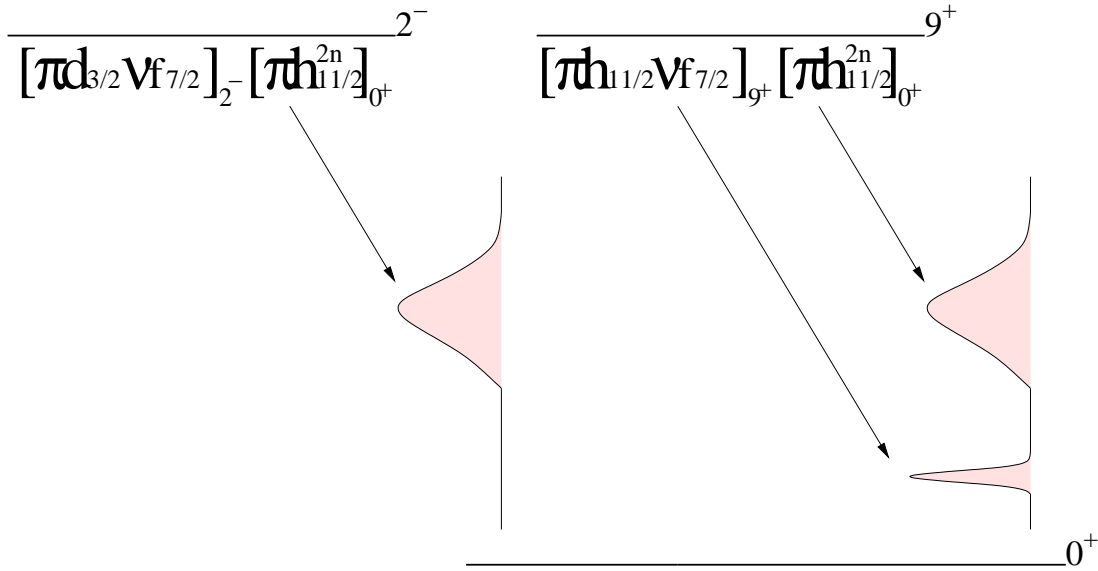


Figure 8.2: Qualitative description of our expectation for the decay of the low-spin isomer (left) and the high-spin isomer (right).

In this work we have studied the decay of the $Z=66$, $N=82$ ^{148}Dy , the decay of the two isomers 2^- and 9^+ of ^{148}Tb and ^{152}Tm , and finally the decay of ^{156}Tm . However here we will describe in detail only the experiment and analysis performed in the ^{152}Tm case. For the other cases the same accelerator facility, mass separator and TAS detector have been used, and the analysis techniques are very similar. In summary, in the following I will present a description of the experimental facilities at GSI, where the experiments were performed, a detailed description of the experiment and analysis of the decay of ^{152}Tm , and the results for all the different decays studied here. Finally we have performed shell model calculations to compare with our results on the systematics of the GT transition in the region.

Chapter 9

The experiment

9.1 The GSI accelerator facilities

The GSI (*Gesellschaft für Schwerionenforschung*), is a German laboratory fully dedicated to nuclear and applied physics using heavy ion accelerated beams. One of the most important research fields is cancer therapy using Carbon or Oxygen beams. In nuclear science one can study from nuclear structure to quark-gluon plasma (see also www.gsi.de/portrait/index_e.html). In our case we will focus on the nuclear structure of exotic nuclei.

The wide range of experimental possibilities at GSI is based on a multi-stage accelerator facility consisting of a linear accelerator, *UNILAC*, a synchrotron, *SIS*, and an experimental storage ring, *ESR*. For nuclear structure studies one can work at *UNILAC* energies. This accelerator was built in 1975. It can accelerate all nuclear species up to uranium. It consists of three stages:

1. A so-called *Wideröe structure* is the first stage. It consists of four electrode structures each containing 130 drift tubes. These operate at a radio-frequency of 27 MHz.
2. The *stripper* and the *Alvarez structures* form together the second phase. After many violent collisions with the molecules of a supersonic gas beam, the heavy ions are stripped of many electrons, up to 28 in the case of uranium. Then they enter into the second accelerating stage operating at 108 MHz.
3. Finally, the third stage is made of fifteen *single resonators*. It is in this phase where one can adjust the energy of the beam. At the end of this last structure, the heavy ions can have any energy in a range extending from 2 to 18 MeV per nucleon.

In Fig. 9.1 we see the single-resonator structures of the linear accelerator *UNILAC* (left side), and the general layout of GSI accelerators (right side). First there is the *UNILAC*, and at the end of this we see the first experimental hall for low energy

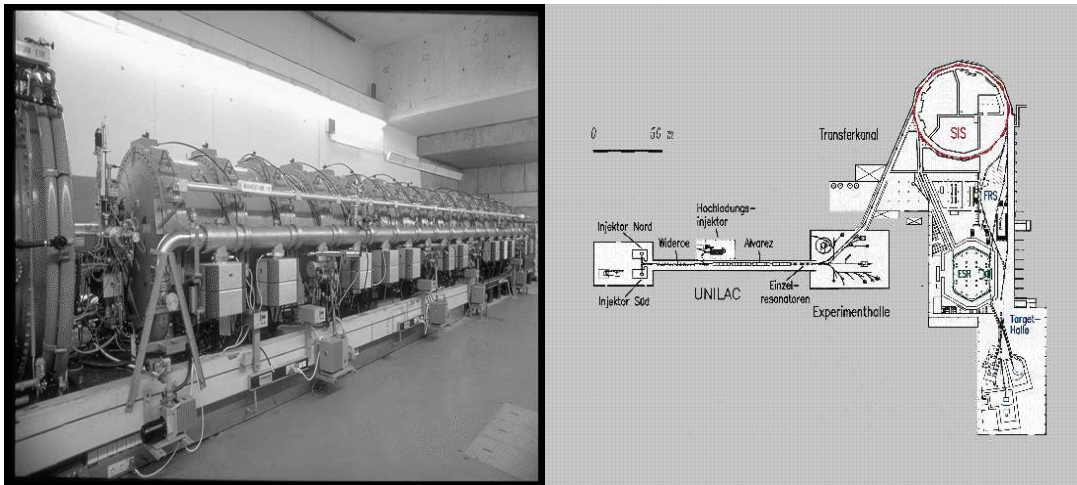


Figure 9.1: A view of the *UNILAC* and the layout of the GSI accelerator facilities.

physics. Apart from low energy studies, the *UNILAC* also acts as injector for the heavy ion synchrotron *SIS* and in the drawing we see the transfer line between the two accelerators. The *SIS* then sends the heavy ions at relativistic energies (up to 2 GeV per nucleon) to the fragment separator, to a second experimental hall, or to the experimental storage ring *ESR*.

9.2 ISOL, the On-Line Mass Separator

The On-line Mass Separator is situated in the low-energy experimental hall, at the end of the *UNILAC*. The heavy ion beam coming from the linear accelerator hits a target, producing different isotopes in fusion, fission, or multi-nucleon transfer reactions. Then, the mass separator acts as an instrument to select specific reaction products out of the bulk of products formed in such reactions. In Table 9.1 there is a summary of the main properties of the mass separator, and in Fig. 9.2 we see a schematic view of how it works.

The production and separation of the isotopes of interest happens in a series of steps:

1. The reaction products can either remain in the target, or fly out of the target, cross a very thin window (usually Ta or W of $0.8 - 3 \text{ mg/cm}^2$) and arrive at a catcher where they are stopped.
2. Now these products are inside the ion source where they are ionised to a 1^+ charge state. There are different types of ion source, for instance some of them are based on hot-cavity thermo-ionisers operating up to 2800 K, and some

High Voltage	55 kV, 1 Volt ripple, drift few volts per day
Beam Emittance	$< 10 \text{ Pi mm mrad}$ for FEBIAD sources
Energy Spread	$< 10 \text{ eV}$
Transmission	$\approx 90\%$ to focal plane chamber
Magnet	Radius=1500 mm, B=0.45 Tesla (max) Deflection angle 55°
Mass resolving power	500-1500 ($M/\Delta M$) depending on the ion source
Cross-contamination	$< 10^{-4}$ for neighbouring masses
Mass Range	up to mass 450 for 55 keV ions
Mass Accuracy; Positioning	0.01 amu; 0.1 mm

Table 9.1: Main characteristics of the on-line mass separator at GSI

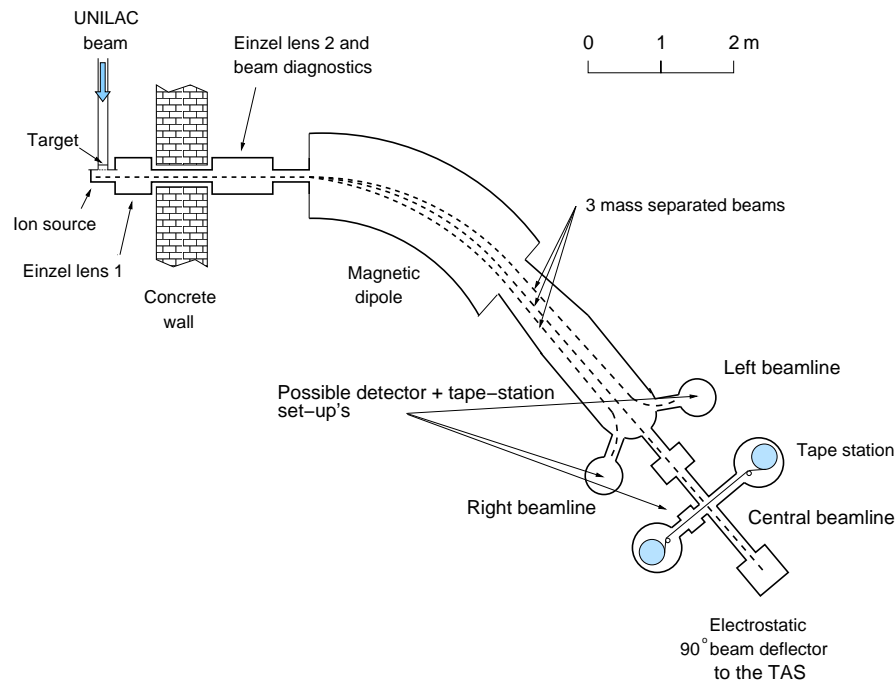


Figure 9.2: The on-line mass separator.

others using an electron beam to ionise the isotopes in the catcher. Sometimes it is possible to suppress the release of one specific isotope using its chemical properties¹. In these cases one can have not only mass but also Z selectivity.

3. After ionisation the reaction products are extracted with a 55 kV electrostatic potential, subsequently accelerated to 55 keV, and focused by two electrostatic

¹See for instance the fluorination technique explained in Sec. 5.1

lenses to a parallel beam at the entrance of the separator magnet.

4. The double-focusing 55° magnet separates according to mass (in reality A/q), and refocuses the beams both in the horizontal and vertical directions.

Once we have the mass we want, we implant this separated beam in a support, either a tape for transport or a detector, surrounded by detectors depending on the experiment we want to perform. For instance, in some experiments telescopes for charged particles have been mounted on the left or right beam line. Another typical set-up used in recent experiments is an array of germanium detectors: the two super-segmented super-clover detectors of GSI and one germanium cluster detector, the three of them being placed in the central beam line. The tape transport systems are used for transporting activity from the collection to the measuring point or removing the daughter activity from the measuring point.

9.3 The TAS at GSI

In Sec. 2.2.2 we established the basis of the TAS technique. It was clear that the main request is to have a detector with a very high intrinsic efficiency and a very good geometry, covering as much as possible of the 4π solid angle around the radioactive source.

The characteristics mentioned above are perfectly fulfilled by the TAS installed at GSI. In Fig. 9.3 the TAS is shown as well as the tape system which transports the radioactive source inside the detector. As we see, the main NaI crystal is a cylinder ($\varnothing=h=35.6$ cm) with a hole in the direction of the symmetry axis, forming a well. The upper part of the well is closed by a plug detector, covering a solid angle very close to 4π . The lower part of the plug detector, the one near the source, holds the ancillary detectors: one germanium planar detector ($\varnothing 16$ mm \times 10 mm), to measure the X-rays and tag the electron capture processes, and two silicon detectors to measure the positrons and tag the β^+ -decay processes. The top silicon detector ($\varnothing 17.4$ mm \times 0.5 mm) sees the source from above, and the bottom silicon detector, below the source, was in reality a telescope ($\varnothing 17.4$ mm \times 35 μ m and $\varnothing 27.4$ mm \times 0.55 mm) to measure not only positrons but also protons or α particles. Below the silicon bottom detector there is a piece of beryllium which acts as absorber for the positrons, very useful to avoid the penetration of the charged particles into the crystal. The silicon-absorber mounting can be changed and has been altered during other experiments, for instance during the run for the measurement of the β -decay of ^{148}Dy and ^{148}Tb (Sec 11.1 and 11.2) the bottom silicon detector was not a telescope and the absorber was polyethylene instead of beryllium. In Fig. 3.1 one can see more details of the detector.

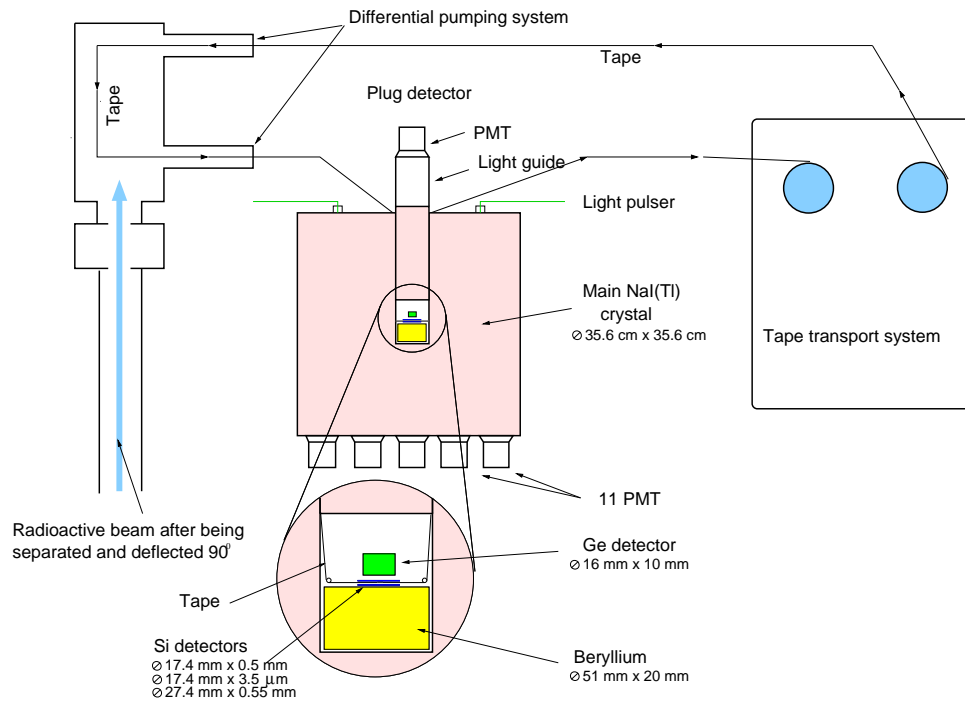


Figure 9.3: The Total Absorption Spectrometer at the on-line mass separator.

Finally, in Fig. 9.4 we have the efficiency curves of the GSI TAS. If we compare this with Fig. 5.5 we can appreciate that the total efficiency is in general larger for this detector than for Lucrecia, the one installed at CERN. This is due to the transverse hole in Lucrecia which is absent in the GSI TAS.

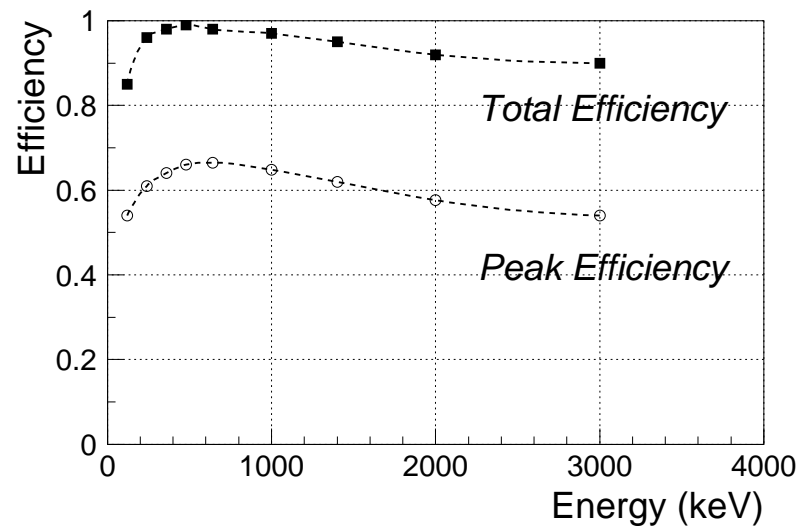


Figure 9.4: GSI TAS' total and photo-peak efficiency.

9.4 The measurement of ^{152}Tm β -decay

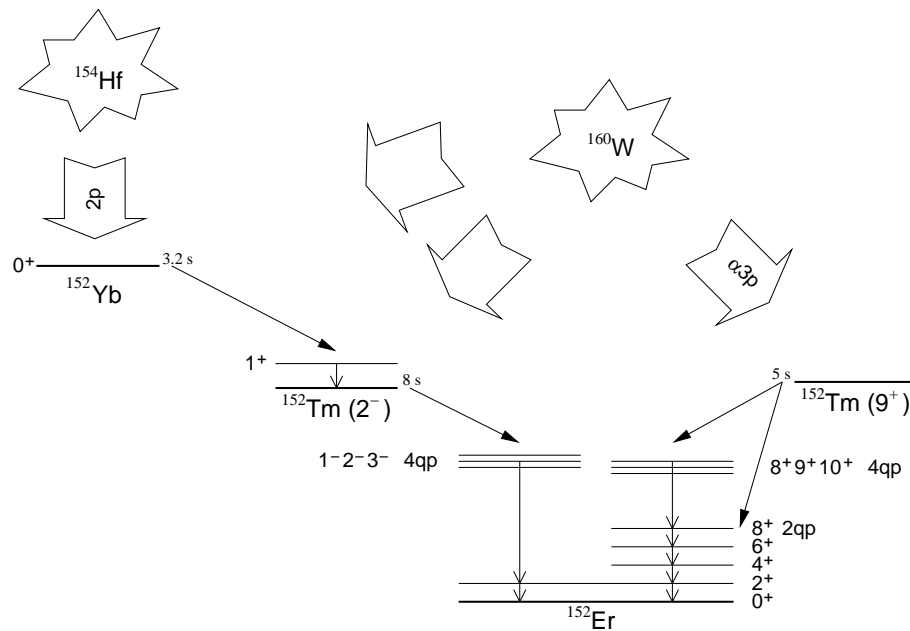
In the previous chapter we have presented the accelerator and separator facilities at GSI, and the Total Absorption Spectrometer coupled to the mass separator. In the following we will describe the experiment devoted to measure the decay of ^{152}Tm .

The nucleus of interest, as for all of the other odd- $N=83$ isotopes above the ^{146}Gd core, presents two isomers. The low-spin isomer $J^\pi=2^-$ has one proton in the $d_{3/2}$ orbital and two proton pairs coupled to 0^+ , partially occupying the three orbitals $d_{3/2}$, $s_{1/2}$ and $h_{11/2}$. The β -decay of this isomer can only happen when one proton pair occupies the $h_{11/2}$ orbital and one of the protons decays into a neutron in the $h_{9/2}$ orbital. The states populated in ^{152}Er are of four-particle character. The high-spin isomer $J^\pi=9^+$ has the odd proton not in the $d_{3/2}$ but in the $h_{11/2}$ orbital. This means that we will observe two components in this decay: one corresponding to the pairs in the $h_{11/2}$, as in the former case, and the other corresponding to the decay of the odd proton which can only populate a $2p$ state in ^{152}Er . This was already explained in Sec. 8.2 and shown graphically in Fig. 8.2.

One of the experimental challenges in the study of this nucleus (applicable to the other odd- $N=83$ isotopes studied in this work as well) was the isomeric selectivity achieved using the fusion-evaporation reaction, in other words, the production of one specific isomer and not the other. The key point for achieving this is to take advantage of the selection rules for β -decay and to use the fact that the 2^- isomer is the only one which can be populated in the β^+ -decay of the even- $N=82$ ^{152}Yb . In reality this isomer is not directly populated in this decay because the ground-state of ^{152}Yb has $J^\pi=0^+$ that can only populate 1^+ states in its daughter ^{152}Tm . Actually, it populates mainly one 1^+ state where all the GT strength is concentrated². The gamma de-excitation (E1) of this state feeds directly the 2^- isomer so that we never end up in the high-spin isomer 9^+ . Summarising, one can measure the decay of the 2^- isomer of ^{152}Tm very cleanly by producing and separating ^{152}Yb . The fusion-evaporation reaction chosen for the production of ^{152}Yb which also avoids the direct production of ^{152}Tm was $^{96}\text{Ru}(^{58}\text{Ni},2p)^{152}\text{Yb}$. The left side of Fig. 9.5 shows this sequence from the compound nucleus ^{154}Hf to the decay of interest. In the right side of the same figure we have the second reaction to produce the high-spin isomer: $^{102}\text{Pd}(^{58}\text{Ni},\alpha 3pn)^{152}\text{Tm}$. Unfortunately this second reaction populates not only the 9^+ isomer but also the 2^- which had to be subtracted afterwards.

For the two reactions different degraders and targets were prepared and mounted on two different wheels. In this way it was easy to adjust the final energy of the ^{58}Ni beam and to change between different targets with different thickness to optimise for the production of the isomer of interest. In the case of the low-spin isomer the en-

²In Sec. 11.1 the equivalent decay of the even- $N=82$ ^{148}Dy will be presented.

Figure 9.5: Selective production of the two isomers of ^{152}Tm .

ergy of the beam was degraded by a Ta foil of 3.25 mg/cm^2 placed in the first wheel, and, in the second wheel, the target was mounted on a backing foil of ^{92}Mo (97.37%) 0.99 mg/cm^2 thick facing the beam, in which some energy degradation occurred as well. All in all the ^{58}Ni beam arrived at the target with an energy of 4.53 MeV/u . The target was made of ^{96}Ru (96.53%) and had a thickness of 2.0 mg/cm^2 . For the second reaction, aimed at producing the high-spin isomer, no degrader was used. Thus, the ^{58}Ni beam arrived at the target with its original energy of 5.5 MeV/u . The target was ^{102}Pd (90.4%) with a thickness of 3 mg/cm^2 .

After the reaction, the products entered a FEBIAD type ion source [65]. There an electron beam ionised the products to a 1^+ charge state and then the ions were extracted with a 55 kV electrostatic potential. The separator magnet was set to select mass 152. The radioactive beam with this mass was then deflected vertically, implanted on the tape and moved periodically to the measuring position inside the TAS. As the measuring point was at atmospheric pressure and the beam came through a pipe with a quite high vacuum, a differential pumping system was used to move the source implanted on the tape from vacuum to 1 atm . However once every eight cycles the radioactive source was implanted not in the tape transport system of the TAS but in another tape station in which one Ge detector was placed at the implantation point. During this cycle the TAS was measuring background and the Ge detector was used to monitor periodically the production of the isotope of interest.

As in the ^{76}Sr case (see Part II), a symmetric cycle was used. The period of the cycle is normally set according to the half lives involved in the isobaric chain. Unfortunately, the half lives in this particular chain are not very different. The low and high-spin isomers of ^{152}Tm have respectively $T_{1/2}(^{152}\text{Tm}_{2-})=8.0$ s and $T_{1/2}(^{152}\text{Tm}_{9+})=5.2$ s [66]. On the other hand, in both reactions ^{152}Yb is produced, and in any case the decay of interest produces ^{152}Er . The former has $T_{1/2}(^{152}\text{Yb})=3.1$ s, and the latter $T_{1/2}(^{152}\text{Er})=10.3$ s [66]. Consequently, regardless of the cycle used, we will have at least three different decays in the spectra. We decided to measure the decay of the low-spin isomer in a symmetric cycle of 16 s, and for the high-spin isomer we used 12 s.

Examples of the on-line spectra registered during the run dedicated to measuring the decay of the low and high spin isomers of ^{152}Tm are shown in Figs. 9.6 and 9.7. The most striking thing about these figures is that, in the direct TAS spectrum (top), we can already observe the bump corresponding to a huge resonance between 4 and 6 MeV. In reality, we will see that this resonance is not so wide and its centroid lies at $\approx 4.3\text{-}4.5$ MeV, but in the direct spectrum we have the EC and the β^+ components together, and furthermore, we have all the possible contaminants in the spectra: the background and the decay of the other isotopes of the isobaric chain. On the other hand, in the X-ray spectra we observe that the highest peaks are the $\text{Er}(K_{\alpha 1})$ and $\text{Er}(K_{\alpha 2})$ at 48.2 keV and 49.1 keV respectively. This indicates that the cycle was appropriate in both the low and high-spin cases because these peaks appear as a consequence of the electron capture in ^{152}Tm . We also see that the peak at 50.7 keV is proportionally bigger in the decay of the low-spin isomer. This peak corresponds to the $\text{Tm}(K_{\alpha 1})$ and is present in the spectrum thanks to the β -decay of ^{152}Yb , which populates only the low-spin isomer.

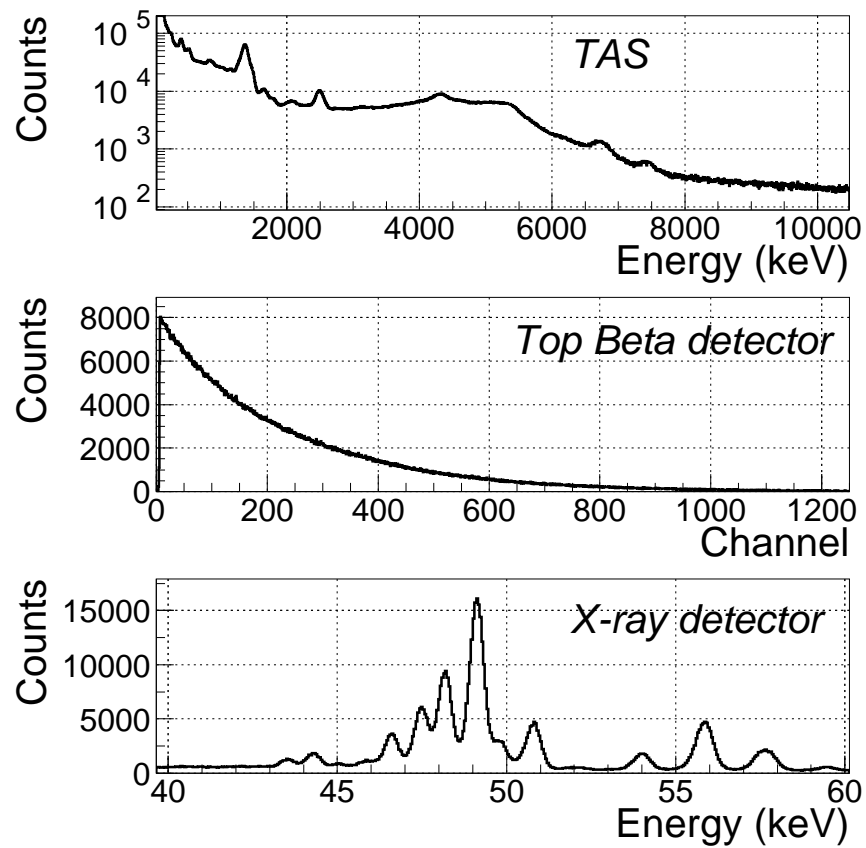


Figure 9.6: Direct spectra registered in the TAS and the ancillary detectors during the measurement of the ^{152}Tm 2^- decay.

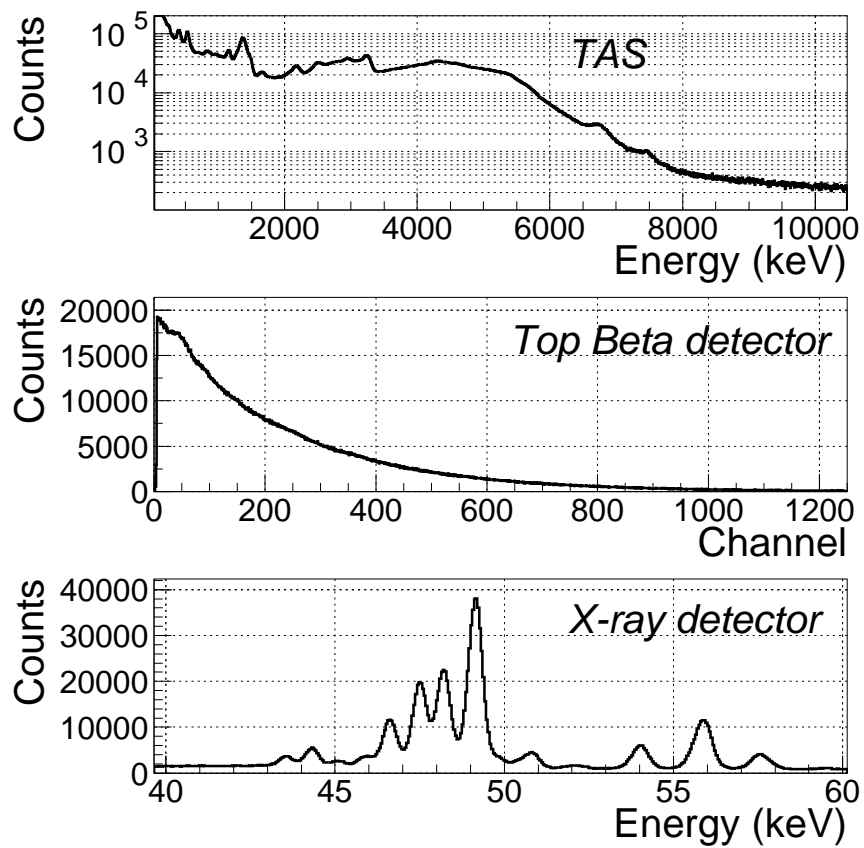


Figure 9.7: Direct spectra registered in the TAS and the ancillary detectors during the measurement of the $^{152}\text{Tm } 9^+$ decay.

Chapter 10

Data analysis of the ^{152}Tm β -decay

10.1 ^{152}Tm low-spin ($J^\pi=2^-$):

The sorting and preparation of the data

The main difference between the analysis we performed with the ^{76}Sr data in Chap. 6 and the one we face here with the ^{152}Tm data is that in the latter we do not have any strongly converted line as we had in the former. This means that now we can set a coincidence with the appropriate X-ray and separate cleanly the EC component of the decay. We could not do this in the ^{76}Sr case because there was a very strongly converted transition which produced the same X-rays for the EC and for the β^+ decay. In the present case we will analyse only the EC component of the decay because it has some advantages with respect to the β^+ : Firstly, the coincidence on the X-rays gives a very clean spectrum almost free of any isobaric contamination or background. Secondly, the energy window available for the decay is 1022 keV larger in the EC process than in the β^+ . Apart from these two advantages we must remember that the ratio EC/β^+ can be easily calculated as it depends only on the phase space available in the final state and on the electromagnetic part of the interaction, and these two things are very well known and tabulated for instance in Ref. [56]. This means that once we obtain the β -intensity distribution from the EC, we can calculate the total β -intensity distribution $I_\beta(E)$. Summarising, in all the cases analysed from here on, we will use only the EC component of the decay but at the end we will obtain the total β -intensity and Gamow-Teller strength.

In order to select the EC component of the decay of interest we need to sort the data demanding a coincidence on the X-rays, in particular we need to set a gate covering the $\text{Er}(K_{\alpha 1})$ and $\text{Er}(K_{\alpha 2})$ peaks and accumulate then the TAS spectrum. Unfortunately, even with a very conservative (narrow) gate, we will include some counts coming from the tails of the neighbouring peaks which are the $\text{Ho}(K_{\alpha 1})$ and the $\text{Yb}(K_{\alpha 2})$. In Fig. 10.1 we have the X-ray spectrum and the gates that we set to tag the EC decay of ^{152}Tm and also the possible contaminants (decay of ^{152}Er and ^{152}Yb). We have chosen a very narrow gate covering only part of the $\text{Er}(K_\alpha)$ peaks

in order to avoid the tails of the neighbouring peaks. Unfortunately, in the TAS spectrum in coincidence with this gate we still see the contaminants (see Fig. 10.2 top). Therefore we will use the other two gates to determine the contaminants and subtract their contribution to our spectrum. The $\text{Er}(K_\beta)$ peaks have not been used because they are completely contaminated by the other decays as we see in Fig. 10.1.

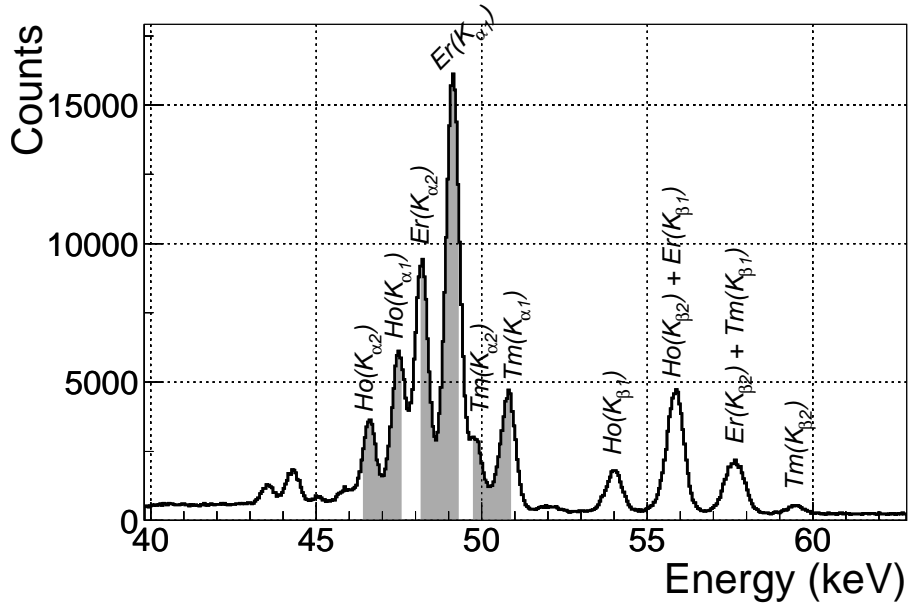


Figure 10.1: X-ray spectrum during the measurement of the decay of $^{152}\text{Tm } 2^-$. The shade regions represent the gates set for the coincidences.

The determination of the normalisation factors for the contaminants and their subtraction are shown in Fig. 10.2. The upper panel shows, in black colour, the resulting TAS spectrum in coincidence with the $\text{Er}(K_\alpha)$ gate in the X-ray spectrum. Overlaid, in red colour, there is the sum of the TAS spectra in coincidence with the other two gates in the X-rays multiplied by their respective normalisation factors. These factors have been calculated using the peaks at 482 keV and 180 keV in the TAS spectrum which correspond to the decay of ^{152}Yb and ^{152}Er respectively. In the lower panel the resulting spectrum obtained after the subtraction is plotted. Already without any analysis we can appreciate the huge resonance peaked at ≈ 4.3 MeV.

At this point one should clean the spectrum of pile-up. However we can not see any count in the spectrum beyond the Q_{EC} because there is no pile-up. The counting rate was always below 2 kHz in the TAS (1.5 kHz of background) and this was low enough to avoid completely the pile-up contribution. However there is another contamination very hardly seen in the spectrum. At ≈ 2.2 MeV we see something that suggests the possibility of some small contribution from the decay

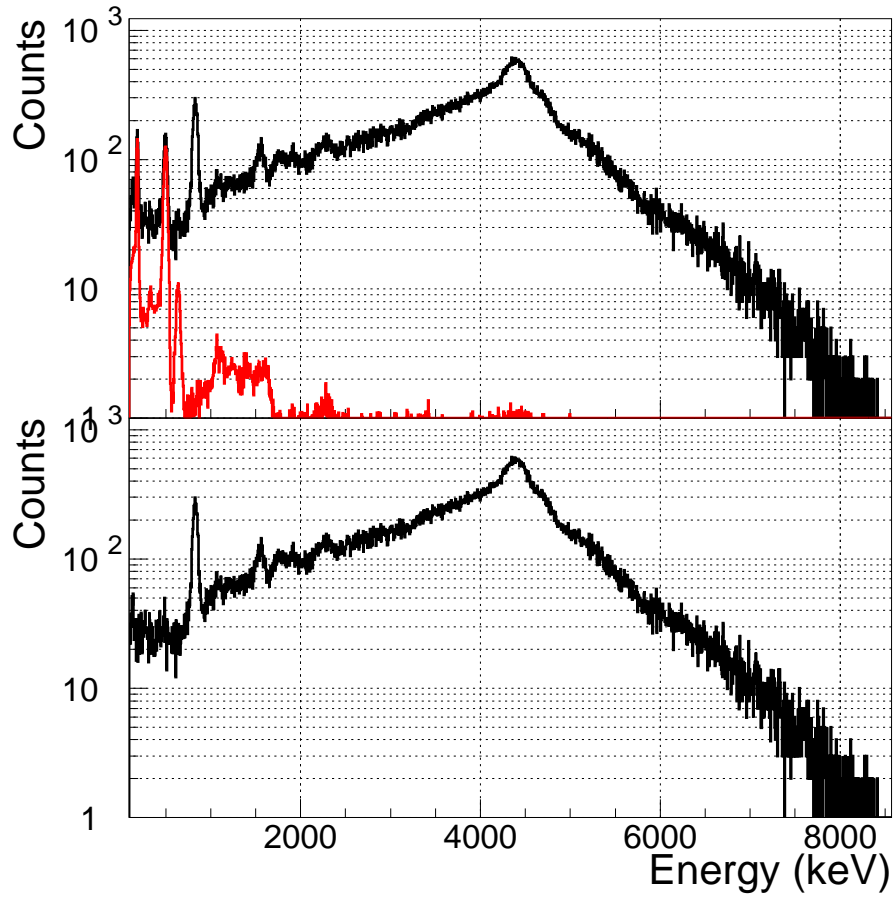


Figure 10.2: Top: EC component of the decay of the low-spin isomer of ^{152}Tm (black) and its contaminants (red). Bottom: Resulting spectrum after the subtraction.

of the high-spin isomer. At this energy there is the 8^+ $2p$ state which can be fed directly from the decay of the ^{152}Tm 9^+ isomer and not from the decay of the 2^- . To make this clear we can have a look at the upper panel of Fig. 10.3. There we have in black colour the spectrum corresponding to the 2^- isomer decay, and in red colour, a clean spectrum of the 9^+ decay. In this comparison we see the position of the 8^+ $2p$ state exactly in the place where we observe a small bump in the black spectrum of the 2^- decay. The red spectrum of the 9^+ decay has been taken from two sections ahead (Sec. 10.3) and we will use it to clean the current spectrum, but this will be explained later.

In order to confirm the small contribution of the high-spin isomer to the spectrum of the low-spin isomer, we can look for a peak coming from the de-excitation of the

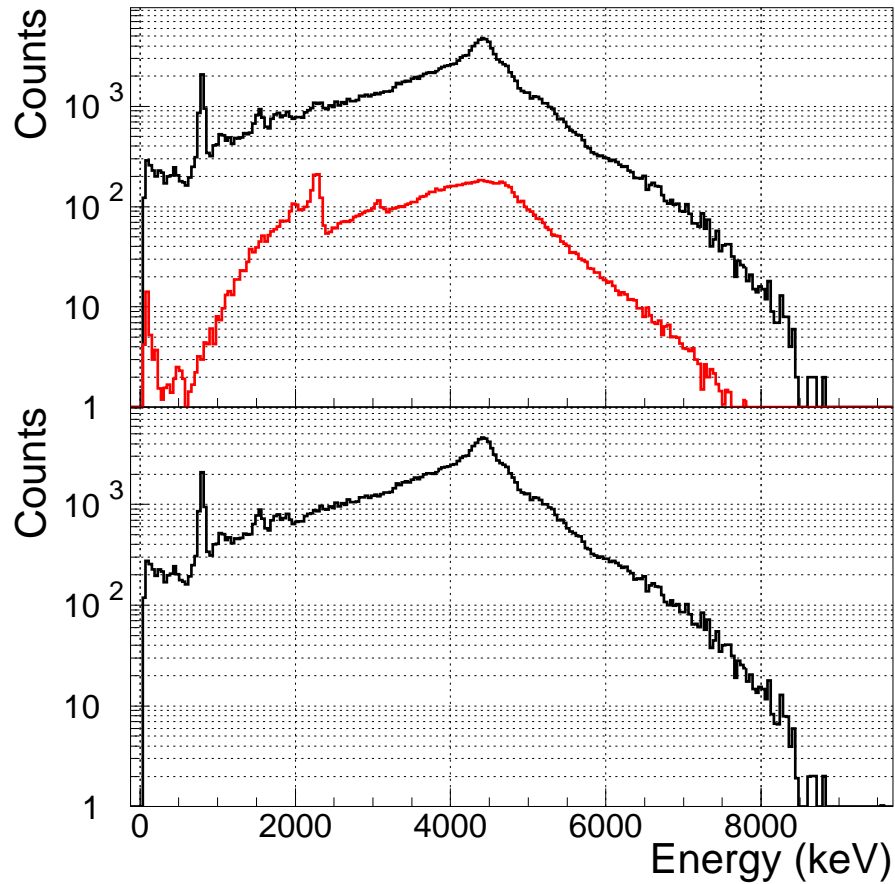


Figure 10.3: Top: EC spectrum of the decay of the low-spin isomer of ^{152}Tm (black) clean from isobaric contaminants. Overlaid in red colour: Clean EC spectrum of the decay of the high-spin isomer of ^{152}Tm . Bottom: Resulting spectrum after the subtraction.

8^+ $2p$ state in the germanium detector¹. Actually, the $8^+ \rightarrow 6^+$ transition should leave a very clear signature: a peak at 279.9 keV in the germanium spectrum. This spectrum is shown in Fig. 10.4 and the peak at 279.9 keV confirms our suspicion: the low-spin spectrum is contaminated by the high-spin decay. This is surely due to impurities in the target. With the aim of estimating the ratio between 2^- decay and 9^+ decay that we have in the spectrum we calculated the γ -intensities of the peaks at 279.9 keV and 808.2 keV. Dividing these intensities, both corrected by the efficiency of the detector, we concluded that 5.7% of the spectrum was in reality coming from the decay of the 9^+ isomer, or in other words, the ratio between both contributions was $9^+/2^-=0.06$. If we remove the part of the 808.2 keV peak which

¹Apart from the X-rays, we measured high energy γ -rays with the germanium detector using a second signal from the detector and a very low amplification.

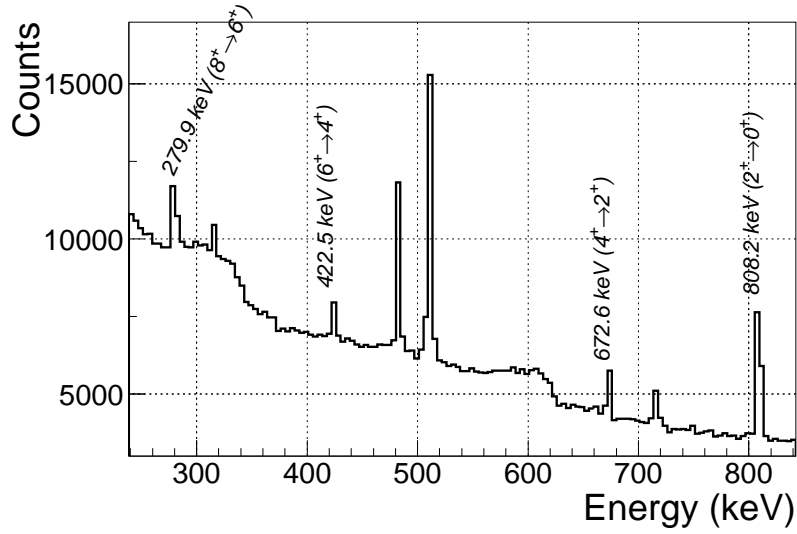


Figure 10.4: Low amplification germanium spectrum. We see transitions that can only come from the decay of the high-spin isomer.

comes from the 9^+ decay (subtracting the intensity of the 422.5 keV peak) and make the division, we obtain again the ratio $9^+/2^-=0.06$. At the same time, this number is in agreement with the data taken at GSI some years ago, when the same decay was measured, using the same target, in a high resolution and high efficiency setup of 6 Ge-cluster detectors [67].

At this stage we can use a clean spectrum of the decay of the high-spin isomer and subtract it from the contaminated spectrum we are dealing with. Fig 10.3 shows such a subtraction. In the upper panel we have the decay of the low-spin isomer with the small contamination (black curve) and overlaid in red colour there is the contamination: A clean spectrum of the decay of the 9^+ taken from Sec. 10.3. The lower panel shows the result of the subtraction. We can appreciate that the bump at ≈ 2.2 MeV disappears in the lower spectrum. This is the final spectrum that we have to analyse. It looks as if it had more statistics than in Fig. 10.2, but this is because it has been re-binned to have the same calibration as the simulated response function. In this figure each energy bin covers about 40 keV.

10.2 ^{152}Tm low-spin ($J^\pi=2^-$): Analysis using the EM algorithm

As in the ^{76}Sr case presented in Sec. 6.3 we need to calculate the response function of the detector and validate it with a well known source. Again we used ^{24}Na

for this comparison and the *GEANT4* code [24] for the Monte Carlo simulations. Fig. 10.5 shows the simulation of the ^{24}Na source compared to the measured one. The agreement is remarkably good and this makes us trust the individual response functions that we have simulated for mono-energetic γ -rays.

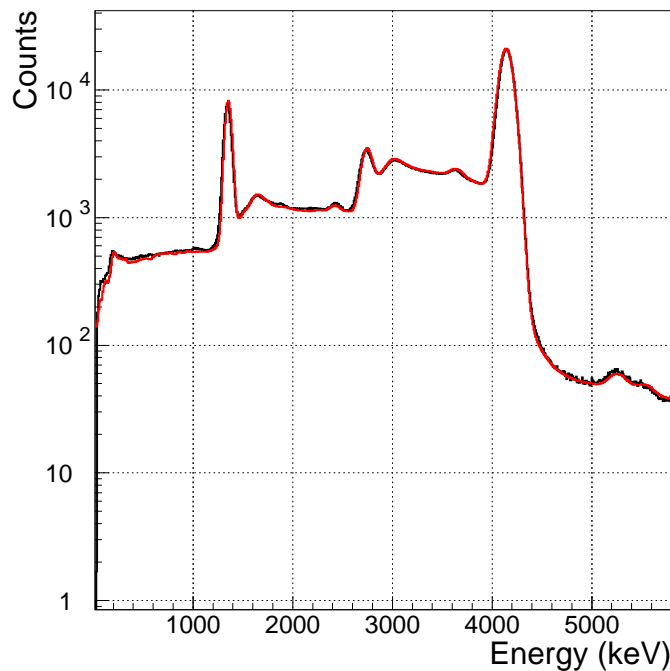


Figure 10.5: Simulation of the β -decay of ^{24}Na (red) overlaid to the measured ^{24}Na source (black).

At this point we need to construct the response function of the detector for this specific decay using the individual simulated and validated response functions (for details see Sec. 6.3). For this purpose we need the level scheme of the daughter. We have used two different sources for this level scheme: The results of Ref. [68], and a preliminary evaluation of the data taken with the six Ge-cluster detectors at GSI some years ago [67]. These two references provided a reliable level scheme up to 2129.0 keV, from that point on we used the statistical model. In this occasion the parameters for the back-shifted Fermi gas model were $a = 14.99 \text{ MeV}^{-1}$ and $\Delta = 0.69 \text{ MeV}$ [69, 67]. These parameters were extracted from experimental data but are also consistent with the parametrisation of [53]. For the branching ratios the parametrisation of Ref. [52][53][54, 55] were used for the E1, M1 and E2 transitions respectively. The whole procedure is similar to the one described in Sec. 6.3.

Having a level scheme with gamma branching ratios for the daughter nucleus, and the individual response functions simulated and validated with the ^{24}Na source

(see Fig. 10.5), we can construct the response function of our detector to the decay of interest following Ref. [23], and then apply the EM algorithm to the experimental data (see Sec.3.1). This was done, and the result after 200 iterations appears in Fig. 10.6. As indicated before, already from the experimental spectrum and without

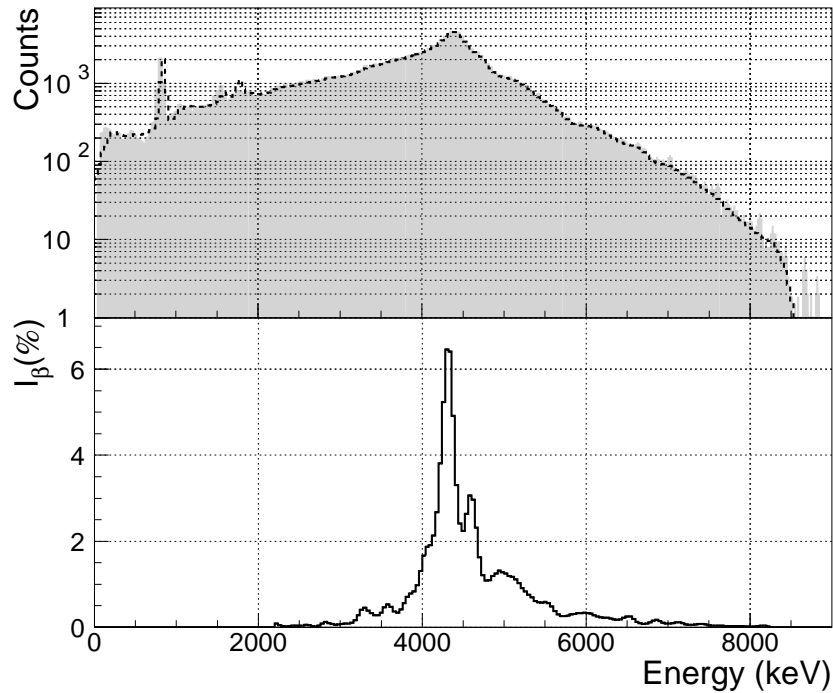


Figure 10.6: Top: Experimental spectrum for the ^{152}Tm 2^- decay (grey shade). Overlaid there is the recalculated spectrum using the result after the analysis (dashed line). Bottom: Resulting $I_\beta(E)$ after the data deconvolution.

any analysis one can predict that the decay of this isomer populates a resonance at ≈ 4.3 MeV in the daughter nucleus. The results of the analysis corroborate this prediction.

10.3 ^{152}Tm high-spin ($J^\pi=9^+$): The sorting and analysis of the data

In this section we will show the preparation and analysis of the data corresponding to the decay of the high-spin isomer of ^{152}Tm but without entering into details as deeply as in the previous section. The reason is that the procedure to clean the data from contaminants is similar to that described in the previous section and also in Sec. 6.2 when the decay of ^{76}Sr was presented. There are only three remarks to be made:

1. The gates on the X-rays have been kept the same as in the low-spin case for the ^{152}Tm decay as well as for the isobaric contaminants. With these gates and calculating again the normalisation factors for the contaminants the spectrum of the decay of the high-spin isomer has been cleaned, removing the contributions from the ^{152}Yb and ^{152}Er decays.
2. In the measurement of the 9^+ isomer the counting rate in the TAS crystal was higher than 3 kHz and therefore the first order pile-up has been calculated and removed as described in Sec. 6.2. The clean 9^+ spectrum without isobaric contaminants and pile-up is the black one in the upper panel of Fig. 10.7.

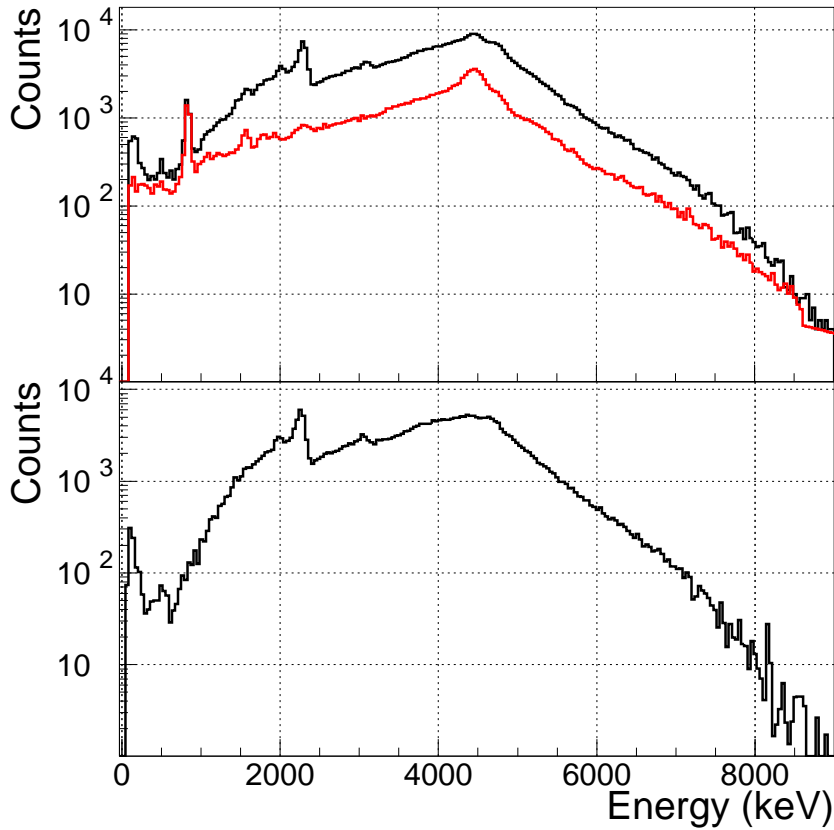


Figure 10.7: Top: The black curve is the ^{152}Tm 9^+ decay clean of any isobaric contamination. The red spectrum is the ^{152}Tm 2^- decay plus the pile-up. It has been normalised to the peak at 808.2 keV. Bottom: Result of the subtraction of the two spectra of the upper panel.

3. As mentioned before, the 9^+ decay spectrum comes always contaminated by the 2^- decay, thus we need to subtract this contamination using the 2^- decay spectrum clean of isobaric contaminants. For that we have normalised to the

peak at 808.3 keV ($2^+ \rightarrow 0^+$) which can only appear in the low-spin decay in a total absorption spectrum. Fig. 10.7 shows the result of this last subtraction. The lower panel shows the clean spectrum which has been used not only for the analysis but also for cleaning the spectrum of the 2^- decay in Sec. 10.1.

Now that we have a clean spectrum of the ^{152}Tm 9^+ decay we can apply the EM algorithm as we have done before with the low-spin isomer and obtain the β -intensity distribution $I_\beta(E)$. For that we need again the level scheme of the daughter. The lower part of this scheme was taken from Ref. [70] up to 3 MeV, and from that point on the statistical model was used with the same parameters as in the low-spin isomer decay. The results of the analysis are presented in Fig. 10.8. Again we see a resonant structure whose main peak lies at ≈ 4.5 MeV, but this time we also observe high beta feeding to the 8^+ level at 2183.2 keV. This is the 2p level that we have mentioned before, whereas the resonant structure from 4 to 6 MeV corresponds to the 4p levels also fed in the Gamow-Teller transition $\pi h_{11/2} \rightarrow \nu h_{9/2}$ in a region of high level density. It is important to remember that, at this stage, we are talking about the $I_\beta(E)$, but the physics underneath will be discussed in connection with the B(GT) which is presented in the next section.

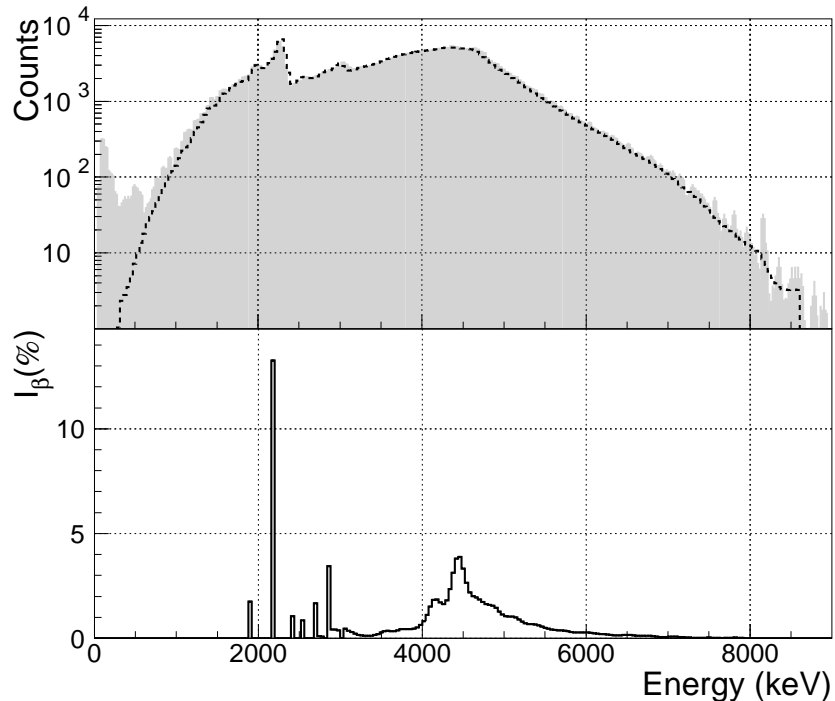


Figure 10.8: Top: Experimental spectrum for the ^{152}Tm 9^+ decay (grey shade). Overlaid is the recalculated spectrum using the result after the analysis (dashed line). Bottom: Resulting $I_\beta(E)$ after the data deconvolution.

10.4 Results and discussion: The GT strength distribution in the decay of ^{152}Tm

Going from the β -intensity distribution $I_\beta(E)$ to the $B(\text{GT})$ is easy once we know the half-life and the Q_{EC} of the decay. In our case the half-lives of the two isomers are $T_{1/2}(^{152}\text{Tm}_{2^-})=8.0(10)$ s and $T_{1/2}(^{152}\text{Tm}_{9^+})=5.2(6)$ s [66]. For the Q_{EC} the situation is more complicated. The first time this analysis was performed, there was no experimental information on the Q_{EC} of any of the isomers. They were estimated to be both 8600 keV, but only based on the systematics of the region. Therefore we decided to use the end point of the EC spectrum in the TAS to estimate them. The results were $Q_{EC}(^{152}\text{Tm}_{2^-})=8800(200)$ keV and $Q_{EC}(^{152}\text{Tm}_{9^+})=8700(200)$ keV. The uncertainties were large but at least these were experimental values and not estimates from systematics. Using the end point of the positrons in the Ge detector we obtained values compatible with the former ones but with higher uncertainties. In Fig. 10.9 we have, on the left, the end point of the EC spectrum in the TAS for the decay of the low-spin isomer. The linear fit can be done representing on the Y axis the square root of the number of counts. From the intersection of the resulting line with the X axis we obtained the Q_{EC} value. The right side of the figure is the end point of the positron spectrum in the Ge detector. The black line is simply to guide the eye. This line crosses the X axis in a point which gives a Q_{EC} value compatible with the previous one but with a much bigger uncertainty.

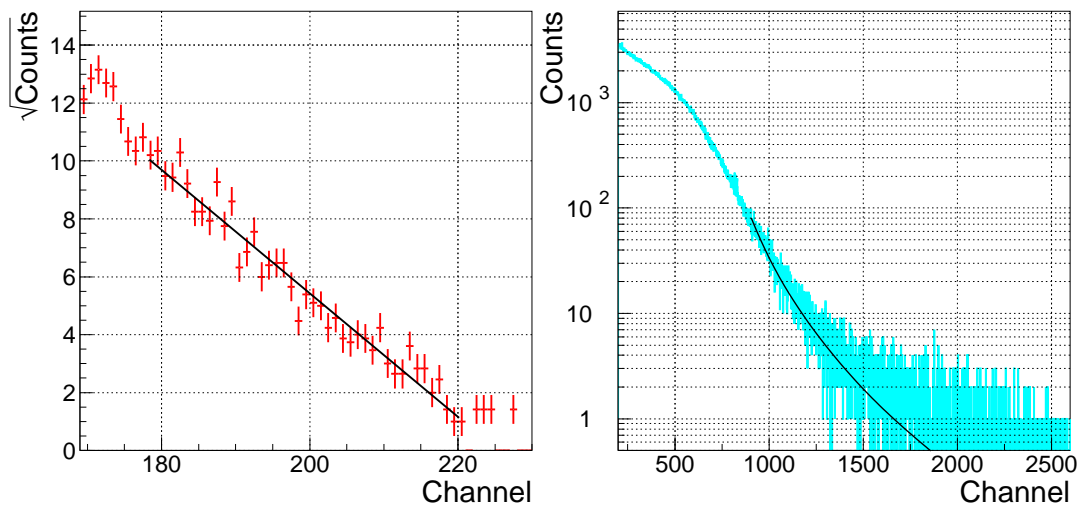


Figure 10.9: Left: End point of the EC spectrum measured in the TAS for the decay of the 2^- isomer. Right: End point of the positron spectrum measured in the Ge detector for the same decay.

Using the Q_{EC} values obtained from the end point of the EC spectra, and the statistical rate Fermi integral tabulated in Ref. [56] we obtained a first result for the $B(\text{GT})$ distribution of both isomers. However, meanwhile a new compilation of nuclear masses (consequently Q_{EC} values) has been published [57]. For the low-spin isomer a new experimental Q_{EC} value is presented: $Q_{EC}(^{152}\text{Tm}_{2^-})=8730(70)$ keV. This is compatible with our measurement, but it has higher accuracy, therefore we will use this value for the ^{152}Tm 2^- decay. However for the high-spin isomer the value given in [57] still comes from systematics and here we have decided to use our own result $Q_{EC}(^{152}\text{Tm}_{9^+})=8700(200)$ keV.

After all these considerations we present the $B(\text{GT})$ distribution measured in the β^+ -decay of ^{152}Tm in Fig. 10.10. The upper panel corresponds to the decay of the high spin isomer and the lower panel to decay of the low-spin one. In both distributions we observe a strong resonance peaked at ≈ 4.5 and ≈ 4.3 MeV respectively.

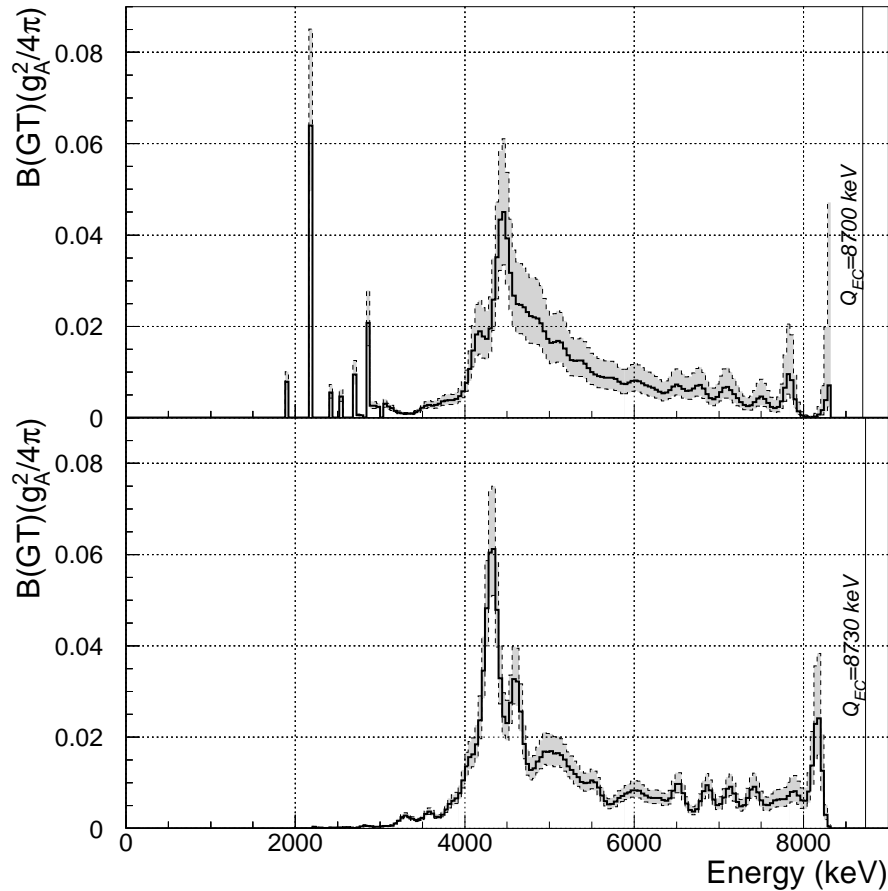


Figure 10.10: $B(\text{GT})$ distribution in the β^+ -decay of ^{152}Tm . Upper panel: high-spin isomer (9^+) decay. Lower panel: low-spin isomer (2^-) decay.

The grey shade in the figure is the uncertainty mainly due to the Q_{EC} and the half-life. It is smaller in the low-spin case because the uncertainty in the Q_{EC} is 70 keV to be compared with the 200 keV uncertainty in the case of the 9^+ . These uncertainties also propagate to the sum of the $B(GT)$, which gives a value of:

$$\boxed{\sum^{8.0 \text{ MeV}} B(GT)_{9^+} = 1.3(3) \frac{g_A^2}{4\pi}}$$

$$\boxed{\sum^{8.0 \text{ MeV}} B(GT)_{2^-} = 1.3(2) \frac{g_A^2}{4\pi}}$$

Again the reason for the large uncertainty is mainly the Q_{EC} .

Now that we have some final results for the decay of the two isomers of ^{152}Tm we can compare them with the results obtained in previous β -decay studies of this nucleus. For the low spin isomer we have already used Ref. [68] to build the level scheme of the daughter. Unfortunately, in that article only four levels were identified above the ground-state of the daughter, the last one being at 1715 keV. The authors agreed that most of the β -decay of ^{152}Tm populated levels at higher energy and that they could only observe the low-lying levels indirectly fed through γ transitions. This is the reason why there is no information on the $\log ft$ in that article [68]. In the case of the high-spin isomer the situation is better. Two high resolution experiments were performed: one at HMI (Berlin) and a second one at GSI (Darmstadt). In the first experiment a setup of 12 Ge detectors with a multiplicity filter of 42 BGO detectors was used. The results are still unpublished but the decay scheme appears in Ref. [70]. Our results for the high-spin isomer are compared with those of Ref. [70] in Fig 10.11. There we can appreciate the effect already mentioned: in the high resolution experiment the bulk of the strength is shifted downward. However one has to recognise that in this case the results from the high resolution experiment are of excellent quality in the sense that some states of the resonance are already identified in [70] in spite of the high excitation energy. The sum of the $B(GT)$ gives an amount of $0.46 \frac{g_A^2}{4\pi}$ to be compared with our resulting $B(GT)$ integrated up to 8 MeV: $1.3(3) \frac{g_A^2}{4\pi}$. The global reduction of the strength seen in [70] due to the *pandemonium effect* (Sec. 2.2.1) is bigger than 60% even in this case in which some states of the resonance are detected.

At this point we could start a discussion about the quenching, the Gamow-Teller resonance in the region and the possible theoretical calculations of the $B(GT)$ in this cases, but all the discussion is left for Chap. 12 in which we will take into account other decays studied in this region. Those other measurements and results are presented in summary form in the next chapter. The experimental techniques and analysis methods are the same as those used in the cases described so far.

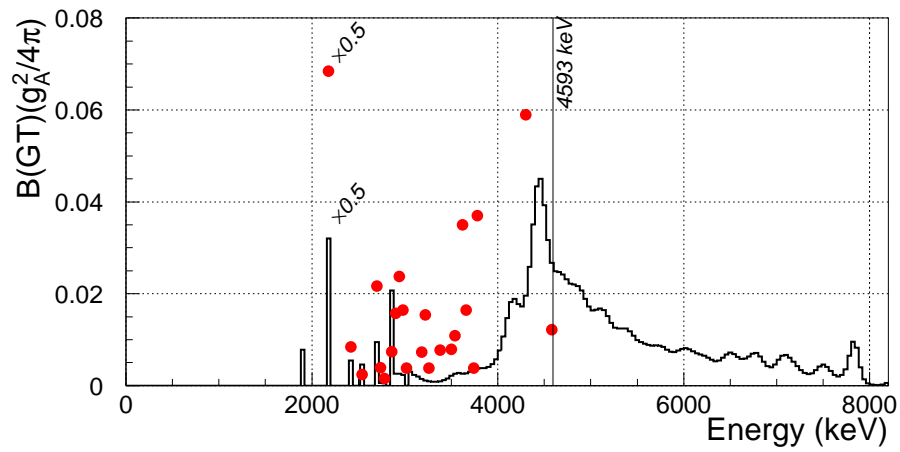


Figure 10.11: Comparison between the results of this work (solid line) and those from Ref. [70] using a high resolution setup (red dots). The vertical line indicates the position of the last level seen in [70].

Chapter 11

Summary of the other decays in the region pertinent to the present discussion: ^{148}Dy , ^{148}Tb and ^{156}Tm

11.1 Beta decay of ^{148}Dy

In a simplified picture one can consider ^{148}Dy as an even-even nucleus with only two protons above the ^{146}Gd core. Therefore its ground-state is the consequence of the coupling of the proton pair to 0^+ , with the two protons partially occupying the three available orbitals $d_{3/2}$, $s_{1/2}$ and $h_{11/2}$. This is represented in Fig. 11.1 where we see that the only allowed decay, which involves the breakup of the pair, will populate only one state of two-particle character in the daughter where all the Gamow-Teller strength will be concentrated: $[\pi h_{11/2}^2]_{0^+} \rightarrow [\pi h_{11/2} \nu h_{9/2}]_{1^+}$.

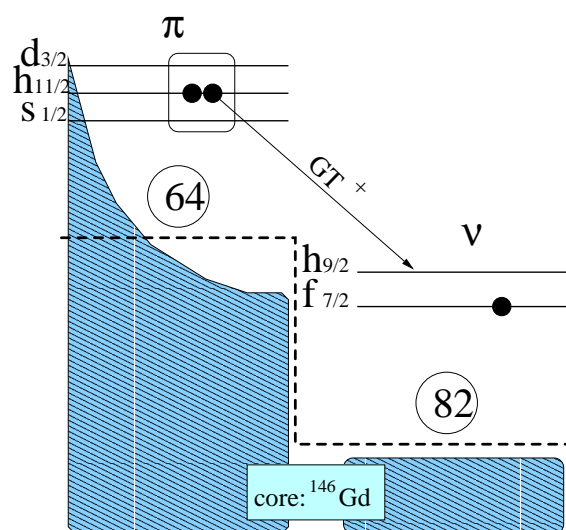


Figure 11.1: Extreme single-particle representation of the β -decay of ^{148}Dy .

The β^+ -decay of ^{148}Dy was measured twenty years ago with a high resolution setup of three Ge detectors (two coaxial for γ -rays and one planar for X-rays) and the results were reported in Ref. [71]. Although in that work the authors could measure the Gamow-Teller $2p$ excitation at 620 keV, the question of whether there was β population at higher energy remained unanswered due to the low efficiency of the detectors used at that time. The β^+ -decay of ^{148}Dy was measured some years later with the TAS at the On-line Mass Separator of GSI. The reaction chosen to produce the isotope of interest was $^{93}\text{Nb}(^{58}\text{Ni},3p)^{148}\text{Dy}$. The ^{58}Ni was accelerated in the *UNILAC* up to 5.3 MeV/u and then hit the ^{93}Nb target 5.17 mg/cm² thick. A FEBIAD type ion source [65] was also used in this case. The tape transport system was set for symmetric cycles of 400 s, optimised for the decay of ^{148}Dy , with $T_{1/2}=198$ s. The daughter, ^{148}Tb , has $T_{1/2}=60$ min, therefore with such a short cycle the main activity should be the ^{148}Dy β -decay.

Without going deeper into the description of this measurement, we present here the results after the analysis of the data. The left side of Fig. 11.2 is the EC component of the decay of ^{148}Dy measured with the TAS. The dashed line is the recalculated spectrum after the analysis process, which fits very well the experimental spectrum (grey shade). At the right side of the same figure the B(GT) distribution of this decay is shown. As we see, almost the total strength lies at the 620 keV level and only a very small fraction lies beyond this point.

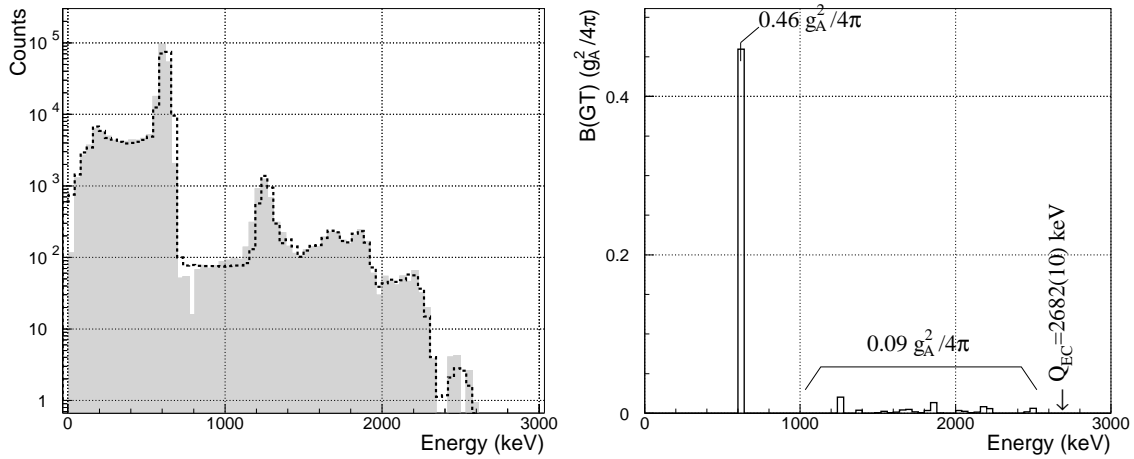


Figure 11.2: Left: Experimental EC spectrum of the ^{148}Dy decay (grey shade) and recalculated spectrum after the analysis (dashed line). Right: Gamow-Teller strength in the β -decay of ^{148}Dy .

The total strength measured in this decay is:

$$\sum^{2.6\text{MeV}} B(GT) = 0.55(1) \frac{g_A^2}{4\pi}$$

The importance of this number lies in the fact that it serves as a pattern to quantify the total strength and the retardation of the Gamow-Teller transition due to the break of a single proton pair in the $h_{11/2}$. This pattern could also be extracted from the decay of the low-spin isomer of ^{150}Ho or ^{152}Tm , but these cases are very difficult to measure with the high resolution technique. In contrast, the fact that the decay of ^{148}Dy is concentrated in one single state in ^{148}Tb makes this case easier to measure with this technique, in fact, the strength distribution measured in [71] with the Ge detectors was very similar to our result. However with the low efficiency of the Ge detectors one can never be sure of the result beyond 1.5 or 2 MeV. In any case, in Ref. [71] they could detect $0.04 g_A^2/4\pi$ beyond the level at 620 keV, to be compared with our number $0.09 g_A^2/4\pi$. The $B(\text{GT})$ to the Gamow-Teller state at 620 keV reported in [71] is $0.44 g_A^2/4\pi$ and now we have measured $0.46 g_A^2/4\pi$. All in all the difference between our results and those from [71] is not significant. One should mention here that ^{148}Dy is the cleanest case to investigate the breakup of a proton pair since here we just have one proton pair above the ^{146}Gd core.

In any case, the first thing we should do now is to check whether our result for this decay is compatible with our result for the decay of the 2^- isomer of ^{152}Tm . In principle, in terms of total strength, we have said in the previous paragraph that the decay of ^{148}Dy is a pattern for the total strength in the decay of one proton pair above the ^{146}Gd core. On the other hand the configuration of the low-spin isomer of ^{152}Tm on the proton side contains, in the extreme single-particle approach, two proton pairs above the ^{146}Gd core. Therefore the total strength measured in the decay of $^{152}\text{Tm } 2^-$ should be twice as much as in the decay of ^{148}Dy . Our results for the ratio between these two numbers is exactly:

$$\frac{\sum B(\text{GT})_{152\text{Tm } 2^-}}{\sum B(\text{GT})_{148\text{Dy}}} = \frac{1.3(2)}{0.55(1)} = 2.3(4)$$

very much in agreement with our expectations.

Summarising, our results for this decay are not different from those of Ref. [71]. However, taking into account the importance of this decay, the confirmation of the results from [71] justified the effort to measure the decay of ^{148}Dy with the most efficient technique available, namely the TAS technique. We will use this result in Chap. 12 where we discuss other results.

This work has been accepted for publication in *Physical Review C* [72].

11.2 Beta decay of ^{148}Tb

^{148}Tb is similar to ^{152}Tm in the sense that it is an odd- $N=83$ with two isomers: the low-spin isomer with $J^\pi=2^-$, and the high-spin one with $J^\pi=9^+$. The configurations of these states regarding valence particles correspond to the ones already

shown for the ^{152}Tm case. The only unique aspect of this nucleus is that it has 65 protons, and this means that all the proton pairs which can be moving around the three orbitals $2d_{3/2}$, $3s_{1/2}$ and $1h_{11/2}$ must be promoted from the ^{146}Gd core. In this sense we can say that the low-spin isomer should not decay by allowed Gamow-Teller transitions unless there are proton pairs crossing the gap above $Z=64$. From a $(d, ^3\text{He})$ experiment on a ^{144}Sm target [73] we know that this pair scattering occurs. The authors of [73] agree that there is an occupation of 1.6(3) protons in the $1h_{11/2}$ orbital in the ground-state of ^{144}Sm . We expect the same pair scattering in the nuclei above ^{146}Gd , therefore we should observe the β -decay of $^{148}\text{Tb } 2^-$ which corresponds to the breakup of the pair.

The experiment devoted to measuring the β -decay of the two isomers of ^{148}Tb took place at the Mass Separator of GSI. The same technique used in the case of ^{152}Tm to produce the two isomers separately was applied to this measurement. The low-spin isomer was produced cleanly as the decay product of ^{148}Dy . The reaction to produce this nucleus was already presented in the previous section: $^{93}\text{Nb}(^{58}\text{Ni}, 3p)^{148}\text{Dy}$. The β -decay of the product ^{148}Dy populates mainly the state at 620 keV as we saw in Fig. 11.2 left, and this state de-excites through γ emission populating only the low-spin isomer in ^{148}Tb . The half-lives involved in this decay chain are: $T_{1/2}=198$ s, 60 min, and 74.6 y for ^{148}Dy , $^{148}\text{Tb } 2^-$ and ^{148}Gd respectively. Therefore, instead of the symmetric cycles used in the other measurements presented here, on this occasion the cycle was a long irradiation to produce a strong source, a delay time without measuring to get rid of the ^{148}Dy activity, and then a measuring time to enhance the decay of $^{148}\text{Tb } 2^-$. The delay was chosen to be approximately five times the half-life of ^{148}Dy , and the measuring time was between one and two hours.

The EC spectrum of the decay of $^{148}\text{Tb } 2^-$ is plotted on the left side of Fig. 11.3. The right side of the same figure corresponds to the GT strength in this decay.

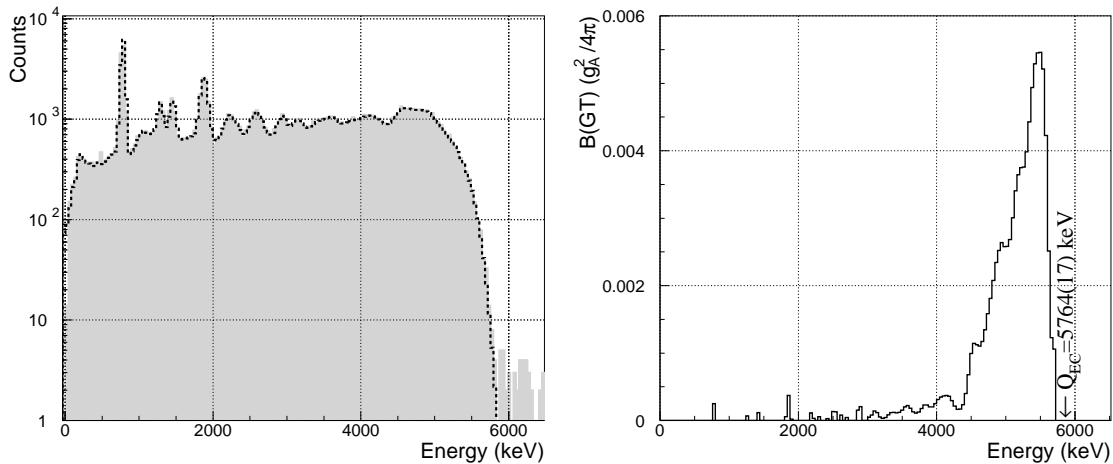


Figure 11.3: Same as in Fig. 11.2 for the decay of $^{148}\text{Tb } 2^-$.

The total strength summed up to 5.7 MeV is:

$$\boxed{\sum^{5.7\text{MeV}} B(GT) = 0.10(1) \frac{g_A^2}{4\pi}}$$

This value is certainly very low, but this is understandable if we recall the fact that in principle, neglecting the pairing interaction, there are no protons filling the $h_{11/2}$ orbital and therefore we should not observe any allowed β -decay. However, we know that there are certainly proton pairs scattered from the ^{146}Gd core and therefore the occupation of the $h_{11/2}$ is not zero. Taking the results from [73] and our results of Sec. 11.1 for the decay of ^{148}Dy we can take the following points into consideration:

1. The occupation of the $h_{11/2}$ in ^{148}Dy is not only one proton pair but one proton pair plus the proton pairs scattered from the ^{146}Gd core. Following Ref. [73] we will assume that ^{148}Dy has 0.80(15) proton pairs scattered from the core and occupying the $h_{11/2}$ orbital as this is the number that the authors of [73] measured for ^{144}Sm .
2. In Sec. 11.1 we presented our results for the decay of ^{148}Dy . For the total $B(GT)$ we measured $0.55(1) \frac{g_A^2}{4\pi}$. Assuming that we have 1.80(15) proton pairs in the $h_{11/2}$ orbital we can estimate that the $B(GT)$ per proton pair amounts to $0.305(26) \frac{g_A^2}{4\pi}$.

Overall, for the present case, namely the decay of $^{148}\text{Tb } 2^-$, we should expect to observe a total $B(GT)$ near 0.24(5). However the measured $B(GT)$ for this case only accounts for one half of it. The most plausible explanation for this reduction in the total $B(GT)$ is a reduction in the number of proton pairs as compared with the ^{144}Sm case. In reality, the problem of our deduction is that the number of scattered protons in the ground-state of ^{144}Sm can not be assumed to be valid for the nuclei above the ^{146}Gd core as well. Probably the 2.4 MeV gap which appears in ^{146}Gd between the $2d_{5/2}$ and the group of three free orbitals $2d_{3/2}$, $3s_{1/2}$ and $1h_{11/2}$ is smaller in the case of ^{144}Sm . This would explain why the occupation of the $h_{11/2}$ in the case of ^{148}Dy or ^{148}Tb is smaller than in the case of ^{144}Sm studied in [73].

We can turn the problem around and try to deduce the pair scattering from the comparison of the decays of ^{148}Dy and $^{148}\text{Tb } 2^-$. Assuming that the $B(GT)$ is directly proportional to the number of pairs in the $h_{11/2}$ orbital we can write:

$$\frac{B(GT)_{^{148}\text{Dy}}}{B(GT)_{^{148}\text{Tb } 2^-}} = \frac{0.67 + p}{p} \quad (11.1)$$

where in the second term we have “0.67”, which is the number of *real pairs* in the $h_{11/2}$ orbital in the ground-state of ^{148}Dy (one pair occupying the three orbitals $d_{3/2}$, $s_{1/2}$ and $h_{11/2}$ is 67% of the time in the $h_{11/2}$), and “ p ”, which is the number of *scattered pairs* that we want to calculate. We are neglecting the small blocking effect of the proton in the $d_{3/2}$ in $^{148}\text{Tb } 2^-$ which allows us to assume that the number of scattered proton pairs p is the same for ^{148}Dy and $^{148}\text{Tb } 2^-$. We can rewrite eq. 11.1:

$$p = 0.67 \times \left(\frac{B(GT)_{148Dy}}{B(GT)_{148Tb\ 2^-}} - 1 \right)^{-1} \quad (11.2)$$

And finally, using our results for the total $B(GT)$ measured for the decay of ^{146}Gd and $^{148}\text{Tb}\ 2^-$ we obtain that the number of proton pairs scattered from the ^{146}Gd core is:

$$p = 0.15(3)$$

to be compared with the same number for ^{144}Sm which is 0.80(15) according to [73]. This comparison indicates that for some reason (probably a reduction in the gap in ^{144}Sm) the scattering of proton pairs across the gap is much smaller (a factor of 5) in the nuclei above the ^{146}Gd core than in the nuclei below the core. This supports the idea of ^{146}Gd as a quasi-doubly magic nucleus.

In Sec. 8.2 we argued that the position of the Gamow-Teller resonance in the odd-odd rare-earth nuclei above ^{146}Gd should be around 4-5 MeV. In the decay of both isomers in ^{152}Tm our observation was in good agreement with that expectation, as well as in the case of ^{150}Ho [25]. However, in the decay of $^{148}\text{Tb}\ 2^-$ the $B(GT)$ is concentrated in the region from 4.5 MeV to 5.8 MeV where it is cut by the Q_{EC} . In other words, it seems to be shifted with respect to the resonances observed in ^{152}Tm and ^{150}Ho . The reason is simple: in this nucleus the proton pair which has to breakup to produce the decay is not present in the upper orbitals, it must be promoted from the core and this requires some extra energy.

A deeper discussion on the $B(GT)$ distribution of the decay of $^{148}\text{Tb}\ 2^-$ is left for Chap. 12. Now we will continue with the measurement and results of the high-spin isomer decay of ^{148}Tb . The reaction chosen for the production of this isomer was $^{94}\text{Zr}(^{58}\text{Ni},3\text{pn})^{148}\text{Tb}$. The half-lives involved in this measurement were: $T_{1/2}=198$ s, 60 min, 132 s and 74.6 y for ^{148}Dy , $^{148}\text{Tb}\ 2^-$, $^{148}\text{Tb}\ 9^+$ and ^{148}Gd respectively. This means that, regardless of the cycle we use, we can never get rid of the ^{148}Dy decay without losing much of the decay of interest. Apart from that, the decay of $^{148}\text{Tb}\ 2^-$ will be present in the spectra as well. In order to optimise for the measurement of the $^{148}\text{Tb}\ 9^+$ decay a symmetric cycle of 240 s was used. The EC spectrum of the β -decay of $^{148}\text{Tb}\ 9^+$ registered in the TAS detector is shown in the left panel of Fig. 11.4 (grey shade). The overlaid dashed line is the recalculated spectrum after the analysis process. The analysis was performed without removing either the pileup, the background or the undesired activities, but taking them into account at the level of the analysis as explained in Sec. 3.2. In the left part of the figure we see the final result for the $B(GT)$ distribution in the β -decay of $^{148}\text{Tb}\ 9^+$.

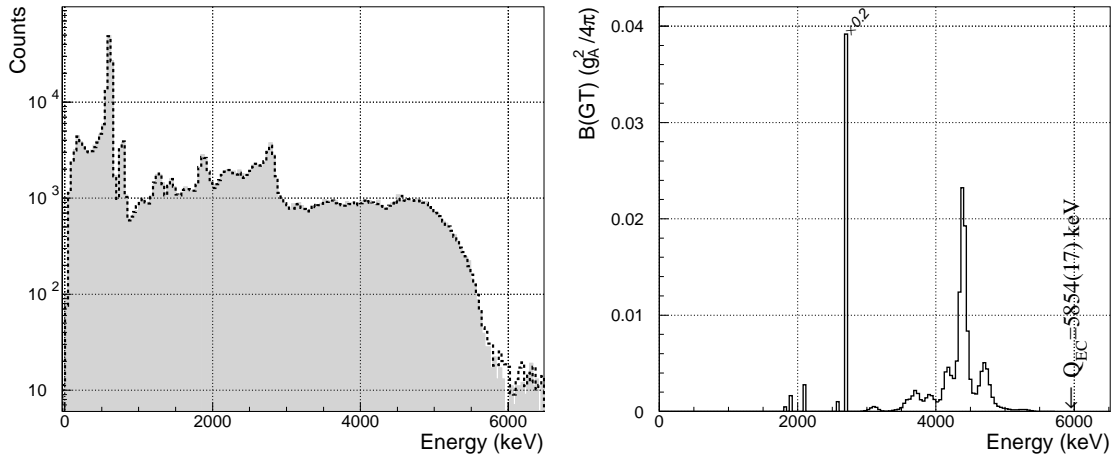


Figure 11.4: Same as in Fig. 11.2 for the decay of $^{148}\text{Tb } 9^+$.

Summing this $B(\text{GT})$ up to 5.8 MeV we obtain:

$$\boxed{\sum^{5.8\text{MeV}} B(\text{GT}) = 0.34(4) \frac{g_A^2}{4\pi}}$$

of which $0.20 \frac{g_A^2}{4\pi}$ is concentrated in the $2p$ state at 2694 keV and the remaining $0.14 \frac{g_A^2}{4\pi}$ is distributed 4 and 5 MeV. In this case we see clearly the two components of the decay: the odd proton decay which populates the $2p \ 8^+$ state in the daughter, and the pair breaking which populates the $4p$ states of the resonance. The resonance due to the pair breaking has the same amount of $B(\text{GT})$ than the low-spin isomer decay as one would expect. However the position of the resonance does not seem to be in agreement with our previous reasoning in the sense that this resonance is due to the decay of one proton of the pair coupled to 0^+ and therefore one still needs the extra energy to promote the proton pair from the core. In other words, we would expect to have the resonance around the same position as in the low-spin case. There is one possible explanation for this behaviour which will be discussed extensively in Chap. 12.

11.3 Beta decay of ^{156}Tm

So far we have dealt with parent nuclei with 82 or 83 neutrons and a number of protons above ^{146}Gd . The assumption underneath our previous and following discussions is that we are sufficiently close to the $N=82$ magic number to keep the characteristics of the spherical nuclei at least in the ground-state. In this section we will study the decay of a nucleus with 87 neutrons. We believe that five neutrons away from $N=82$ is enough to start to observe some change toward transitional nuclei. The question now is whether the β -decay can give us some insight into these changes. This can very well be since the first clear change that we observe is that

there is only one β -decaying isomer in ^{156}Tm .

A first measurement of the β -decay of ^{156}Tm using a total absorption spectrometer was carried out at the GSI On-line Mass Separator [74]. However, at that time the spectrometer used was not the same as the one described in Sec. 9.3 but a prototype of smaller size, the TAgS from the PNPI of St. Petersburg. [75]. It was made of NaI and it had a cylindrical shape with 20 cm high, 20 cm diameter and a hole of $\varnothing=4.3$ cm through the longitudinal axis. One side of the hole is closed by another NaI piece ($\varnothing=20$ cm, $h=10$ cm), and the other side by a BGO cylinder ($\varnothing=3$ cm, $h=3.3$ cm) inside the hole. Near the implantation point there was a Teflon piece to hold a Si detector used to measure the positrons. The overall efficiency of the PNPI TAgS was smaller than the TAS used in this work. Another difference between the old results of the ^{156}Tm decay [74] and the ones we are presenting here, is the analysis method. In Ref. [74] the authors used the *Peel-off* algorithm to unfold the data [76] instead of the EM algorithm that we are using here. Finally, one last difference between the analysis performed in [74] and ours is the calculation of the response function of the detector. In our simulation we have made a special treatment of the light production in the scintillator crystal which presents a linear dependence with the energy deposited in the crystal [23], and not a direct proportionality as was believed before. Of course this effect could not be taken into account in Ref. [74].

The measurement of the β -decay of ^{156}Tm was repeated with the TAS at the GSI On-line Mass Separator some years later. The fusion-evaporation reaction used was $^{103}\text{Rh}(^{58}\text{Ni},4\text{pn})^{156}\text{Tm}$ which populates directly the nucleus of interest. On the other hand, ^{156}Yb is also produced in the reaction through the αp channel, and ^{156}Yb decays by β^+ populating ^{156}Tm again. The half-lives involved in the production and decay of ^{156}Tm are: $T_{1/2}=26.1$ s, 83.8 s and 18.6 min for ^{156}Yb , ^{156}Tm and ^{156}Er respectively. The symmetric cycle used for this measurement was 120 s. Fig. 11.5 shows the results of the measurement and analysis of the β -decay of ^{156}Tm . As in the previous cases, the grey shade on the left side of the figure is the experimental EC spectrum measured in the TAS, and the overlaid dashed line is the recalculated spectrum after the analysis process. In the right part of the figure we see the final result for the B(GT) distribution of the same decay.

The sum of the B(GT) up to 7.2 MeV gives an amount of:

$$\boxed{\sum^{7.2\text{MeV}} B(GT) = 0.48(3) \frac{g_A^2}{4\pi}}$$

If we compare our results with those from Ref. [74] we see that, on one hand the total B(GT) is exactly the same ($\sum^{7.2\text{MeV}} B(GT)=0.48(5)g_A^2/4\pi$ in [74]), and, on the other hand, the B(GT) distributions present only two small differences: 1) Our resulting B(GT) shows some structure not seen in [74], probably due to the better efficiency and resolution of the detector, and 2) there is a small shift in the maximum of the resonance, being this ≈ 80 keV higher in [74]. This can be explained by the

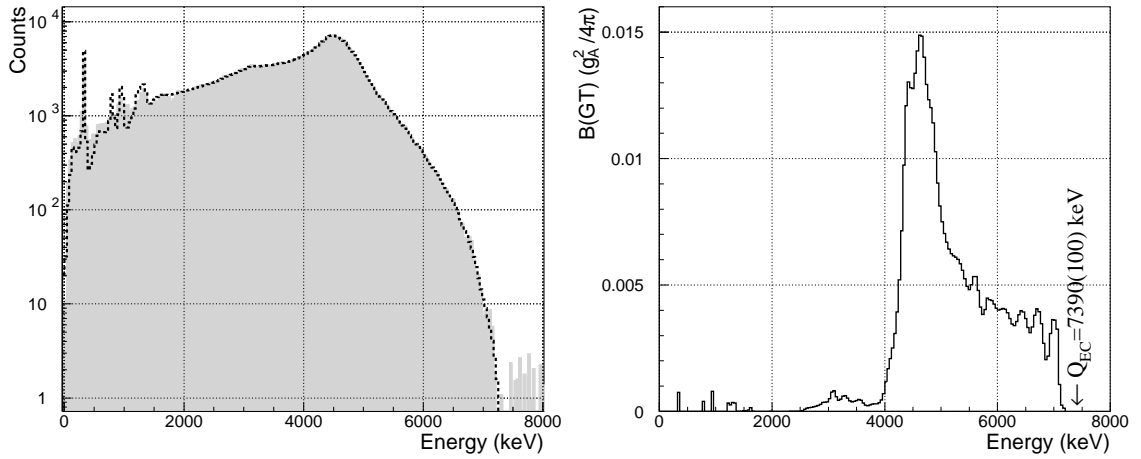


Figure 11.5: Same as in Fig. 11.2 for the decay of ^{156}Tm .

effect of the non-proportionality of the light production in the scintillator, already mentioned in this section. This non-proportionality implies that the total absorption photo-peak due to a γ cascade of multiplicity 2 is shifted about 20-30 keV with respect to the position of the direct sum of the energies of the two γ -rays. If the cascade has multiplicity 3 this shift will be of 40-60 keV. If one does not take this into account, and the resonance de-excites through γ cascades of multiplicity 3 on average, then the resulting $B(\text{GT})$ may well be shifted by 60 keV. This results and the comparison of the two measurements were reported in [77]. Any other consideration about the $B(\text{GT})$ distribution in the decay of ^{156}Tm and its contribution to the systematics in the region is postponed to the next chapter.

Chapter 12

Systematics of the GT resonance in the rare-earth region. Theoretical shell model calculations

12.1 Systematics of the GT resonance in the region

In this work we have studied, among other things, the β -decay of the odd- $N=83$ ^{152}Tm and ^{148}Tb . If we recall the results from Ref. [25] for the decay of ^{150}Ho , then we cover the systematics of the $\pi h_{11/2} \rightarrow \nu h_{9/2}$ decay in the region as we fill the $h_{11/2}$ orbital from 0 to 5 protons. In Fig. 12.1 we have plotted the resulting $B(\text{GT})$ distribution in the six cases of which we have a good determination of the $B(\text{GT})$ measured using the TAS technique. The left column corresponds always to the 2^- isomer and the right column to the 9^+ one. From the bottom we have first the decay of ^{148}Tb , which covers the cases with 0 and 1 proton in the $h_{11/2}$ and has been studied in this work (see Sec. 11.2), then we have the decay of ^{150}Ho , corresponding to the cases with 2 and 3 protons and studied in [25], and finally ^{152}Tm , covering the cases with 4 and 5 protons in the $h_{11/2}$ which has also been presented here (Chap. 10). The shade which appears at the right side of the graphs represents the region beyond the Q_{EC} which is therefore unavailable in the decay. The circles in the upper part of each graph are the number of protons in the $h_{11/2}$ orbital in the extreme single-particle picture. They have been separated into two different parts: proton pairs coupled to 0^+ , and the odd proton. The circles are placed on the graph so that the odd proton is above the 8^+ 2p state which is populated in its decay, and the proton pairs are above the broad distribution corresponding to the 4p states populated in the breakup of one proton pair. The amount of $B(\text{GT})$ to the 2p state or to the the resonance is indicated on the graph as well in units of $g_A^2/4\pi$.

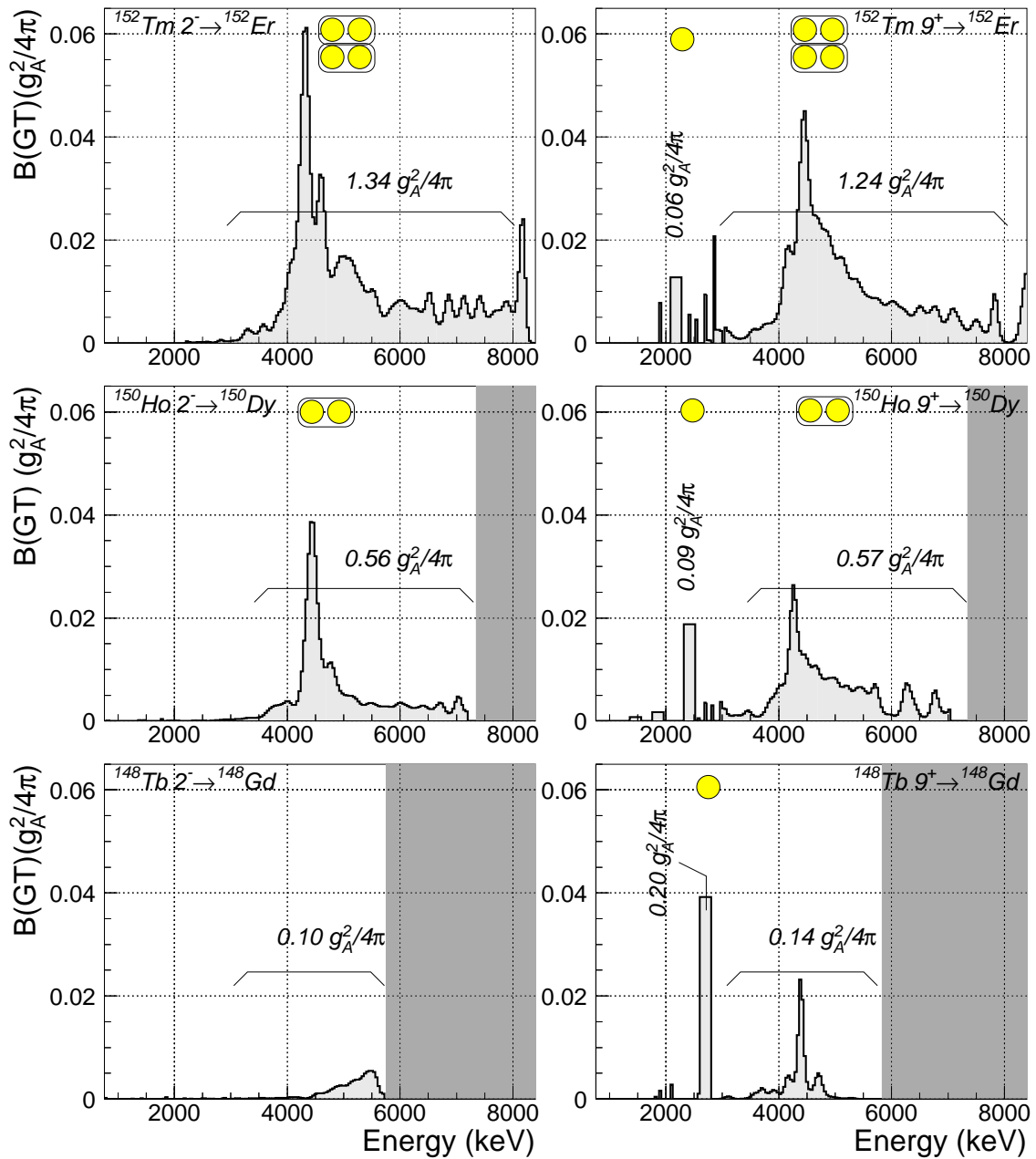


Figure 12.1: Gamow-Teller strength distribution in the β -decay of the odd- $N=83$ nuclei above ^{146}Gd pertinent to the present discussion (see text).

The first common feature in all the cases but $^{148}\text{Tb } 2^-$ is the relatively narrow resonance with its maximum at ≈ 4.5 MeV. The position of the resonance is in agreement with our first approximation of 4-5 MeV (see Sec. 8.2). The resonance in ^{148}Tb requires the promotion of proton pairs from the core and its position will be discussed later. The width of the resonance is mainly due to configuration mix-

ing and is not related to any half-life. In general, one can divide the width of a resonance into two different parts (besides the experimental resolution): spreading width and escaping width. The former is due to configuration mixing and the latter would correspond to the half-life of the state which can be very short if it decays emitting particles. In our case the Gamow-Teller state decays mainly by γ emission instead of particle emission, therefore the corresponding escaping width is negligible. In fact, the β -delayed α emission has been measured in the case of $^{150}\text{Ho } 2^-$ and $^{152}\text{Tm } 2^-$, however it represents a small contribution to the $B(\text{GT})$ compared to the γ emission and does not affect the half-life of the bound levels. The fact that the Gamow-Teller state is mixed with many other states of particle character (1p, 2p, 3p...) or particle-hole character (1p1h, 2p2h, 3p3h...) is what we regard as configuration mixing. In the figure we see a full width at half maximum (fwhm) of the order of 400-500 keV for the decay of $^{152}\text{Tm } 2^-$ and 250 keV for the decay of $^{150}\text{Ho } 2^-$. The corresponding high-spin cases seem to have part of the $B(\text{GT})$ of the resonance shifted to higher energy increasing the tail and beyond the main peak. In the case of ^{148}Tb we observe a bigger spread of the resonance in the decay of the 2^- isomer and an extremely narrow resonance in the high-spin case with a fwhm of 120-150 keV. We conclude that the spreading width, due to configuration mixing, grows rapidly with the number of particles in the final nucleus. This is because, as the number of particles increases, there are more possible combinations of particles to build complex configurations with the proper J^π which can mix, therefore some $B(\text{GT})$ goes to these states. This is the reason why the resonance becomes wider as the number of protons in the $h_{11/2}$ increases. This mixing is also responsible for the long tail beyond the peak which is cut by the Q_{EC} window in most of the cases. According to Ref. [16], this tail can reach ≈ 200 MeV carrying up to 50% of the total Gamow-Teller strength.

Let us now have a closer inspection to the $B(\text{GT})$ numbers as expressed in the figure. As the low-spin decay corresponds to the breakup of a proton pair populating 4p states in the daughter, in all the three nuclei the amount of $B(\text{GT})$ in the low-spin decay should be similar to the amount of $B(\text{GT})$ which goes to the 4p states of the resonance in the high-spin decay, as this corresponds also to the breakup of a proton pair. One can see that this is accomplished in the three cases within the uncertainty of the $B(\text{GT})$ value. On the other hand one would say, in the extreme single-particle approach, that the amount of $B(\text{GT})$ is directly proportional to the number of protons present in the $h_{11/2}$ orbital in the parent state. Then the total $B(\text{GT})$ measured in the low-spin decay of ^{152}Tm should be, in first approximation, twice the total $B(\text{GT})$ measured in the low-spin decay of ^{150}Ho . In reality we must take into account the proton pairs that are promoted from the ^{146}Gd core due to pairing correlations as well as the fraction of the proton pairs which are not in the $h_{11/2}$ orbital but in the other two orbitals $s_{1/2}$ and $d_{3/2}$, very close in energy to the $h_{11/2}$. Doing it properly requires a BCS calculation, including the $g_{7/2}$, $d_{5/2}$, $s_{1/2}$, $h_{11/2}$ and $d_{3/2}$, similar to the one performed for the $N=82$ nuclei above ^{146}Gd in [78].

Instead of using the results from [78] we have performed a shell-model calculation using a two-body interaction matrix whose elements have been estimated using empirical data [79]. All the non-diagonal matrix elements have been neglected except for those related to the pairing correlations, i.e. the three 0^+ two-body interactions which have been adjusted to reproduce the ^{148}Dy level scheme (See Sec. 12.2 for the details of the calculation). Looking at the wave functions obtained in the calculation we can estimate the number of protons in the $h_{11/2}$ orbital in each case. In $^{152}\text{Tm } 2^-$ this occupation is 3.04, in $^{150}\text{Ho } 2^-$ 1.52, and in ^{148}Dy 1.39, to be compared with the BCS calculation of [78] which gives 2.9, 1.7 and 1.7 for these occupations respectively. Using our results we conclude that the ratio between the total B(GT) in the decays of $^{152}\text{Tm } 2^-$ and $^{150}\text{Ho } 2^-$ should be $3.0/1.5=2.0$ (see Table 12.1). The numbers in the left panels of Fig. 12.1 for ^{152}Tm and ^{150}Ho agree with this expectation within the uncertainties in the B(GT) values as the ratio of B(GT) values for $^{152}\text{Tm } 2^-$ and $^{150}\text{Ho } 2^-$ is 2.3(4). Furthermore, as the decay of $^{150}\text{Ho } 2^-$ is due to the breakup of one pair, the total B(GT) should be very similar (in reality $1.52/1.39=1.1$) to the total B(GT) in the decay of ^{148}Dy . Recalling the results of Sec. 11.1, $B(\text{GT})_{^{148}\text{Dy}}=0.55(1) g_A^2/4\pi$, we see that this is correct. Finally, in the ^{148}Tb case we can not calculate the occupation of the $h_{11/2}$ because we need to use a different core, ^{144}Sm (See Sec. 12.2). However, we can assume that we have 0.15(3) proton pairs in the $h_{11/2}$ as this was the result obtained in Sec. 11.2, and therefore the ratio of total B(GT) values in the decay of $^{150}\text{Ho } 2^-$ and $^{148}\text{Tb } 2^-$ should be $1.52/0.30(6)=5(1)$. The measured ratio is 5.6(4) which is also close to the expected value. As a conclusion, we agree that the assumption of the direct proportionality of the B(GT) with the number of protons in the $h_{11/2}$ is correct in the case of an even number of protons in this orbital (β -decay of the low-spin isomers and ^{148}Dy), since our results are quite consistent with this assumption. In Table 12.1 we present a summary of the expected (shell-model) and measured B(GT) ratios for the low-spin decays.

B(GT)	$^{152}\text{Tm } 2^- / ^{150}\text{Ho } 2^-$	$^{150}\text{Ho } 2^- / ^{148}\text{Tb } 2^-$	$^{150}\text{Ho } 2^- / ^{148}\text{Dy}$
Theoretical value	2.0	5(1)	1.1
Measured value	2.3(4)	5.6(4)	1.02(7)

Table 12.1: Ratio between B(GT) values: comparison between the expected value from a shell model calculation and the experimental results of this work. Only the experimental errors are taken into account.

Now we can try to do the same with the high-spin decays. First of all we can check whether the total B(GT) in the high-spin decay follows the same proportionality with the total B(GT) in the low-spin decay. The occupation of the $h_{11/2}$ in the high-spin isomers is, according to our shell-model calculation: 2.27 and 3.62 for $^{150}\text{Ho } 9^+$ and $^{152}\text{Tm } 9^+$ respectively. In $^{148}\text{Tb } 9^+$ we can assume that the number of protons in

the $h_{11/2}$ is the same as in $^{148}\text{Tb } 2^-$ (estimated in Sec. 11.2) plus one. Therefore, the ratio between the total B(GT) in the high-spin decay and the total B(GT) in the low-spin decay should be $1.30(6)/0.30(6)=4.3(9)$ for ^{148}Tb , $2.27/1.52=1.5$ for ^{150}Ho and $3.62/3.04=1.2$ for ^{152}Tm . In all the three cases the experimental ratio is in agreement with the expectation if we take into account the uncertainty: $3.4(5)$ for ^{148}Tb , $1.2(3)$ for ^{150}Ho and $1.0(3)$ for ^{152}Tm (see Table 12.2). On the other hand, the total B(GT) in the decay of the high-spin isomer of ^{152}Tm should be related to that of ^{150}Ho with a ratio 3.62 to 2.27 which is 1.6. This is in agreement with the experimental result for this ratio, which is $2.0(5)$. Finally, dividing the total B(GT) values for $^{150}\text{Ho } 9^+$ and $^{148}\text{Tb } 9^+$ we obtain $2.0(3)$ in good agreement with the ratio of the number of protons in the $h_{11/2}$: $2.27/1.30(6)=1.7(5)$. Tables 12.2 and 12.1 summarise these results.

B(GT)	$^{148}\text{Tb } 9^+ / ^{148}\text{Tb } 2^-$	$^{150}\text{Ho } 9^+ / ^{150}\text{Ho } 2^-$	$^{152}\text{Tm } 9^+ / ^{152}\text{Tm } 2^-$
Theoretical value	4.3(9)	1.5	1.2
Measured value	3.4(5)	1.2(3)	1.0(3)

Table 12.2: Same as Tab. 12.1

B(GT)	$^{152}\text{Tm } 9^+ / ^{150}\text{Ho } 9^+$	$^{150}\text{Ho } 9^+ / ^{148}\text{Tb } 9^+$
Theoretical value	1.6	1.7(5)
Measured value	2.0(5)	2.0(3)

Table 12.3: Same as Tab. 12.1

Following with the numbers of Fig. 12.1, we can now use the two different components of one particular high-spin decay. Again we will assume that the number of protons in the $h_{11/2}$ orbital in the ^{150}Ho and ^{152}Tm cases is the one given by our shell-model calculation. For the case of $^{152}\text{Tm } 9^+$ one would expect the ratio between the B(GT) to the resonance and the B(GT) to the $8^+ 2p$ state to be roughly $2.6/1=2.6$. Even in the case that our estimation for the occupation is not right, the ratio between both components of the decay should never exceed $4/1=4$. However, using the measured values for the B(GT) we obtain something bigger than 20 for this ratio. Similarly, in the case of $^{150}\text{Ho } 9^+$ decay the expected ratio would be 1.27, and never higher than 2, to be compared with the measured one 6.33. Finally, for the $^{148}\text{Tb } 9^+$ decay the calculation gives $0.30/1=0.30$ and the measurement 0.7. These differences are very big and outside any error bar, and they clearly increase as the number of protons in the $h_{11/2}$ orbital increases. Actually, this effect has been known for some years, but it was never observed as clearly as in the present case.

The fact that part of the B(GT), which in principle should be placed in the low energy state, is shifted to higher lying states is something well known and normally attributed to a residual repulsive interaction which mixes the pure states, shifts them apart, and redistributes the strength in such a way that it goes from the lower level to the upper one. One example of this sort of calculation can be seen in Ref. [80] in which the authors present some experimental results from the $^{48}\text{Ca}(^3\text{He,t})^{48}\text{Sc}$ reaction and then try to explain the distribution of the Gamow-Teller strength doing theoretical shell-model calculations. In a first approximation the strength should be shared among the two pure states, namely $\pi f_{7/2} \nu f_{7/2}^{-1}$ and $\pi f_{5/2} \nu f_{7/2}^{-1}$. As soon as one considers the mixing between both states using a certain particle-hole interaction extracted from [81] both states are pushed up, and the Gamow-Teller strength originally placed in the low lying state is reduced by a factor of three and moved to the upper state. The particle-hole interaction has a central component of the type $\sigma_1 \sigma_2 \tau_1 \tau_2$ and a tensor term $\tau_1 \tau_2$. In a further level of approximation the authors of [80] treat the mixing of the original 1p1h state with more complex configurations and this fractionates the upper state into many pieces leaving the lower one unaffected.

The dependence of this effect on the number of valence particles is mentioned in Ref. [82], where the authors find, for the $^{42}\text{Ca}(p,n)^{42}\text{Sc}$ reaction, that the strength is concentrated in the lower state and only a small fraction of it is spread at higher energy. However, as one adds neutrons to the system (e.g. the $^{48}\text{Ca}(^3\text{He,t})^{48}\text{Sc}$ reaction mentioned above) the Gamow-Teller strength moves up from the lower state to the higher states. The authors of [82] attribute this effect to the fact that the particle-particle matrix elements relevant for ^{42}Sc are attractive whereas the particle-hole matrix elements relevant for ^{48}Sc are repulsive. We have observed in our data that the Gamow-Teller strength moves up gradually from the lower state (the 8^+ 2p state) to the higher states (the 4p ones at ≈ 4.5 MeV) as the number of protons is increased which is exactly the same feature as found in Ref. [82] with the increase of the number of neutrons.

So far we have discussed the B(GT) total strength and distribution as we increase the number of protons. It is also interesting to see the effect of adding neutrons, and this will be discussed in the following. We will compare our results for the B(GT) distribution in the decay of two different isotopes of Tm. The decay of the low-spin isomer of ^{152}Tm is due to the breakup of one of the two proton pairs which may be occupying the $h_{11/2}$ orbital and the same picture should describe the decay of ^{156}Tm . However, the number of neutrons is very different for each case, and this is particularly important when we look at the states populated in the daughter nucleus. It is easy to imagine that the number of 2p, 3p... states that can be built combining six neutrons (^{156}Er) above the ^{146}Gd core is much bigger than the same number but combining only two neutrons (^{152}Er). This explains two things: the different shape of the B(GT) distribution and the different total B(GT) in the decay

of both isotopes. To discuss these differences let us have a look at Fig. 12.2 where the Gamow-Teller strength distribution in the decay of ^{156}Tm (top) and the same distribution in the decay of $^{152}\text{Tm } 2^-$ are presented. The most striking difference between both graphs is the ratio peak to tail which is 4.4 in the case of ^{156}Tm decay to be compared with 10.0 in the $^{152}\text{Tm } 2^-$ decay. But looking at the numbers there is another even more astonishing difference: the total $B(\text{GT})$ in the decay of ^{156}Tm amounts to less than 50% of the same quantity in the decay of $^{152}\text{Tm } 2^-$. Taking into account that both decays are due to the breakup of the pair in the $h_{11/2}$, and that the number of protons in this orbital in the parent nucleus is in principle the same for both decays, one would expect to observe the same amount of $B(\text{GT})$. Both effects: the smearing of the distribution and the reduction of the total $B(\text{GT})$ when the number of neutrons is increased, have the same origin, namely the configuration mixing. In the daughter nucleus ^{156}Er we have four extra neutrons with respect to ^{152}Er , therefore there must be a huge number of $2p, 3p \dots$ states with the appropriate spin and parity to mix with the pure Gamow-Teller state. This means that a big fraction of the $B(\text{GT})$ will be shifted up in energy, leaving the peak with less strength and moving it to the tail. Furthermore, the tail may very well extend up to very high energies not available in the β -decay window. Hence, we must have an important fraction of the $B(\text{GT})$ missing due to the Q_{EC} limitation. Calculations by Bertsch and Hamamoto [16] proved that, due to conventional nuclear mixing, up to 50% of the Gamow-Teller strength may very well shifted from the peak of the resonance to the continuum up to ≈ 200 MeV.

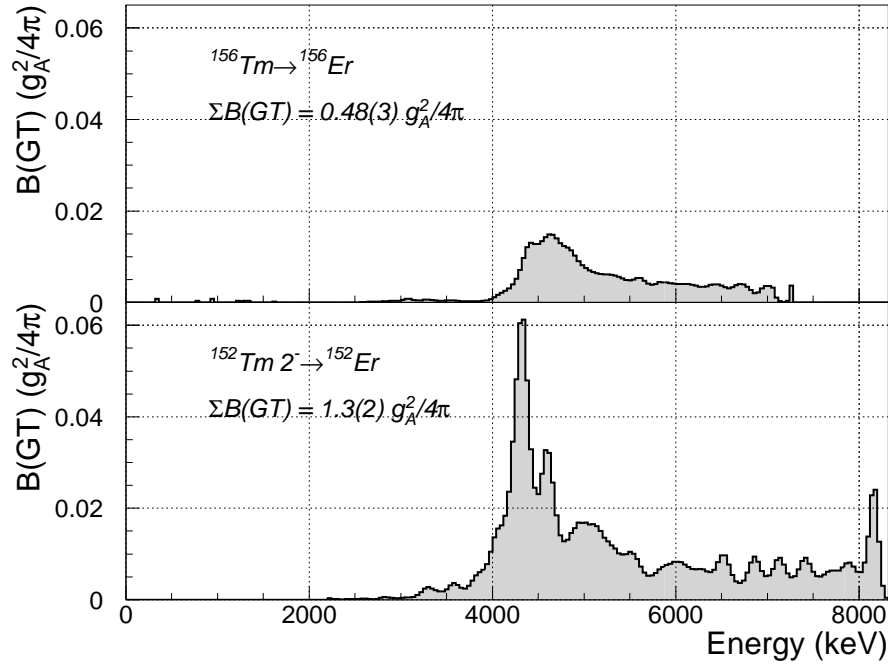


Figure 12.2: Gamow-Teller strength distribution in the decay of ^{156}Tm (top) compared to the same distribution in the decay of $^{152}\text{Tm } 2^-$ (bottom).

So far the discussion has been focused in the B(GT) distribution more than in the total B(GT) value. At this point one can compare the results obtained in this work for the total B(GT) with theoretical estimates for these particular nuclei. Such a calculation can be found in Ref. [78]. Detailed microscopic calculations do not exist in this region of the Segré table. In the following the calculations of Ref. [78] are summarised.

The starting point of this approach is the extreme single-particle approximation. For n protons in a certain orbital and the corresponding spin-orbit partner for neutrons completely empty, the Gamow-Teller strength in the extreme single-particle approximation would be:

$$B(\text{GT})_{\text{S.P.}} = n \frac{4\ell}{2\ell + 1} \quad (12.1)$$

However, this must be corrected by a factor h , the so called *hindrance factor*, to take into account various effects such as pairing correlations, core polarisation (one and two-body corrections), and higher order effects (e.g. Δ -hole excitations). In Ref. [78] the first two effects are theoretically calculated, but not the higher order effects. This last correction is simply assumed to be a factor $h_{\text{high}}=1.6$, the appropriate factor to explain that only 60% of the sum-rule is observed in (p,n) reactions (see Sec. 1.3). Once we have the hindrance factor h , the single-particle calculation and the experimental B(GT) should verify:

$$B(\text{GT})_{\text{S.P.}} = B(\text{GT})_{\text{EXP}} \times h \quad (12.2)$$

We can now use Eq. (12.1) to calculate the total B(GT) for some of the decays studied in this work in the extreme single-particle approximation and correct it with the hindrance factors calculated in [78]. It is worth noting here that the calculations of [78] refer to $N=82$ and we will compare them with our results for $N=83$ nuclei. In this we assume that the valence neutron in the parent state is in the $f_{7/2}$ orbital which does not take part in the decay and consequently does not affect the B(GT). The comparison of the expected values for the total B(GT) using [78] and our measurements is shown in Fig. 12.3. In the x axis of the graph there is the number of protons in the $h_{11/2}$ proton orbital neglecting pair correlations, and in the y axis the total B(GT). The black vertical bars represent the points calculated using [78]. The lengths of the bars represent the range of possible B(GT) values depending on the choice of the effective interaction in the evaluation of the core polarisation in [78]. The grey squares with error bars are the values measured for the total B(GT) using the total absorption technique. The points corresponding to the decay of both isomers of ^{150}Ho have been taken from [25], and the rest of them are some of the results of this work. Although the experimental points follow a similar trend to the theoretical bars, there is a systematic reduction of the measured B(GT). As we defend the idea that we measure all the B(GT) which lies inside the Q_{EC} window, this discrepancy can be due to the fact that the calculation is performed

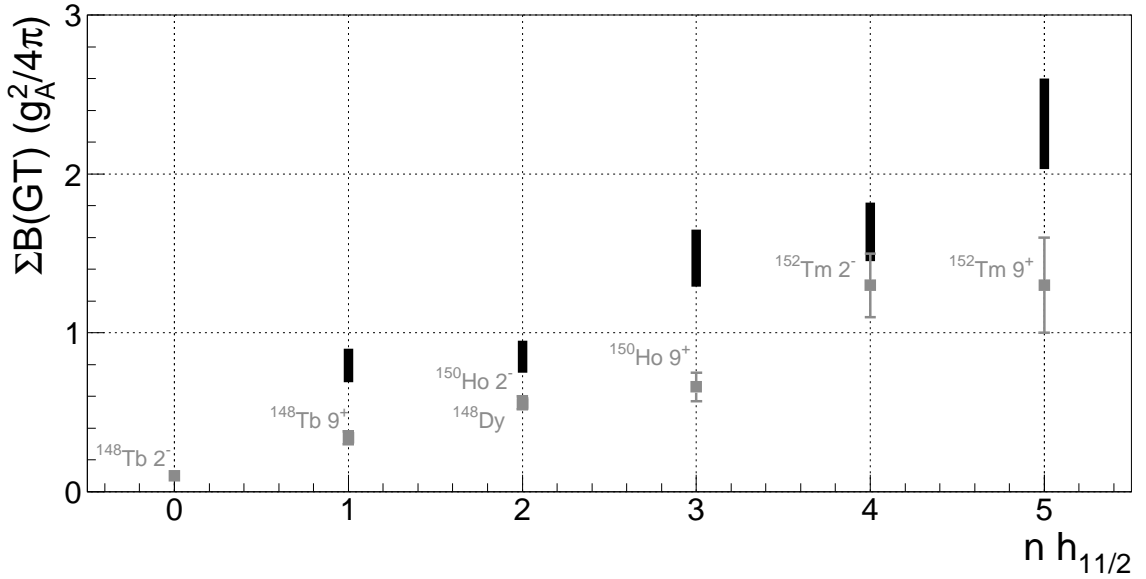


Figure 12.3: Evolution of the total B(GT) as a function of the occupancy number of the proton orbital $h_{11/2}$. The results from this work (grey squares) are compared with the theoretical estimates of Ref. [78] (black bars).

using a very limited configuration space in the sense that the author only takes into account the overlap between the $\pi h_{11/2}$ and the $\nu h_{9/2}$. The only sources of quenching are then the pairing correlations, the core polarisation and the higher order effects, but the mixing of the original configuration with many other 1p, 2p, 1p1h, 2p2h... configurations is not taken into account, as well as the fact that the strength might be shifted to higher energies and lie beyond the Q_{EC} window, which again is not part of the calculation.

12.2 Shell model calculations

Apart from the estimates shown in the previous section for the total B(GT), we have performed a shell model calculation using the OXBASH code [83]. For that we followed the method explained in Ref. [20] in which the authors construct the two-body interaction matrix based on empirical data and, using this phenomenological interaction and the shell-model approach, they can reproduce very well the energy of the Gamow-Teller resonance in the decay of ¹⁵⁰Ho 2⁻. Using the same approach, originally developed by Prof. J. Blomqvist in [79], and with the help of [84], we constructed a two-body interaction matrix for the calculation of the states in ¹⁴⁸Gd which are populated in the β -decay of ¹⁴⁸Tb. These states are, in the low-spin case, 4p states with the configuration $[\pi d_{3/2} \pi h_{11/2} \nu f_{7/2} \nu h_{9/2}]_{1-, 2-, 3-}$. In the high-spin case the configurations will be, the 4p states populated in the breakup of a proton pair: $[\pi h_{11/2} \pi h_{11/2} \nu f_{7/2} \nu h_{9/2}]_{8+, 9+, 10+}$, and the 2p state populated in the decay of the odd proton: $[\pi h_{11/2}^2]_{0+} [\nu f_{7/2} \nu h_{9/2}]_{8+}$. The nucleus which acts as a core for this shell-model

calculation is ^{144}Sm . This means that the values for the single-particle excitations and for the residual two-body interaction are taken from experimental data relative to this core. In order to perform the calculation we have used a configuration space which includes the orbitals $2d_{3/2}$, $3s_{1/2}$ and $1h_{11/2}$ on the proton side, and $2f_{7/2}$ and $1h_{9/2}$ on the neutron side. We neglected all the non-diagonal terms of the interaction matrix except the ones related to the pairing correlations of the protons which are $\langle \pi s_{1/2}^2 | V | \pi d_{3/2}^2 \rangle_{0+}$, $\langle \pi s_{1/2}^2 | V | \pi h_{11/2}^2 \rangle_{0+}$ and $\langle \pi d_{3/2}^2 | V | \pi h_{11/2}^2 \rangle_{0+}$. These three, and the three diagonal terms $\langle \pi s_{1/2}^2 | V | \pi s_{1/2}^2 \rangle_{0+}$, $\langle \pi d_{3/2}^2 | V | \pi d_{3/2}^2 \rangle_{0+}$ and $\langle \pi h_{11/2}^2 | V | \pi h_{11/2}^2 \rangle_{0+}$ have been adjusted to reproduce the ^{148}Dy level scheme.

Once we know the single-particle energies and the two-body interaction matrix is constructed, one can run the OXBASH code to calculate the wave function and energy of the states in the daughter nucleus. For the decay of $^{148}\text{Tb } 2^-$ we only needed to calculate the 1^- , 2^- and 3^- states in ^{148}Gd . In the next step one calculates the wave function of the parent state, and then one can run the code to obtain the overlap between the wave function of the parent ground-state, when the $\sigma\tau$ operator is applied, and the wave function of the daughter nucleus states. In this way one can obtain the probability amplitudes for the Gamow-Teller process which is the B(GT). The same sort of calculation was done in [20] for $^{150}\text{Ho } 2^-$ except that in that case the valence particles are referred to the ^{146}Gd core instead of ^{144}Sm . However, when we estimated the two-body matrix elements for the calculation of the $^{148}\text{Tb } 2^-$ decay we observed that they were very similar to those of Ref. [20] for the case of $^{150}\text{Ho } 2^-$. Encouraged by this observation we took some advantage of that work and we used the same matrix elements which appear there to calculate the $^{152}\text{Tm } 2^-$ decay, where the experimental data needed to extract these matrix elements are very scarce since we are further away from stability in this case. On the other hand, for the calculation of the $^{152}\text{Tm } 2^-$ decay we had to add one extra proton pair with respect to the $^{150}\text{Ho } 2^-$ case. Furthermore, we repeated the calculation of [20] for the $^{150}\text{Ho } 2^-$ decay.

The results of our shell-model calculation for the low-spin isomeric decays are presented in Fig. 12.4. A Gaussian distribution (fwhm \approx 165 keV) has been folded with the direct results from the OXBASH code in order to simulate the width of the resonance. The normalisation of the total area of the shell-model results is completely arbitrary, it has been chosen to give the same height for the measured and the calculated resonance. We can see that even with a very restricted phase-space calculation we can reproduce the position of the measured Gamow-Teller resonance within less than half MeV in the worst case (the upper one).

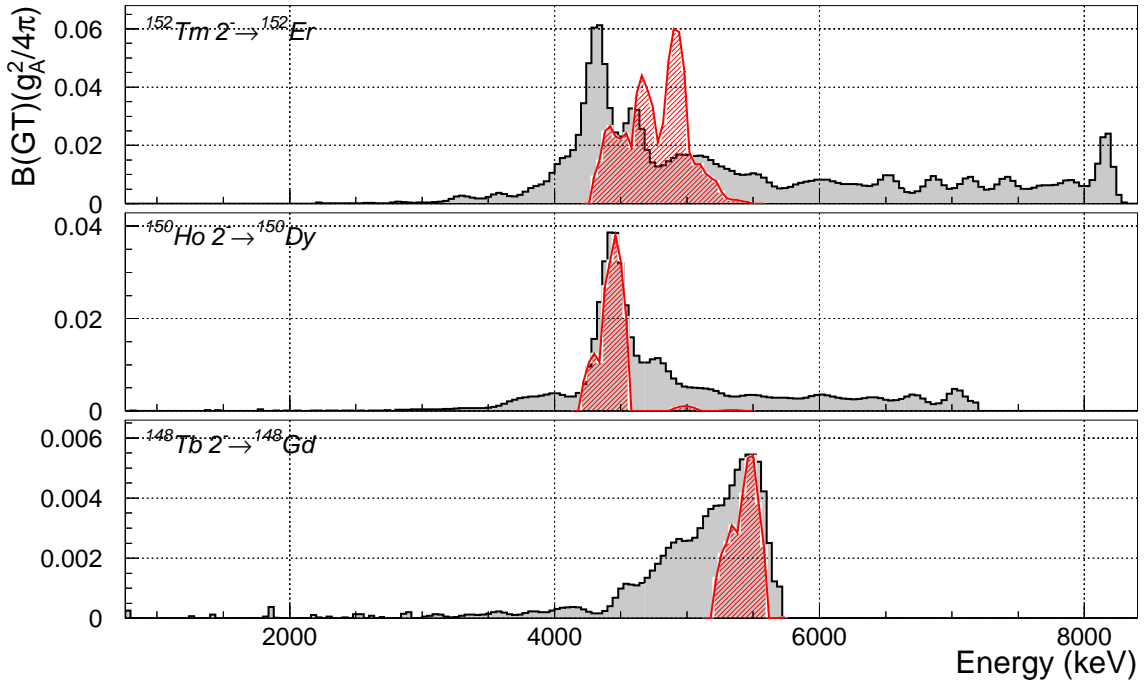


Figure 12.4: Gamow-Teller strength distribution for the low-spin isomer of the odd- $N=83$ nuclei above ^{146}Gd . The results from the TAS measurement (black/grey) are compared with a shell-model calculation (red).

In order to calculate the high-spin cases we proceeded in the same way: we took the two-body interaction matrix elements from [20] and, using ^{146}Gd as a core, we calculated the 8^+ , 9^+ and 10^+ states in the daughter nuclei ^{152}Er and ^{150}Dy . Afterwards we calculated the wave functions of $^{152}\text{Tm } 9^+$ and $^{150}\text{Ho } 9^+$, and then we ran the code again to obtain the Gamow-Teller amplitudes. After that we used the two-body interaction matrix that we calculated for the $^{148}\text{Tb } 2^-$ case and we took ^{144}Sm as the core to perform again the same calculation but for the decay of $^{148}\text{Tb } 9^+$. The results of these calculations for the high-spin isomeric decays are presented in Fig. 12.5. Once we observe the three shell-model results (red spectra in the figure) the first thing to note is that the strength actually moves from the lower state to the upper ones as we add protons to the $h_{11/2}$ orbital. This is the effect we mentioned in the previous section in reference to our results and to the results from [82]. Apart from that, the agreement between theory and experiment is not as good as in the low-spin cases. For the case of $^{152}\text{Tm } 9^+$ and $^{150}\text{Ho } 9^+$ decays it is still acceptable in terms of the position of the centroid of the resonance, however the calculated distribution presents a splitting that we do not observe experimentally, especially in the case of $^{150}\text{Ho } 9^+$ decay.

The case which presents the worst theory-experiment agreement is the decay of $^{148}\text{Tb } 9^+$ in which the centroid of the theoretical distribution is shifted by almost

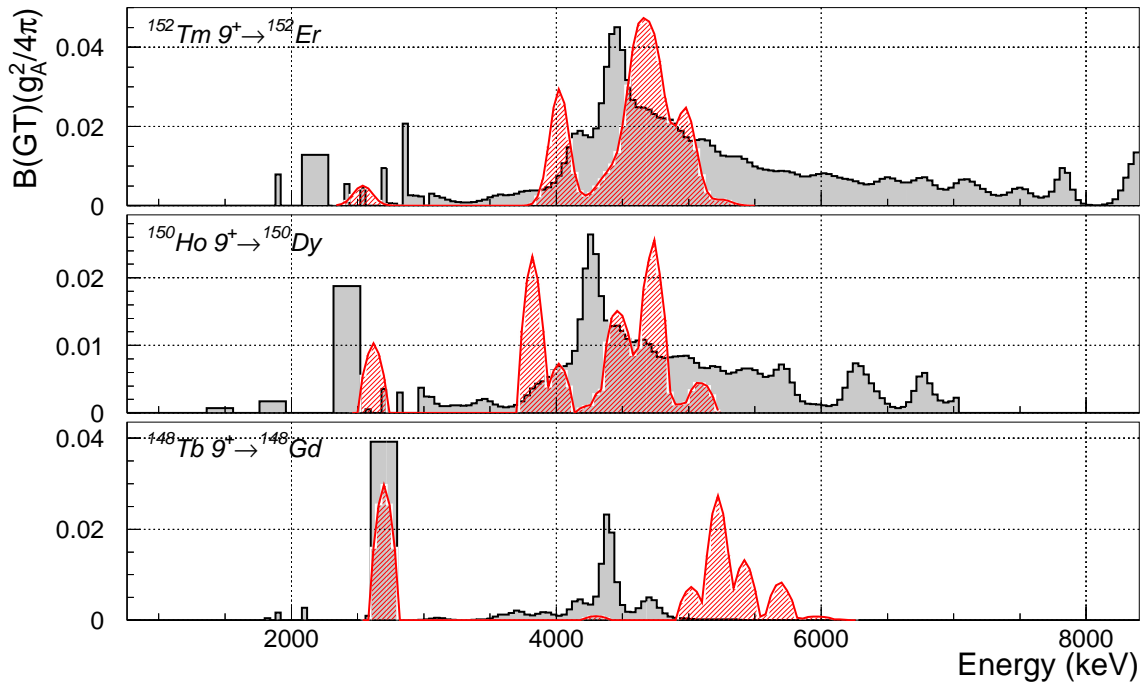


Figure 12.5: Same as Fig. 12.4 but for the high-spin isomers.

1 MeV with respect to the measured one. Actually, in different sections we have made clear that the $B(GT)$ distribution in the decay of ^{148}Tb should be shifted with respect to the same distribution in the other decays of the odd- $N=83$ nuclei above ^{146}Gd because one proton pair must be promoted from the core only in the case of ^{148}Tb and this requires some extra energy. In fact, the shell-model calculation reproduces very well the position of the resonance in the decay of the low-spin isomer of ^{148}Tb (see Fig. 12.4). However the decay of the high-spin isomer does not present the same distribution shifted with respect to the other decays and it is difficult to imagine why in this case the breakup of a proton pair promoted from the core should be different from the same breakup of a proton pair in the low-spin case.

There is one possible explanation for the difference between the decay of both isomers of ^{148}Tb and for the disagreement with the shell-model calculation. The 4p states populated in the decay of the high-spin isomer should have a wave function dominated by the configuration: $[\pi h_{11/2} \pi h_{11/2} \nu f_{7/2} \nu h_{9/2}]_{8^+, 9^+, 10^+}$. With this configuration one can build the final spin by coupling the two neutrons to 8^+ (as in the 2p state populated in the decay of the odd proton) and then the two protons can be coupled to $0^+, 2^+, \dots$. The coupling of these two protons with the neutrons can build the $8^+, 9^+$ and 10^+ states populated in the decay. The 8^+ state will be strongly mixed with the low-lying 2p state and therefore will receive more $B(GT)$ than the 9^+ and 10^+ states. The lowest 8^+ 4p state is the one with the two protons coupled

to 0^+ , then there is a second 8^+ with the two protons coupled to 2^+ , and the 9^+ and 10^+ also with the protons coupled to 2^+ . All these states are, according to the shell-model calculation, between 5 and 5.5 MeV in ^{148}Gd . However, according to the calculation, the 8^+ populated in the decay is not the lowest but the second one in energy, which is the one with the two protons coupled to 2^+ . Therefore most of the 4p states populated in the decay have the two protons coupled to 2^+ . These states might preferably mix with other states of the configuration $2_1^+ \otimes [\nu f_{7/2} \nu h_{9/2}]_{8^+, 9^+, 10^+}$, where 2_1^+ represents now the first 2^+ state in the ^{146}Gd core, namely the state at 1972 keV of particle-hole character $[\pi d_{5/2}^{-1} \pi s_{1/2}]_{2^+}$ [85]. In a first order approximation these states should lie 1972 keV higher in energy than the first 8^+ state of ^{148}Tb $[\nu f_{7/2} \nu h_{9/2}]_8^+$ which lies at 2694 keV, i.e., at approximately 4670 keV, very close to the observed states populated in the decay. In our shell-model calculation we use ^{144}Sm as a core and then the configuration space we are using does not include the $d_{5/2}$ orbital necessary to calculate states which include the configuration $[\pi d_{5/2}^{-1} \pi s_{1/2}]_{2^+}$ in their wave function. This is the reason why we can not reproduce the experimental data with our calculation. Doing the proper calculation would mean taking ^{140}Ce as a core and extending the configuration space to include the $d_{5/2}$ orbital in the two-body interaction. This is in principle possible, but then the OXBASH shell-model calculation of the states in ^{148}Gd would contain six protons distributed among the four proton orbitals and two neutrons to be shared by two neutron orbitals, which exceeds the present computing capabilities.

12.3 Summary and conclusion

In this third part of the work we have studied the Gamow-Teller resonance in the rare-earth region populated in the β -decay process. The experiments have been performed at the On-line Mass Separator at GSI using a total absorption spectrometer. The main results and conclusions which arise from this work are summarised in the following points:

1. We have measured the Gamow-Teller β -decay of the the two isomers of the odd-N=83 nuclei ^{152}Tm and ^{148}Tb . The β -decay of ^{148}Dy and ^{156}Tm has also been studied. For all these cases we have obtained the B(GT) distribution which presents a strong resonance inside the Q_{EC} window. The case of ^{148}Dy is the only one in which almost all the Gamow-Teller strength is concentrated in one single state. For this reason this is the only case in which our results agree quite well with previous experiments performed with high-resolution Ge detectors.
2. Combining the results for the decay of $^{148}\text{Tb } 2^-$ and ^{148}Dy we could estimate the occupation of the $h_{11/2}$ in the ground-state of these nuclei which turns out to be 0.15(3). This number is about five times smaller than the same occupation number in the case of ^{144}Sm which supports the idea of ^{146}Gd being a doubly closed shell nucleus.
3. With the results obtained here for ^{152}Tm and ^{148}Tb , and taking the results of Ref. [25] for ^{150}Ho we could study the systematics of the Gamow-Teller resonance as the number of protons in the $h_{11/2}$ increases. In all the cases but $^{148}\text{Tb } 2^-$ the Gamow-Teller resonance lies at an energy about 4.5 MeV. In the four decays in which there are proton pairs present in the $h_{11/2}$ orbital there is a very long tail which extends to the Q_{EC} . In the three high-spin decays there are two components of the decay: the decay of the odd proton populates a single 2p state lying at low energy, and the breakup of a proton pair populates the 4p states which form the resonance mentioned before. In all the cases the ratio of the B(GT) going to the resonance and going to the lower state is very large as compared to the extreme single-particle picture. Furthermore the effect is accentuated as we add protons to the $h_{11/2}$ of the parent. This effect has been explained as coming from nuclear configuration mixing and it is very similar to what is observed in charge-exchange reactions and discussed in Ref. [16].
4. By comparing our results for the decay of $^{152}\text{Tm } 2^-$ with those for the decay of ^{156}Tm we observed two effects as we add neutrons to the system: one is the smearing of the distribution, and the other the large suppression of the total B(GT). Both effects can be explained again if we consider that the number of 1p, 2p, 3p... states that we can build increases as we add valence particles. Therefore the configuration mixing is again the the reason why a big fraction

of the strength moves to many states near and beyond the peak, smearing in this way the distribution and contributing to the missing part of the strength in the tail beyond the Q_{EC} window. Again this is something already calculated for other cases in [16].

5. Using the hindrance factors of Ref. [78] we could calculate a theoretical estimation of the total $B(GT)$ that we should observe. Both the experimental data and the theoretical values follow a similar trend. However, there is a systematic reduction of the experimental $B(GT)$ which can arise from the fact that the calculations of [78] are carried out in a very limited configuration space.
6. Shell-model calculations have been performed using the OXBASH code [83] and a phenomenological two-body interaction. The $B(GT)$ distribution in the decay of the low-spin cases is well reproduced by the theoretical calculation. In the high-spin decay of ^{152}Tm and ^{150}Ho the agreement between theory and experiment is good in terms of the centroid of the resonance, but the calculated distributions present a splitting not observed in the experiment. The effect of the $B(GT)$ moving from the lower to the higher states, and its accentuation when we add protons, are also reasonably well reproduced by the calculations. However the position of the Gamow-Teller resonance in the $^{148}\text{Tb } 9^+$ does not appear in the right position. We can explain this disagreement as arising from the fact that we use a very limited configuration space which does not include the $d_{5/2}$ orbital.

Part IV

Resumen en español

Introducción

La desintegración β es un proceso en el que un neutrón se transforma en protón o viceversa. Puede darse de dos modos diferentes: Fermi o Gamow-Teller. El modo Fermi de desintegración viene mediado por el operador de aumento o disminución de isospin: $O_F = \tau^\pm$. El modo Gamow-Teller tiene además la posibilidad de cambiar el spin nuclear puesto que incluye el operador de Pauli: $O_{GT} = \sigma\tau^\pm$. Sin embargo, la desintegración beta no es el único proceso mediado por estos operadores. En las reacciones (n,p) y (p,n) también se transforma un neutrón en protón o viceversa, por ello son reacciones que vienen mediadas por los mismos operadores que la desintegración beta. Resumiendo, podemos extraer información de las propiedades de spin-isospin del núcleo estudiando su desintegración β Gamow-Teller o haciendo reacciones (n,p) y (p,n). Tanto para el caso de la desintegración beta como para las reacciones (n,p) y (p,n) tiene sentido definir una función, la función “Gamow-Teller strength”, que viene dada por:

$$B(GT) = | \langle \psi_f | \sum_{k=1}^A \sigma_k \tau_k^\pm | \psi_i \rangle |^2 \equiv \langle \sigma\tau \rangle^2 \quad (12.3)$$

Esta función no es más que el elemento de matriz al cuadrado del operador O_{GT} entre el estado inicial, estado fundamental o isómero en el núcleo padre, y los diferentes estados finales en el núcleo hijo. Por ello la $B(GT)$ debe estar directamente relacionada con la probabilidad de transición beta entre estos estados, o con la sección eficaz (p,n) o (n,p) según el caso.

Del estudio sistemático de las reacciones (p,n) sobre diferentes blancos se obtiene el resultado que se muestra en la Fig. 12.6, extraída de la Ref. [7]. En esta figura se representa la sección eficaz de la reacción (p,n) sobre distintos blancos, y en ella se observa una estructura de resonancia a una energía de excitación del núcleo de unos 20 MeV, la llamada resonancia de Gamow-teller. Esta resonancia que se había predicho en los años 60 [5], se descubrió en Michigan alrededor de 1975 [6] y fue estudiada en profundidad en los 80 [7][2]. Una interpretación semiclásica de esta resonancia es que se debe a un estado muy colectivo en el que se produce una oscilación en la cual protones de un cierto espín están siempre acoplados a neutrones del espín contrario. En un sistema cuántico como el núcleo esta interpretación semiclásica no describe exactamente la realidad.

Tomemos ahora la Ec. (12.3) y sumemos para todos los estados finales posibles. Esto equivaldría a integrar uno de los espectros mostrados en la Fig. [12.6]. Si esto se hace para una reacción (p,n), para la correspondiente (n,p), y se restan, queda la denominada regla de suma de Ikeda [8]:

$$S_{GT} = \sum_f B_-(GT) - \sum_f B_+(GT) = 3(N - Z) \quad (12.4)$$

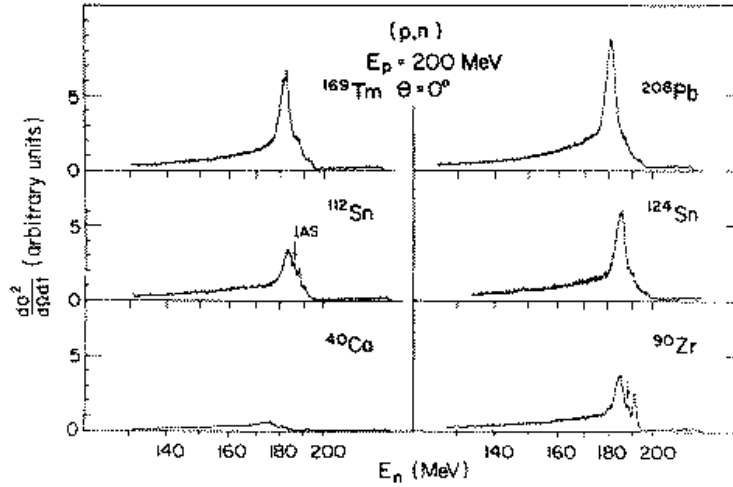


Figure 12.6: Espectro de tiempo de vuelo de los neutrones a $\theta = 0^\circ$ para la reacción (p,n) sobre distintos blancos nucleares (Ref. [7]).

Esta regla de suma es independiente del modelo, sólo depende del exceso de neutrones en el núcleo. Cuando se intenta reproducir esta regla de la suma experimentalmente uno encuentra que sólo se mide un 60% de la strength total que cabría esperar. Esto se ha denominado problema de la “missing strength” o “Gamow-Teller quenching”. Para explicar esta pérdida de B(GT) en los experimentos de reacciones se propusieron varios mecanismos. Uno era la renormalización de la constante axial debida al acoplamiento de excitaciones $\Delta(1232)$ -h al proceso [11][12][13]. El otro era la mezcla de configuraciones nucleares [14][15][16] que movería una buena parte de la B(GT) hacia altas energías. Para poder establecer cual de los dos mecanismos es dominante en los procesos Gamow-Teller se debe medir la resonancia estimando el fondo con mucha precisión. Esto se pudo hacer en 1997 [17][18], y parece ser que es el segundo mecanismo, la mezcla de configuraciones, el que explica las observaciones experimentales.

En cualquier caso, como proceso de desintegración β viene mediado por el mismo operador que las reacciones (p,n) o (n,p), debemos poder poblar la resonancia Gamow-Teller mediante desintegración β . Sin embargo la desintegración β es un proceso prohibido en general, en una buena parte de los casos debido a las restricciones impuestas por la ventana energética accesible en la desintegración. Sin embargo, existen tres regiones de la tabla nuclear en las cuales la mayor parte de la B(GT) cae dentro de la ventana accesible al proceso de desintegración β . En este trabajo se pretende estudiar la desintegración β Gamow-Teller en dos de esas regiones: Los núcleos con $N \approx Z$ y $A=70-80$, y los núcleos justo por encima del casi doblemente mágico ^{146}Gd . En cada caso el problema y el interés físico a estudiar son distintos y se explicarán en la sección correspondiente.

Teniendo claro lo que queremos estudiar, se plantea ahora cuál es la forma óptima de hacerlo. Como los estados poblados en la desintegración β suelen desexcitarse emitiendo radiación γ , tradicionalmente se han usado detectores de germanio para estudiar este tipo de desintegraciones. Estos detectores tienen muy buena resolución energética, pero la eficiencia de detección es muy baja. Nosotros pretendemos medir la probabilidad de desintegración β a los distintos niveles del núcleo hijo, es decir, la intensidad beta (I_β) en función de la energía de excitación del núcleo hijo, ya que de ésta se puede deducir fácilmente la $B(GT)$:

$$B(GT)(E) = 6147(7) \times \left(\frac{g_V}{g_A} \right)^2 \frac{I_\beta(E)}{f(Q_\beta - E) T_{1/2}} \quad (12.5)$$

Sin embargo, la baja eficiencia de los detectores de Ge para rayos γ de alta energía hace que no sean el instrumento más adecuado para este tipo de estudio, especialmente cuando nos alejamos de la estabilidad y los valores Q_β son muy grandes. Esta baja eficiencia, combinada con el hecho de que la $B(GT)$ suele estar muy fragmentada a altas energías (alta densidad de niveles) y que el núcleo hijo se desexcita siguiendo muchos caminos distintos cada vez, hace necesario el uso de un instrumento más eficiente que los detectores de Ge que detecte cascadas γ completas en lugar de fotones individuales. Este instrumento es un Espectrómetro de Absorción Total (TAS). El uso de un TAS para la medida precisa de la $B(GT)$ en la desintegración β nuclear se remonta a la Ref. [22]. Sobre el funcionamiento de este tipo de detector y el análisis de los datos obtenidos con un TAS se puede encontrar información en [25]. En la Fig. 12.7 se representa un TAS ideal. Se aprecia que de la detección de la cascada completa se puede extraer la intensidad beta I_β que nos permitirá finalmente llegar a la $B(GT)$. Un TAS real dista mucho de lo representado en la figura, pero la idea básica es exactamente esa.

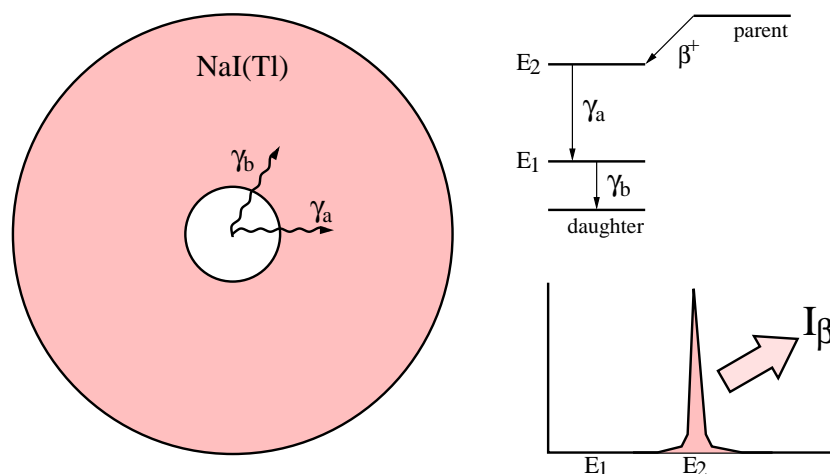


Figure 12.7: TAS en el caso ideal: Los dos rayos γ que aparecen tras la desintegración β son totalmente absorbidos por el detector. Del espectro se puede obtener directamente la intensidad beta I_β .

Los núcleos con $N \approx Z$ y $A=70-80$.

Los núcleos ricos en protones y con $A=70-80$ son los más pesados que uno puede estudiar en los cuales protones y neutrones ocupan los mismos orbitales ($N \approx Z$). Esta región se caracteriza por numerosos efectos asociados a deformación nuclear, por ejemplo transiciones de forma, coexistencia de forma, grandes deformaciones en el estado fundamental. . . Entre ellos, el ^{76}Sr es uno de los que mayor deformación debe mostrar en su estado fundamental [31]. Sin embargo, medir el signo de la deformación, es decir, si el núcleo en su estado fundamental es oblatado o prolado, es algo muy complicado.

Según Hamamoto y colaboradores [32] uno puede obtener información de la deformación nuclear a través de la desintegración β . Esta idea fue seguida en [33] donde cálculos teóricos RPA muestran que la forma de la distribución de la $B(\text{GT})$ en la desintegración β de ciertos núcleos depende fuertemente de su deformación. En el caso particular de los isótopos ligeros de Sr se observa una diferencia muy marcada en la $B(\text{GT})$ según la forma del núcleo padre como se puede apreciar en la Fig. 12.8 en la que se muestran estos cálculos.

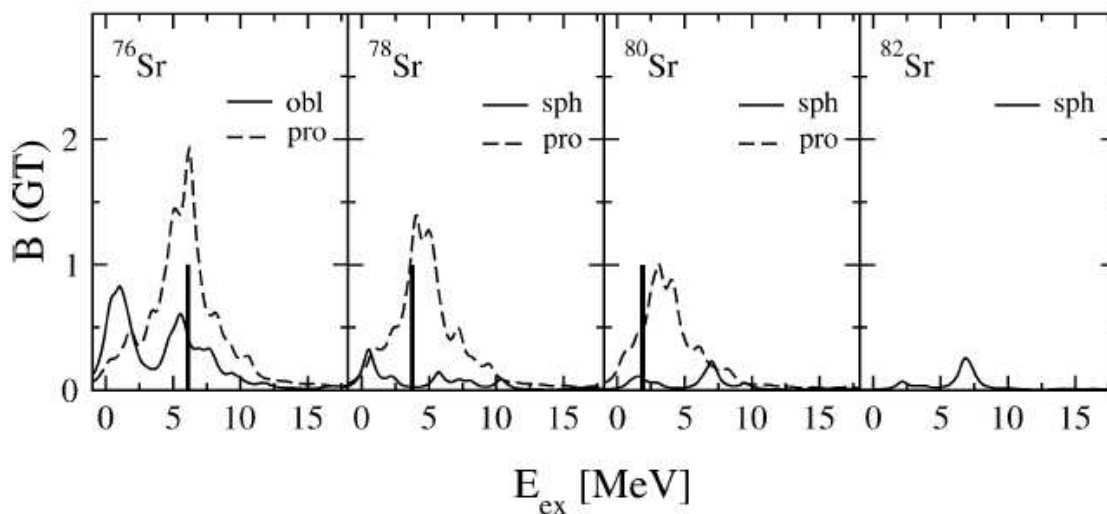


Figure 12.8: Distribución $B(\text{GT})$ en unidades de $g_A^2/4\pi$ como función de la energía de excitación del núcleo hijo. El cálculo se ha realizado asumiendo diferentes deformaciones en el estado fundamental [33].

En esta parte del trabajo nos planteamos medir la $B(\text{GT})$ en la desintegración del ^{76}Sr y, por comparación con los resultados de [33], medir por primera vez el signo de la deformación de este núcleo, es decir, si es oblatado o prolado en su estado fundamental.

Para realizar esta medida instalamos un nuevo TAS llamado Lucrecia en ISOLDE-CERN, Ginebra (Suiza). Este detector consta de un cilindro de NaI(Tl) de dimensiones $L=\varnothing=38$ cm con un agujero según su eje transversal de $\varnothing=7.5$ cm. Por un lado del agujero entra la fuente radioactiva a estudiar (^{76}Sr en este caso) que se implanta en cinta, y por el otro entran los detectores auxiliares: un centelleador plástico para detectar positrones y un telescopio de Ge cuya parte frontal es un detector en configuración planar para detectar rayos X. El núcleo radioactivo a estudiar, ^{76}Sr , se produce por la colisión de un haz de protones, acelerados a 1.4 GeV en el PS-Booster del CERN, contra un blanco de 52 g/cm^2 de Nb. Los productos de la reacción se ionizan en una fuente de iones de superficie caliente de W a unos $2100 \text{ }^\circ\text{C}$. Además se utiliza una técnica de fluorinación para evitar la contaminación isobárica [46, 47, 48]. El haz radioactivo, en forma de molécula ^{76}SrF , se produce de esta manera al extraer de la fuente de iones los productos de la reacción ionizados a estado de carga 1^+ con un potencial de 60 kV. Los dos imanes del separador HRS de ISOLDE seleccionan la masa adecuada que se quiere estudiar y esta se implanta en la estación de detección, en este caso Lucrecia. La implantación se realiza en realidad sobre una cinta situada en el agujero transversal de Lucrecia. Esta cinta se mueve convenientemente para quitar la actividad de los núcleos hijos una vez se ha producido la desintegración del padre. Una muestra de los espectros registrados en Lucrecia, en el detector de positrones y en el detector planar de Ge aparece en la Fig. 12.9.

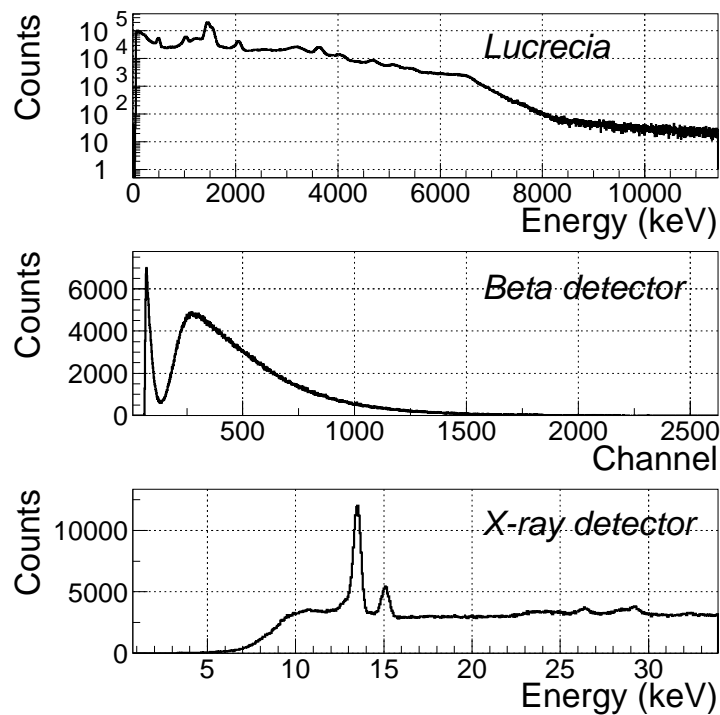


Figure 12.9: Espectros directos registrados en Lucrecia y en los detectores auxiliares durante la medida de la desintegración del ^{76}Sr .

Durante el experimento se tomaron también varias medidas del fondo ambiental y de la actividad del núcleo hijo, en este caso ^{76}Rb . Esto nos permitió después estimar correctamente las posibles contaminaciones que tenía el espectro a analizar. Una vez hecho esto nos planteamos el análisis de los datos. Para ello utilizamos un algoritmo de deconvolución de datos utilizado ya anteriormente en la reconstrucción de imágenes de satélite o en tomografía, el algoritmo de Expectación-Maximización (EM) [26]. Este algoritmo fue adaptado para el problema de los datos del TAS en [25], y para este trabajo ha sido readaptado de manera que puede analizar los datos teniendo en cuenta las contaminaciones estimadas anteriormente al nivel de la propia deconvolución de los datos, sin efectuar ninguna sustracción. Como conocimiento *a priori* el algoritmo necesita los datos experimentales y la función de respuesta del detector a la desintegración concreta que se quiere estudiar. Esta función de respuesta se calcula utilizando simulaciones Monte Carlo basadas en el código *GEANT4* del CERN [24], pero además es necesario conocer el esquema de niveles del núcleo hijo. Este esquema está bien conocido hasta 2 MeV [49]. Por encima de esta energía tuvimos que utilizar el modelo estadístico para calcular primero la densidad de niveles, utilizando el modelo “back-shifted Fermi gas model”, y después los “branching ratios” utilizando las parametrizaciones de las Ref. [52][53][54, 55] para las transiciones E1, M1 y E2 respectivamente. Llegados a este punto aplicamos el algoritmo de deconvolución de datos y obtuvimos la intensidad beta I_β en la desintegración del ^{76}Sr . A partir de aquí es sencillo calcular la $B(\text{GT})$, resultado principal de esta parte del trabajo que se muestra en la Fig. 12.10. La zona sombreada en color gris representa la incertidumbre debida sobre todo a los errores que conlleva la estimación de las constantes de normalización de los contaminantes.

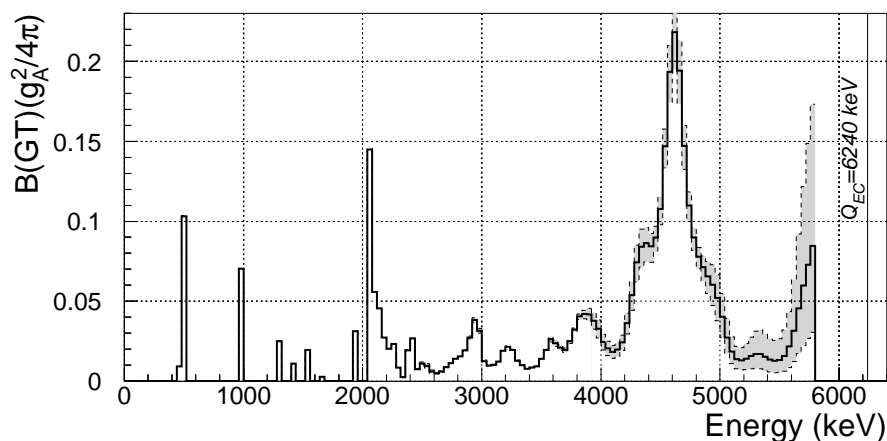


Figure 12.10: Distribución $B(\text{GT})$ en la desintegración β del ^{76}Sr como función de la energía de excitación del núcleo hijo ^{76}Rb .

En un cálculo RPA como el de [33] la energía calculada para los estados excitados

del núcleo no suele coincidir de forma precisa con la energía real de esos estados, por ello uno debe utilizar una forma adecuada de comparar teoría y experimentos en estos casos. Una forma de comparar nuestro resultado con el cálculo RPA de [33] es utilizar unos intervalos de energía muy anchos en el eje x de la gráfica. La otra es no representar la distribución B(GT) sino la distribución acumulada o integrada de B(GT), es decir, en cada canal de energía se representa la suma de la B(GT) desde 0 hasta esa energía. Ambas comparaciones podemos verlas respectivamente en la Fig. 12.11. Tanto en una comparación como en la otra se aprecia que el resultado experimental es sólo compatible con una forma prolada para el estado fundamental del ^{76}Sr . Este resultado concuerda con las expectativas teóricas de [39] y [40]. Además es compatible con un parámetro de deformación $\beta_2 \approx 0.4$ lo cual concuerda con el experimento haz realizado hace ya algunos años [31].

Este resultado no sólo establece por primera vez el signo de la deformación del ^{76}Sr en su estado fundamental, sino que además valida el método de obtener la deformación a partir de la desintegración β puesto que funciona correctamente en un caso en el que no hay ambigüedad por no haber mezcla de formas en el estado fundamental.

Este trabajo se ha publicado en *Physical Review Letters* [60], y ha sido seleccionado como de interés general por el *American Institute of Physics* en su revista electrónica *Physics News Update* (<http://www.aip.org/pnu/2004/split/686-3.html>).

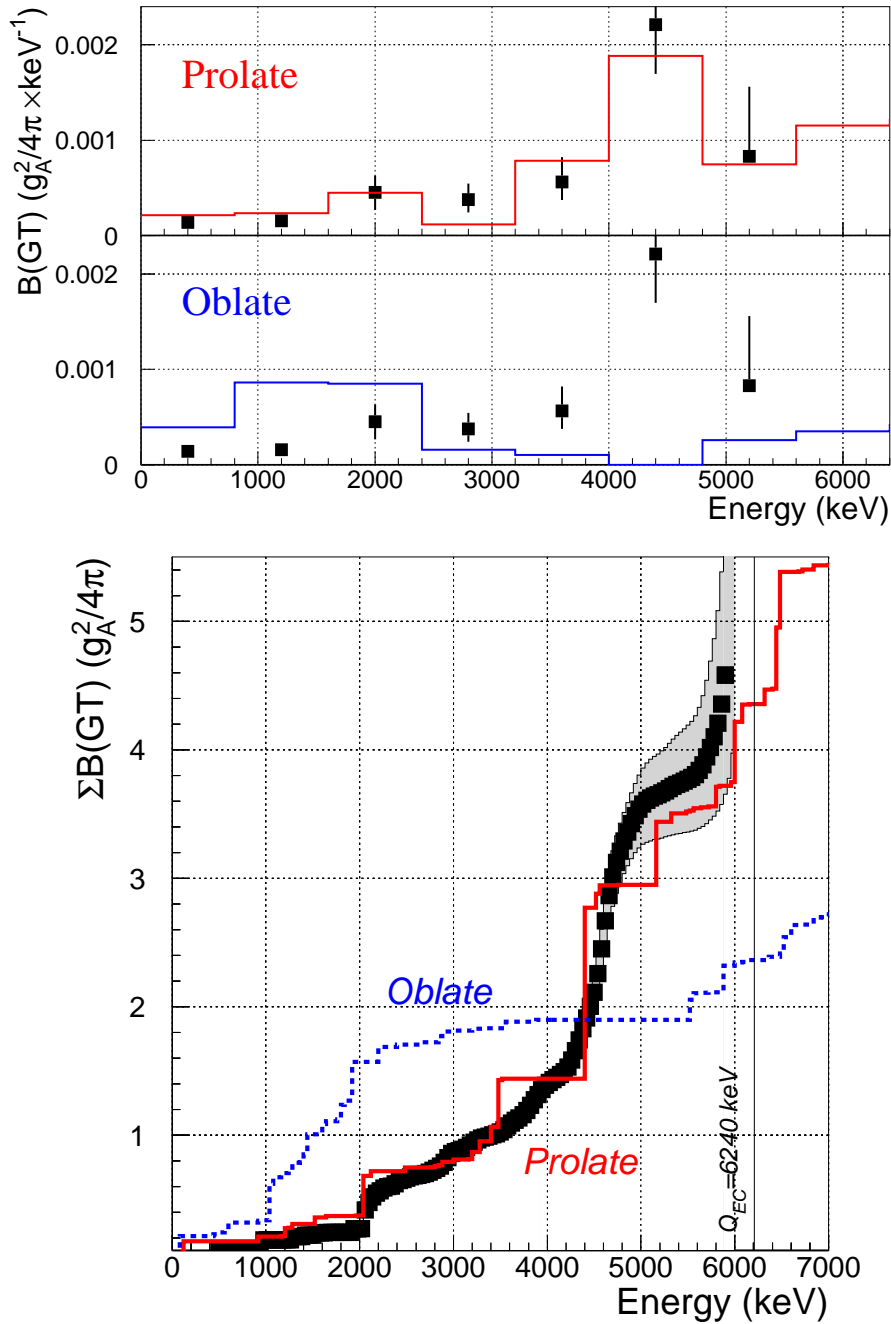


Figure 12.11: En el panel superior se representa la distribución de $B(\text{GT})$ en intervalos de energía de 800 keV. En el panel inferior se muestra para cada canal la $B(\text{GT})$ integrada hasta ese canal. En ambos casos los cuadrados negros son el resultado experimental de este trabajo, la línea sólida roja en cálculo teórico para forma prolada, y la azul para forma oblada.

Los núcleos alrededor del núcleo casi doblemente mágico ^{146}Gd

En la segunda parte del trabajo se ha estudiado la desintegración β de varios núcleos con pocos nucleones por encima del núcleo ^{146}Gd que tiene 82 neutrones, lo cual cierra una capa, y 64 protones, que aunque no cierra capa puede considerarse en este caso un número casi mágico. Esto se debe a que con el orbital $2d_{5/2}$ completamente lleno, la separación entre éste y el siguiente grupo de orbitales $2d_{3/2}$, $3s_{1/2}$ y $1h_{11/2}$ es de ≈ 2.4 MeV, y esto le confiere al ^{146}Gd el carácter de núcleo casi doblemente mágico [64]. Los núcleos un poco por encima del ^{146}Gd tienen, en general, el orbital $h_{9/2}$ de neutrones vacío. Por otro lado, según vamos aumentando el número de protones por encima de 64 el orbital $h_{11/2}$ comenzará a tener protones que pueden decaer a través de la transición permitida Gamow-Teller $\pi h_{11/2} \rightarrow \nu h_{9/2}$. Precisamente ésta es la transición que nos interesa. En este apartado estudiaremos varios casos de desintegración β que pueden interpretarse como el llenado paulatino del orbital $h_{11/2}$ desde el caso de 0 protones hasta el de 5 protones. En todos los casos trataremos tanto al núcleo padre como al hijo como excitaciones sobre el core¹ dado por el ^{146}Gd .

De entre todos los posibles casos alrededor del ^{146}Gd en este trabajo hemos medido la desintegración β de los núcleos impar- $N=83$ ^{148}Tb y ^{152}Tm , la del par- $N=82$ ^{148}Dy , y la del impar- $N=87$ ^{156}Tm . A los dos impar- $N=83$ ^{148}Tb y ^{152}Tm añadiremos los resultados obtenidos en [25] para el ^{150}Ho para completar la sistemática de la desintegración Gamow-Teller alrededor del ^{146}Gd como función del número de protones en el orbital $h_{11/2}$. Estos tres núcleos impar- $N=83$ presentan dos isómeros: uno con $J^\pi=2^-$ y el otro con $J^\pi=9^+$. El isómero de bajo espín debe tener una función de ondas dominada por la configuración $[\pi d_{3/2} \nu f_{7/2}]_{2^-} [\pi^{2n}]_{0^+}$, mientras que en el de alto espín la configuración dominante debe ser $[\pi h_{11/2} \nu f_{7/2}]_{9^+} [\pi^{2n}]_{0^+}$. En ambos casos el segundo término $[\pi^{2n}]_{0^+}$ representa pares de protones acoplados a 0^+ que ocupan parcialmente los tres orbitales de protones $2d_{3/2}$, $3s_{1/2}$ y $1h_{11/2}$ debido a correlaciones de “pairing”. Por tanto la desintegración del 2^- siempre se producirá por rotura de un par de protones, lo cual puebla estados de cuatro partículas en el hijo, mientras que la desintegración del 9^+ tendrá dos componentes: una debida a la desintegración del protón desapareado en el orbital $h_{11/2}$ que poblará un único estado de dos partículas en el hijo, y otra debida a la rotura del par de protones que poblará de nuevo estados de cuatro partículas en el hijo. Teniendo en cuenta la energía de monopartícula del $h_{9/2}$ en neutrones en el núcleo hijo, y la energía necesaria para romper un par de protones y un par de neutrones, uno puede estimar que la energía de los estados de 4 partículas es de $\approx 4-5$ MeV.

Todos los casos estudiados en este trabajo que se han mencionado arriba se mi-

¹La palabra *core* se puede traducir como *corazón* o *núcleo*. En este caso es la parte inerte del núcleo en contraposición con las partículas de valencia.

dieron en el GSI de Darmstadt (Alemania). Allí se utilizaron haces de iones pesados para producir los núcleos de interés a través de reacciones de fusión- evaporación. En el caso de los impar- $N=83$ el isómero de bajo espín se pudo producir limpiamente a través de la desintegración β del padre par- $N=82$. El isómero de alto espín siempre se produjo contaminado con una cierta contribución del de bajo espín pero este se pudo sustraer gracias al hecho de tener una medida limpia para el de bajo espín. En la Tabla 12.4 se muestra un resumen de las distintas reacciones de núcleo compuesto utilizadas para producir cada caso de interés. La energía del haz siempre fue de aproximadamente 5 MeV/a, es decir, muy cercana a la barrera de Coulomb, y el grosor de los blancos osciló entre 1 y 5 mg/cm².

Núcleo	Reacción	Núcleo	Reacción
¹⁴⁸ Tb 2 ⁻	⁹³ Nb(⁵⁸ Ni,3pβ ⁺) ¹⁴⁸ Tb 2 ⁻	¹⁴⁸ Tb 9 ⁺	⁹⁴ Zr(⁵⁸ Ni,3pn) ¹⁴⁸ Tb
¹⁵² Tm 2 ⁻	⁹⁶ Ru(⁵⁸ Ni,2pβ ⁺) ¹⁵² Tm 2 ⁻	¹⁵² Tm 9 ⁺	¹⁰² Pd(⁵⁸ Ni,α3pn) ¹⁵² Tm
¹⁵⁶ Tm	¹⁰³ Rh(⁵⁸ Ni,4pn) ¹⁵⁶ Tm	¹⁴⁸ Dy	⁹³ Nb(⁵⁸ Ni,3p) ¹⁴⁸ Dy

Table 12.4: Reacciones de fusión- evaporación utilizadas en este estudio sistemático

Los resultados obtenidos para la distribución B(GT) en los núcleos impar- $N=83$ se muestran en la Fig. 12.12. De abajo a arriba tenemos la desintegración del ¹⁴⁸Tb, el ¹⁵⁰Ho (tomado de [25]) y el ¹⁵²Tm. En cada caso a la izquierda se presenta la desintegración del isómero de bajo espín y a la derecha el de alto espín. En la parte superior de cada gráfica aparecen unos puntos que indican el número de protones responsables de cada desintegración. Por ejemplo en la desintegración del ¹⁵²Tm 9⁺ tenemos el protón desapareado que decae a un único estado de dos partículas a 2.2 MeV, y dos pares de protones que estarán repartidos entre los orbitales 2d_{3/2}, 3s_{1/2} y 1h_{11/2}. Cuando uno de estos pares está en el orbital h_{11/2} y se rompe, decae a través de la transición Gamow-Teller poblando los estados de cuatro partículas en el núcleo hijo que forman la resonancia alrededor de 4.5 MeV. En las gráficas aparece también el valor numérico de la B(GT) que va a la resonancia a 4.5 MeV o al estado de baja energía.

Como principales características de las distribuciones obtenidas podemos mencionar el hecho de que en todas se puebla una resonancia formada por estados de cuatro partículas centrada a unos 4.5 MeV de energía de excitación en el hijo. En el ¹⁴⁸Tb 2⁻ esta resonancia se encuentra más bien a 5.5 MeV debido a la energía necesaria para promocionar un par de protones desde el core ¹⁴⁶Gd hasta el h_{11/2} ya que el ¹⁴⁸Tb es el único caso en el que no hay pares de protones en el h_{11/2} a excepción de los que promocionan desde el core de ¹⁴⁶Gd debido a correlaciones de pairing. En el ¹⁴⁸Tb 9⁺ uno pensaría que sucede lo mismo, y así es, pero la resonancia baja en energía debido a un efecto único en este núcleo que se explicará después. La otra característica común en los casos del ¹⁵⁰Ho y ¹⁵²Tm es la cola que se forma tras

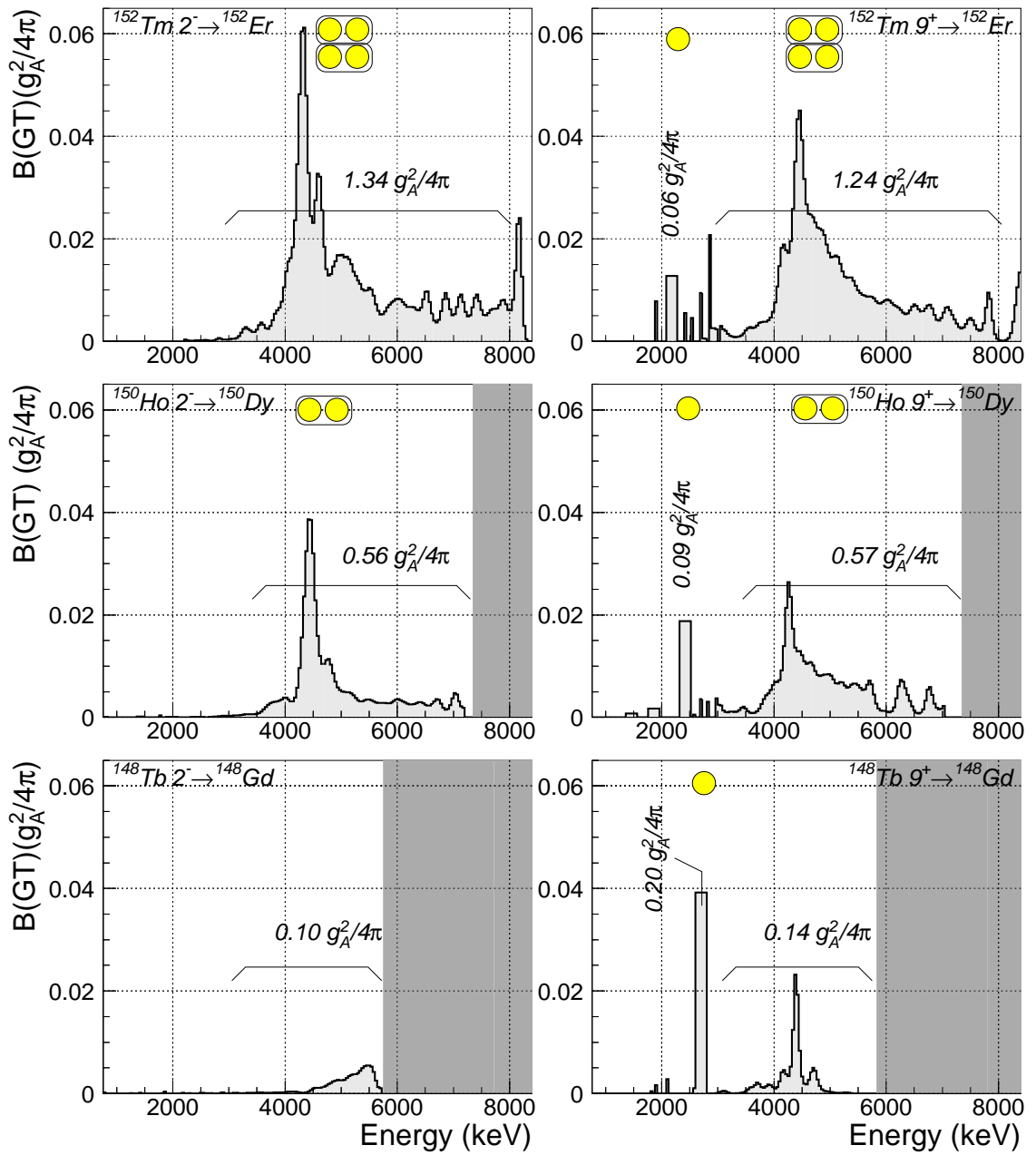


Figure 12.12: Distribución B(GT) en la desintegración de los dos isómeros de los núcleos impar- $N=83$ estudiados en este trabajo.

la resonancia y que llega hasta el Q_{EC} donde queda cortada. Esta cola se observó siempre en las reacciones (p,n) pero nunca se pudo cuantificar correctamente debido a las ambigüedades que tienen esos experimentos al determinar el fondo. En nuestro caso no existen tales ambigüedades, es decir, la cola es real y podría explicar ese “quenching” que se produce al sumar la B(GT). Si esa cola se prolonga hasta cerca

de 200 MeV como se calcula en [16] y se lleva alrededor de 50% de la B(GT) debido a la mezcla de configuraciones esto explica que en las reacciones (p,n) sólo se observe un 60% de la B(GT) total que se debería observar según la regla de suma de Ikeda.

Como ya se dijo, además de los impar-N=83 también se ha medido la desintegración del núcleo ^{148}Dy y la del ^{156}Tm . El resultado para la distribución de B(GT) de ambos casos se presenta en la Fig. 12.13.

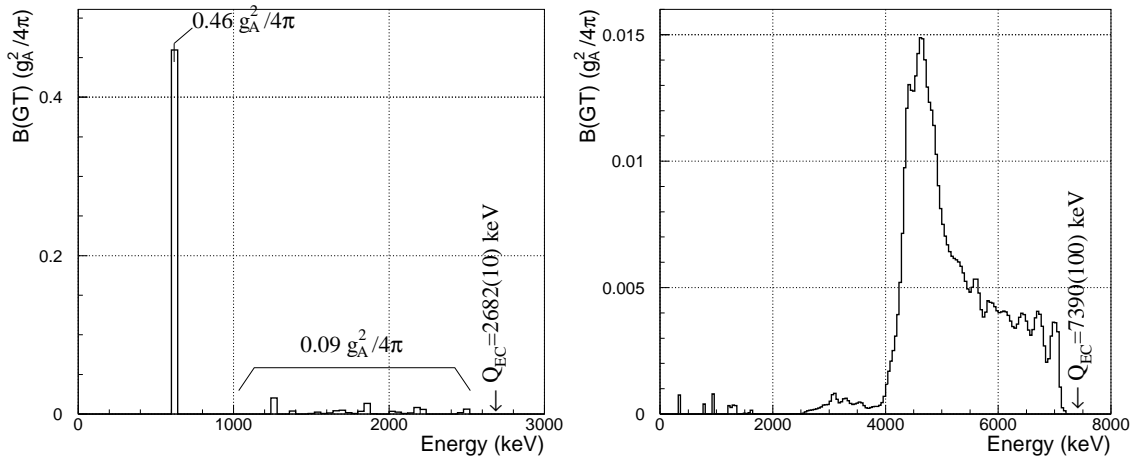


Figure 12.13: Distribución B(GT) en la desintegración del ^{148}Dy (izda.) y del ^{156}Tm (dcha.).

En el caso del ^{148}Dy se observa que toda la B(GT) está concentrada en un único estado de dos partículas a 620 keV. Esto se debe a que el ^{148}Dy en su estado fundamental es simplemente un par de protones sobre el core de ^{146}Gd . Por ello su desintegración se deberá a la rotura de este par y poblará en el hijo un estado dominado por la configuración $[\pi h_{11/2} \nu h_{9/2}]_{1+}$. Por encima de este se observa muy poca B(GT) a otros estados. De la suma total de B(GT) en esta desintegración se obtiene un patrón de desintegración de un par. Es más, por comparación de este resultado con el resultado para la desintegración del $^{148}\text{Tb } 2^-$ podemos estimar el número de pares promocionados desde el core de ^{146}Gd que ocupan el orbital $h_{11/2}$, ya que si llamamos p al número de pares que suben desde el core hasta el $h_{11/2}$, y asumimos que la B(GT) es proporcional a la ocupación del $h_{11/2}$, podemos escribir:

$$\frac{B(GT)_{^{148}\text{Dy}}}{B(GT)_{^{148}\text{Tb } 2^-}} = \frac{0.67 + p}{p}, \quad (12.6)$$

ya que un par *real* ocupando los tres orbitales $2d_{3/2}$, $3s_{1/2}$ y $1h_{11/2}$ estará un 67% del tiempo en el $h_{11/2}$. De aquí podemos despejar p obteniendo:

$$p = 0.67 \times \left(\frac{B(GT)_{148Dy}}{B(GT)_{148Tb\ 2^-}} - 1 \right)^{-1} = 0.15(3) \quad (12.7)$$

Este número es cinco veces menor que el que se mide como ocupación de pares en el $h_{11/2}$ en el estado fundamental del ^{144}Sm , que es 0.80(15) según [73]. Esto refuerza la idea de capa cerrada en $Z=64$ ya que se puede interpretar como un gran aumento de separación entre el orbital $2d_{5/2}$ y el grupo de tres $2d_{3/2}$, $3s_{1/2}$ y $1h_{11/2}$ cuando pasamos del ^{144}Sm al ^{146}Gd . Nuestro resultado para la desintegración del ^{148}Dy ha sido recientemente aceptado para su publicación en *Physical Review C* [72].

De la distribución $B(GT)$ en la desintegración del ^{156}Tm (Fig. 12.13 dcha.) podemos mencionar varias cosas. La primera es que debemos compararla con la distribución obtenida para la desintegración del $^{152}\text{Tm}\ 2^-$ (Fig. 12.12 arriba izda.) ya que la diferencia entre una desintegración y la otra no es más que el número de neutrones espectadores, que pasa de ser 1 a ser 5. Como consecuencia de esto la mezcla de configuraciones será mayor en la desintegración del ^{156}Tm y por ello se observa que la estructura de la resonancia es mucho más ancha, más suave, y la cola es mucho mayor. Por otra parte esta cola se debe llevar mucha $B(GT)$ más allá del Q_{EC} ya que la $B(GT)$ total pasa de ser 1.3(2) $g_A^2/4\pi$ a 0.48(3) $g_A^2/4\pi$ en el caso del ^{156}Tm , cuando estos dos números no deberían ser tan distintos en principio.

Podemos comparar los resultados experimentales medidos en este trabajo con las estimaciones teóricas de [78] para la $B(GT)$ total según el número de protones en el $h_{11/2}$. En esos cálculos se comienza estimando la $B(GT)$ según el modelo extremo de partícula independiente y luego se corrige de acuerdo a ciertos efectos como las correlaciones de pairing, la polarización del core y efectos de orden mayor. Los resultados del cálculo [78] se comparan con nuestra medida en la Fig. 12.14. Aunque ambos resultados siguen una misma tendencia, el cálculo teórico sobreestima la medida en todos los casos. Esto se debe a que el cálculo de [78] se realiza en un espacio de configuraciones muy limitado que sólo incluye el $h_{11/2}$ de protones y el $h_{9/2}$ de neutrones. Además no se tiene en cuenta la mezcla de configuraciones.

Finalmente hemos realizado unos cálculos shell-model utilizando el código OXBASH [83] para las desintegraciones de los seis isómeros que aparecen en la Fig. 12.12. Para ello se ha calculado una interacción residual a dos cuerpos basada en datos empíricos siguiendo el método que se emplea en la Ref. [20] para el caso del $^{150}\text{Ho}\ 2^-$ y que originalmente se desarrolló en [79]. Hemos usado un espacio de configuraciones que incluye los orbitales de protones: $2d_{3/2}$, $3s_{1/2}$ y $1h_{11/2}$, y los de neutrones: $2f_{7/2}$ y $1h_{9/2}$. Los resultados de este cálculo shell-model para los casos de bajo espín podemos verlos en la Fig. 12.15. Se ha convolucionado el resultado teórico con una gaussiana de anchura ≈ 165 keV para dar cuenta de la anchura que se observa en el experimento debido a la mezcla de configuraciones. Como vemos se reproduce bien la posición del centroide de la resonancia en los tres casos calculados.

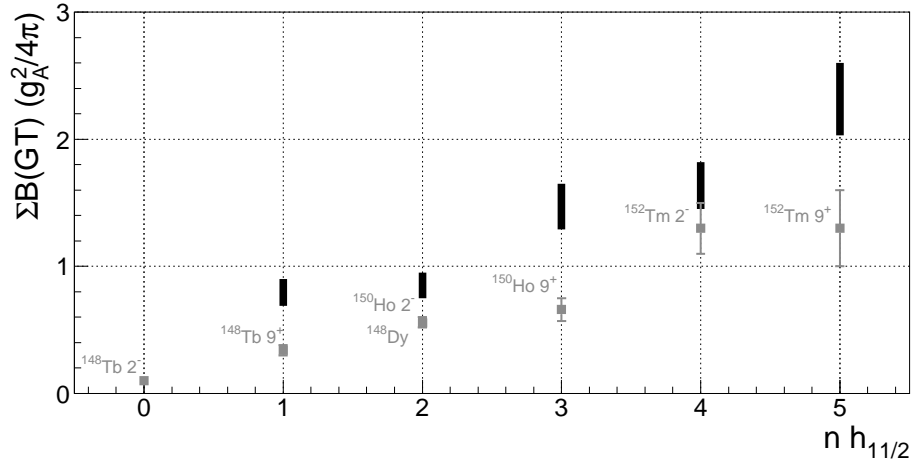


Figure 12.14: Evolución de la $B(GT)$ total con el número de protones en el orbital $h_{11/2}$. Los resultados experimentales de este trabajo (cuadrados grises) se comparan con los cálculos teóricos de [78] (barras negras).

En el peor de los casos, el $^{152}\text{Tm } 2^-$, la diferencia entre el centroide calculado y el medido es de 0.5 MeV. Para este caso se han usado los mismos elementos de matriz que para el ^{150}Ho ya que los datos empíricos de donde extraemos los elementos de matriz son inexistentes para el ^{152}Tm por estar ya muy alejado de la estabilidad. Esto explica que sea el caso que peor reproduce el experimento de los tres de la figura.

Para calcular la desintegración de los isómeros de alto espín se ha procedido de la misma manera. La comparación experimento-teoría para estos casos aparece en la Fig. 12.16. De la comparación queda claro que hay un problema con el $^{148}\text{Tb } 9^+$. Los otros dos casos se reproducen aceptablemente en términos de posición del centroide aunque se observa una estructura de doble pico en el cálculo que no aparece en la medida experimental. La explicación de por qué el cálculo shell-model no reproduce bien la medida de la desintegración del $^{148}\text{Tb } 9^+$ está estrechamente vinculada con la explicación de por qué la resonancia en la desintegración del $^{148}\text{Tb } 2^-$ aparece corrida ≈ 1 MeV hacia energías más altas que en los otros casos y la resonancia en la desintegración del $^{148}\text{Tb } 9^+$ no. En el ^{148}Tb no hay pares de protones en el $h_{11/2}$ a no ser que estos vengan promocionados desde el core de ^{146}Gd . De hecho hemos podido estimar que en el estado fundamental hay una ocupación del $h_{11/2}$ de 0.15 pares de protones en este núcleo. Sin embargo a la hora de calcular la energía de excitación de los estados poblados en el hijo hay que tener en cuenta la energía requerida para promocionar esos pares desde el core de ^{146}Gd , y ésta resulta ser de unos 980 keV. Por eso la resonancia en la desintegración del $^{148}\text{Tb } 2^-$ aparece a ≈ 5.5 keV, es decir, 1 MeV por encima de la resonancia en los otros casos. Sin embargo uno esperaría el mismo fenómeno en la desintegración del $^{148}\text{Tb } 9^+$ y sin embargo no es así.

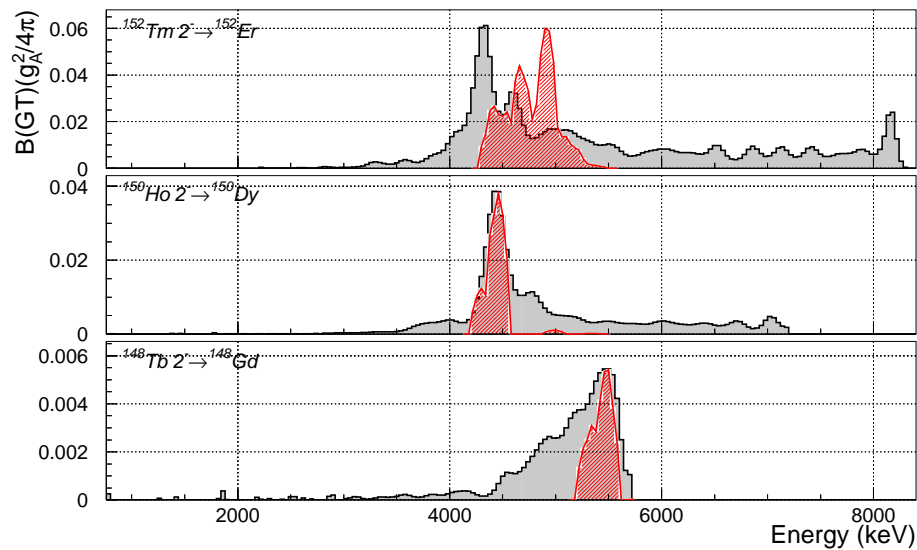


Figure 12.15: Distribución $B(GT)$ en el isómero de bajo espín de los núcleos impar- $N=83$ por encima del ^{146}Gd . Los resultados experimentales (gris) se comparan con cálculos teóricos shell-model (rojo).

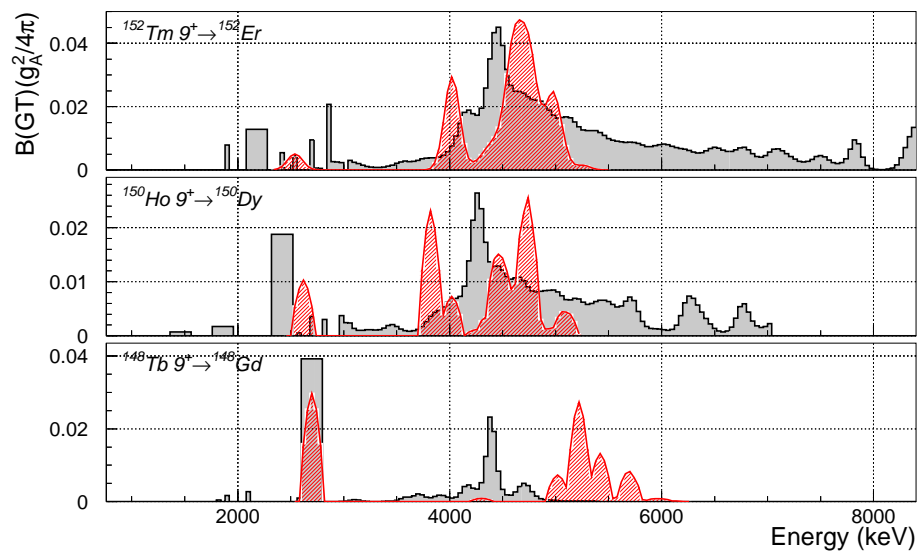


Figure 12.16: Como en la Fig. 12.4 pero para los isómeros de alto espín.

La explicación la podemos intuir al observar el resultado del cálculo shell-model para la función de ondas de los estados que se pueblan en la desintegración β del $^{148}\text{Tb } 9^+$. Estos estados deben tener como configuración dominante $[\pi h_{11/2} \pi h_{11/2} \nu f_{7/2} \nu h_{9/2}]_{8^+, 9^+, 10^+}$. El cálculo teórico nos dice que el estado con $J^\pi=8^+$ más poblado no es el de energía más baja que tendría los dos protones acopla-

dos a 0^+ , sino el segundo, con los dos protones acoplados a 2^+ . En el caso de los estados con $J^\pi=9^+,10^+$ obviamente los dos protones no pueden estar acoplados a 0^+ sino como mínimo a 2^+ . Por tanto todos los estados que se pueblan en la desintegración del ^{148}Tb 9^+ se mezclarán fuertemente con otros estados $8^+, 9^+, 10^+$ cuya configuración sea del tipo $[2^+ \otimes \nu f_{7/2} \nu h_{9/2}]_{8^+,9^+,10^+}$. Aquí el 2^+ se refiere a cualquier excitación de protones en el core de ^{146}Gd que se acople a 2^+ . Más concretamente vamos a considerar el primer estado 2^+ del ^{146}Gd que se debe a una excitación partícula-hueco $[\pi d_{5/2}^{-1} \pi s_{1/2}]_{2^+}$ a 1972 keV [85]. La energía de estos estados $[2^+ \otimes \nu f_{7/2} \nu h_{9/2}]_{8^+,9^+,10^+}$ será aproximadamente la del estado 8^+ de dos partículas $[\nu f_{7/2} \nu h_{9/2}]_{8^+}$, es decir 2694 keV en el ^{148}Gd , más 1972 keV, resultando una energía de excitación de 4.6 MeV. Si los estados de la resonancia, originalmente a ≈ 5.5 MeV se mezclan con estos estados, podemos entender la B(GT) que observamos en el experimento a 4.6 MeV. El hecho de que el cálculo shell-model no reproduzca esta B(GT) tiene ahora sentido y es perfectamente entendible si tenemos en cuenta que el espacio de configuraciones utilizado en el cálculo no incluye el orbital de protones $d_{5/2}$ que es pieza fundamental en la función de ondas del estado 2^+ del ^{146}Gd . Para hacer el cálculo correctamente debería incluirse este orbital, pero entonces partiríamos del core dado por ^{140}Ce y deberíamos hacer un cálculo en el cual tendríamos seis protones distribuidos entre los cuatro orbitales de protones, y dos neutrones distribuidos entre los dos orbitales de neutrones. Las dimensiones del espacio requerido para dicho cálculo exceden la potencia de cálculo disponible hoy en día.

Resumen y conclusiones

En este trabajo se ha estudiado la desintegración β Gamow-Teller de varios núcleos en dos de las tres regiones de la tabla nuclear en donde esta desintegración está permitida por las reglas de selección y es accesible dentro de la ventana Q_{EC} . Para poder medir bien la “fuerza” de la transición Gamow-Teller, conocida como Gamow-Teller strength o B(GT), se ha utilizado la técnica de Espectroscopía de Absorción Total, que es hoy en día la única forma posible de medir la B(GT) correctamente en la desintegración de núcleos medios y pesados.

En la región de los $N=Z$ con $A=70-80$ se ha estudiado la deformación del núcleo ^{76}Sr en su estado fundamental. Por comparación de nuestro resultado experimental con los cálculos teóricos de [33] hemos establecido por primera vez el signo de la deformación de este núcleo, resultando ser fuertemente prolado. Además nuestro resultado valida el método para establecer el signo de la deformación ya que se ha aplicado a un caso que no tiene ambigüedades por carecer de mezcla de formas en el estado fundamental.

En la región de las tierras raras alrededor del ^{146}Gd hemos medido la desintegración β de varios núcleos: ^{152}Tm , ^{148}Tb , ^{148}Dy y ^{156}Tm . Con estos resultados y los de la Ref. [25] para la desintegración del ^{150}Ho hemos podido hacer un estudio

sistemático de la transición de Gamow-Teller permitida $\pi h_{11/2} \rightarrow \nu h_{9/2}$ para distintas ocupaciones del orbital de protones $h_{11/2}$. En todos los casos hemos observado la resonancia de Gamow-Teller dentro de la ventana energética dada por el Q_{EC} . En el ^{148}Dy toda la $B(\text{GT})$ se concentra en un único estado a 620 keV. En los demás casos se distribuye entre muchos estados de cuatro partículas alrededor de 4.5 MeV excepto en el $^{148}\text{Tb } 2^-$ que decae poblando la resonancia más arriba en energía debido al hecho de que para poder decaer tiene que promocionar un par de protones del core de ^{146}Gd . En los isómeros de alto espín parte de la $B(\text{GT})$ va a parar a un estado de dos partículas que se debe a la desintegración de un protón desapareado en el núcleo padre. Más allá de los estados de la resonancia a 4.5 MeV se observa una cola que se extiende hasta que es cortada por el Q_{EC} y que pensamos que explica el efecto de “quenching” observado en las reacciones (p,n) que es debido a la mezcla de la configuración original con otras configuraciones bien de cuatro partículas o bien de carácter partícula hueco.

Bibliography

- [1] A. Bohr and B. Mottelson, *Nuclear Structure (vol. 1)*, chap. 1 (W.A. Benjamin Inc., 1969)
- [2] Franz Osterfeld, *Reviews of Modern Physics* **64 (No.2)** (1992) 491
- [3] W.P. Alford and B.M. Spicer, *Advances in Nuclear Physics* **24** (1998) 2
- [4] Yoshitaka Fujita, *Nucleon-Hadron Many-Body Systems*, chap. 4 (Oxford Univ. Press, 2000)
- [5] K. Ikeda, S. Fujii and J.I. Fujita, *Phys. Lett.* **3** (1963) 271
- [6] R.R. Doering *et al.*, *Phys. Rev. Lett.* **35** (1975) 1691
- [7] C. Gaarde *et al.*, *Nucl. Phys.* **A369** (1981) 258, *and references therein*
- [8] K. Ikeda, *Prog. Theor. Phys.* **31** (1964) 434
- [9] C. Gaarde *et al.*, *Nucl. Phys.* **A396** (1983) 127c
- [10] D.H. Wilkinson, *Phys. Rev.* **C7** (1973) 930
- [11] M. Ericson, A. Figureau and C. Thevenet, *Phys. Lett.* **B45** (1973) 19
- [12] M. Rho, *Nucl. Phys.* **A231** (1974) 493
- [13] E. Oset and M. Rho, *Phys. Rev. Lett.* **42** (1979) 47
- [14] K. Shimizu, M. Ichimura and A. Arima, *Nucl. Phys.* **A226** (1974) 282
- [15] A. Arima and H. Hyuga, in “Mesons in Nuclei”, *ed. by D. Wilkinson* (North-Holland, 1997) 683
- [16] G.F. Berscht and I. Hamamoto, *Phys. Rev.* **C26** (1982) 1323
- [17] Nguyen Dinh Dang, A. Arima *et al.*, *Phys. Rev. Lett.* **79** (1997) 1638
- [18] T. Wakasa, H. Sakai *et al.*, *Phys. Rev.* **C55** (1997) 2909
- [19] J.C. Hardy *et al.*, *Phys. Lett.* **71B** (1977) 307

- [20] A. Algora *et al*, Phys. Rev. **C68** (2003) 034301
- [21] Z. Hu *et al*, Phys. Rev. **C62** (2000) 064315
- [22] C.L. Duke *et al*, Nucl. Phys **A51** (1970) 609
- [23] D. Cano *et al*, Nucl. Instr. and Meth. **A430** (1999) 488
- [24] S. Agostinelli *et al.*, Nucl. Inst. and Meth. **A506** (2003) 250
URL <http://wwwasd.web.cern.ch/wwwasd/geant4/geant4.html>
- [25] D. Cano Ott, Ph.D. thesis, Universidad de Valencia (2000)
- [26] A.P. Dempster *et al*, J. R. Statist. Soc. **B39** (1977) 1
- [27] G. D'Agostini, Nucl. Inst. and Meth. **A362** (1995) 487
- [28] D. Cano *et al*, Nucl. Instr. and Meth. **A430** (1999) 333
- [29] S.G. Nilsson and I. Ragnarson, *Shapes and Shells in Nuclear Structure*, chap. 8
(Cambridge Univ. Press, 1995)
- [30] W. Gelletly *et al*, Phys. Lett. **B253** (1991) 287
- [31] C.J. Lister *et al*, Phys. Rev. **C42** (1990) R1191
- [32] I. Hamamoto *et al*, Z. Phys. **A353** (1995) 145
- [33] P. Sarriguren *et al*, Nucl. Phys. **A635** (1998) 55
- [34] C. Miehé *et al*, in H. Sakai *et al*, ed., “*New Facet of Spin Giant Resonances in Nuclei*” *Conf. Proc.* (World Scientific, 1997)
- [35] P. Sarriguren *et al*, Nucl. Phys. **A658** (1999) 13
- [36] P. Sarriguren *et al*, Nucl. Phys. **A691** (2001) 631
- [37] D. Vautherin , Phys. Rev. **C7** (1973) 296
- [38] H. Flocard *et al*, Nuc. Phys. **A203** (1973) 433
- [39] P. Bonche *et al*, Nucl. Phys. **A443** (1985) 39
- [40] A. Petrovici *et al*, Nucl. Phys. **A605** (1996) 290
- [41] F. Frisk *et al.*, Phys. Rev. **C52** (1995) 2468
- [42] A. Petrovici *et al*, Nucl. Phys. **A665** (2000) 333
- [43] A. Algora *et al*, Phys. Rev. **C61** (2000) 031303

- [44] I. Hamamoto *et al*, Phys. Rev. **C48** (1993) R960
- [45] H. Schatz *et al*, Phys. Rep. **294** (1998) 167
- [46] H.L. Ravn *et al*, Nucl. Instr. and Meth. **123** (1975) 131
- [47] Y. Kawase *et al*, Nucl. Instr. and Meth. **B70** (1992) 146
- [48] R. Kirchner, Nucl. Instr. and Meth. **B126** (1997) 135
- [49] Ph. Dessagne *et al*, Eur. Phys. J. **A20** (2004) 405
- [50] W. Dilg *et al*, Nucl. Phys. **A217** (1973) 269
- [51] J. Giovinazzo *et al*, Nucl. Phys. **A674** (2000) 394
- [52] J.C. Hardy *et al*, Phys. Lett. **B109** (1982) 242
- [53] J. Kopecky *et al*, Phys. Rev. **C41** (1990) 1941
- [54] J. Speth *et al*, Rep. Prog. Phys. **44** (1981) 719
- [55] W.V. Prestwich *et al*, Z. Phys. **A315** (1984) 103
- [56] N.B. Gove and M.J. Martin, Nuclear Data Tables **A10** (1971) 246
- [57] G. Audi *et al*, Nucl. Phys. **A729** (2003) 337
- [58] F. Becker *et al*, Eur. Phys. J. **A4** (1999) 103
- [59] E. Poirier *et al*, Phys. Rev. **C69** (2004) 034307
- [60] E. Nácher *et al*, Phys. Rev. Lett. **92** (2004) 232501
- [61] P. Kleinheinz *et al*, Z. Phys. **A284** (1978) 351
- [62] P. Kleinheinz *et al*, Z. Phys. **A286** (1978) 27
- [63] L. Caballero, Ph.D. thesis, Universidad de Valencia (expected for 2005)
- [64] P. Kleinheinz *et al*, Z. Phys. **A290** (1979) 279
- [65] R. Kirchner and E. Roeckl, Nucl. Inst. and Meth. **133** (1976) 187
- [66] R.B. Firestone, *Table of Isotopes* (John Wiley & Sons, Inc., 1996)
- [67] A. Algora, private communication
- [68] K.S. Toth *et al*, Phys. Rev. **C35** (1987) 310
- [69] A. Algora *et al*, in J. Äystö *et al*, ed., “ENAM2001” *Conf. Proc.* (Springer 2001)

- [70] A. Gadea, Ph.D. thesis, Universidad de Valencia (1994)
- [71] P. Kleinheinz *et al*, Phys. Rev. Lett. **55** (1985) 2664
- [72] A. Algora *et al.*, Phys. Rev. C, to be published.
- [73] B.H. Wildenthal *et al*, Phys. Rev. **C3** (1971) 1199
- [74] A. Gadea *et al*, in W. Gelletly *et al*, ed., *Proc. of the Int. Conf. on "The Future of Nuclear Spectroscopy"*, Crete (NCSR Demokritos 1993)
- [75] A.A. Bykov *et al*, Izv. AN SSSR ser. fis. **44** (1980) 15
- [76] V.D. Wittman and L. Batist, private communication
- [77] E. Nácher *et al.*, GSI Sci. Report **2002** (2003) 8
URL <http://www-aix.gsi.de/annrep2002/files/8.pdf>
- [78] I.S. Towner, Nucl. Phys. **A444** (1985) 402
- [79] J. Blomqvist *et al.*, Z. Phys. **A312** (1983) 27
- [80] C. Gaarde *et al.*, Nucl. Phys. **A334** (1980) 248
- [81] C. Gaarde *et al.*, Nucl. Phys. **A222** (1974) 579
- [82] H. Toki and G.F. Berscht, Phys. Rev. **C26** (1982) 2330
- [83] B.A. Brown *et al.*, MSU-NSCL Report **No. 524** (1994)
- [84] J. Blomqvist, private communication
- [85] S.W. Yates *et al.*, Z. Phys. **A324** (1986) 417

Agradecimientos

Llegados aquí me toca la difícil tarea de comprimir en dos páginas el reconocimiento a tanta gente sin cuya inestimable ayuda todo esto no hubiera llegado a buen puerto. Aunque me va a resultar imposible mencionar a todos los que se merecen mi más sincero agradecimiento, lo voy a intentar.

El primer lugar lo deben ocupar las dos personas que más relacionadas han estado con este trabajo. Berta Rubio y Alejandro Algora. Por todo lo que he aprendido de vosotros, por la paciencia que habéis tenido cada vez que nos hemos sentado a discutir de algo, porque empecé hace cuatro años sin saber hacer la “o” con un canuto y termino ahora con unos conocimientos y una experiencia en el campo de la Física Nuclear que sin duda os debo, por los momentos buenos y los malos en cada uno de los infinitos experimentos que hemos compartido... , por todo eso y mucho más: GRACIAS.

Al resto de componentes del grupo de espectroscopía gamma del IFIC: José Luis y Daniel han sido los pioneros en esto de la espectroscopía de absorción total y no han dudado en transmitirnos sus conocimientos e ideas sobre el tema. Luis me ha convertido en un vicioso del esquí, pero más que eso merece una mención especial por ser de los pocos terrícolas que andan por estos lares. Con César compartí una buena temporada de penurias en el CERN cuando aún estaba soltero, je je... , eso se le ha acabado ya. De Juan Carlos no me puedo olvidar, ¿“pojjjjj qué”? pues “pojjjjjque” hace cada mañana un poco más divertida. Al sargento Agramunt le debo no sólo unos cuantos “berridos” en la nieve sino también los conocimientos adquiridos sobre “ren-pas, cli, iri, wso...” Con Trino, Andrés y Enrico he pasado también grandes momentos aquí y en la tierra de las pizzas. A todos ellos: GRACIAS.

I have always thought that this path started when I went to GSI as a summer student. During those three months in 1999, and during the different experiments performed there afterwards, I have always felt welcome at GSI thanks to the wonderful people of the Mass Separator group: Ernst, Joachim, Zenon, Chiara, Charly... However the first part of this work was performed at CERN where the invaluable help of Luis Mario “Lúí” and Genevieve made all the experiments possible. To all these friends at GSI and CERN: THANK YOU.

Por otra parte, tengo la inmensa suerte de contar con un montón de amigos que no tienen nada que ver con esto de la física (afortunados!!). Con Ernesto y Miriam lo he pasado muy bien y muy mal en las alturas. Espero que sigamos subiendo muchas montañas juntos. Pakete es ese tío que se empeña en correr y nadar más que yo, a ver si llegamos a hacer una triatlón juntos! Quique y Gabi se empeñan en recordarme que un día fui judoka y yo mientras les recuerdo que están los dos más gordos que yo. Ubaldo, Charly, Willy, Kris y Amparo están esperando a que deje de “partir átomos” para montar un cole juntos. Espero que sigamos mucho tiempo zampando paellas los diumenges en “la casita”. Aunque ya casi hablamos sólo por mail, también me acuerdo mucho de los que compartieron conmigo cinco añitos de “mire usted señorita” o “no tengaih miedo a decil-l-l-lo”: Joseja, Luis, Pedro, Jordi, Joselu, José Antonio, Edu. . . GRACIAS.

A la fantástica familia que tengo: abuelos/as, tíos/as y primos/as, nunca podré agradecerle bastante su apoyo incondicional y su enorme cariño (sí, esto ha quedado un poquito cursi). GRACIAS. Y por último los que han sido siempre más importantes para mí: mis padres y mi novia: pues no han tenido que aguantar ni nada!! Sin embargo nunca han pedido nada cambio y son sin duda los máximos responsables de que esté aquí acabando una tesis doctoral y siga tan contento. Gracias a los tres puedo decir orgulloso que he podido pasar momentos más fáciles o más difíciles, pero hasta la fecha no ha habido ni un sólo instante en mi vida que me haya sentido infeliz. GRACIAS PAPÁ, GRACIAS MAMÁ, GRACIAS SANDRA.

Valencia, Septiembre de 2004.